POLITECNICO
MILANO 1863

SCUOLA DI INGEGNERIA INDUSTRIALE
E DELL'INFORMAZIONE

Synchrotron x-ray spectra characterization for radiation therapy applications at the ESRF - ID17 Biomedical beamline

Tesi di Laurea Magistrale in
Physics Engineering - Ingegneria Fisica

Author: **Ilaria Di Manici**

Student ID: 943513
Advisor: Prof. Marco Moretti
Co-advisors: Dr. Paolo Pellicioli
Academic Year: 2020-21

Abstract

Microbeam radiation therapy (MRT) is an innovative radiotherapy technique based on the spatial fractionation of the irradiation field at micrometric scale. MRT showed improved outcome in preclinical studies, thanks to an increased healthy tissue tolerance to the radiation and efficacy in limiting the tumor development.
MRT is currently best performed at synchrotron radiation sources such as the ID17 Biomedical beamline at the European Synchrotron Radiation Facility (ESRF) where the incredible brilliance of the X-ray source is fully exploited. The MRT, as all the RT techniques, needs reliable dosimetric protocols because an accurate dose definition is mandatory for the successful outcome of clinical treatment. The basis of any dosimetry and irradiation protocol is a precise knowledge of the energy spectrum used. The aim of this study is the validation of the X-ray energy spectra used at ID17 for MRT studies in order to provide them as a reliable input for dosimetric studies and treatment planning calculation.
The spectra were calculated by mean of a software called OASYS, in-house developed at ESRF, used for the first time at ID17, that allows to perform a virtual synchrotron experiment. Half Value Layer (HVL) measurements were performed for the spectra validation. This method consists in calculating and measuring the attenuation of the spectrum caused by additional layer of materials to find the thickness needed to attenuate the intensity of the beam to half of its initial value. The characterization was performed for the most used beamline configurations defined for MRT studies.
The obtained X-ray spectra were used for dosimetry study in reference conditions. Depth dose profile were acquired inside a water equivalent phantom using a PTW PinPoint ionization chamber for absolute dosimetry and radiochromic films for relative attenuation measurement. The resulting experimental data sets were compared to corresponding Monte Carlo simulations of the setup used.
The results obtained showed an extremely good agreement between measured and computed data. For both the HVL measurement and for the absolute depth dose profile, the % difference between the measured and theoretical values was below 2% for the first method and below 3% for the second one. These values are respecting the conventional criteria

for RT application, for which the measured dose can deviate at maximum by 3% from the expected one. Regarding the relative depth dose profile performed with radiochromic films, the agreement was still good, with most of the values below 3%, but few outliers were reaching around 5% of difference, which may require a further investigation.
The results are overall satisfactory and proved that the software used to simulate the X-ray spectrum at the ID17 beamline is reliable for the simulation of the radiation spectra. The obtained spectrum profiles can be provided as reliable inputs for future developments in MRT dosimetry such as the use of dedicated treatment planning systems for the definition of the delivered dose in forthcoming clinical trials.

Keywords: microbeam radiotherapy, microbeams, dosimetry, synchrotron radiation, x-ray spectrum

Abstract in lingua italiana

La radioterapia per microfasci (MRT) è un'innovativa tecnica di radioterapia (RT) basata sul frazionamento spaziale del campo di irradiazione utilizzato, su scala micrometrica. La MRT ha mostrato ottimi risultati negli studi preclinici, grazie ad un'aumentata tolleranza dei tessuti sani alla radiazione ed ad un'efficacia nel limitare lo sviluppo del tumore.
La MRT è studiata al momento nelle sorgenti di radiazione di sincrotrone come la beamline biomedica ID17 allo European Synchrotron Radiation Facility (ESRF), per utilizzare al meglio le incredibili proprietà dei raggi-x emessi. La MRT, come tutte le tecniche di RT, si basa su affidabili protocolli di dosimetria, perché un'accurata definizione della dose utilizzata è obbligatoria per un positivo risultato nei trattamenti clinici. Alla base di ogni studio di dosimetria c'è una precisa conoscenza dello spettro utilizzato. Lo scopo di questo studio è di validare lo spettro energetico utilizzato ad ID17 per studi di MRT in modo da fornire un input affidabile per studi di dosimetria e piani di trattamento.
Lo spettro è stato calcolato grazie ad un software chiamato OASYS, sviluppato in-house ad ESRF, usato per la prima volta ad ID17, che permette di simulare un esperimento di sincrotrone virtuale. Il metodo Half Value Layer (HVL) è stato utilizzato per la validazione dello spettro calcolato. Il metodo consiste nella misurazione dell'attenuazione causata dall'inserimento di layer addizionali di materiale lungo il cammino dello spettro, con lo scopo di trovare lo spessore per il quale l'intensità del fascio si riduca a meta del suo valore iniziale. La caratterizzazione è stata ottenuta per le configurazione della beamline più utilizzate negli studi di MRT.
Gli spettri ottenuti sono stati usati per studi di dosimetria in condizioni di riferimento. I depth dose profile sono stati misurati all'interno di un cubo fatto di materiale equivalente all'acqua, usando sia una camera ionizzazione per ottenere delle misure assolute, sia dei film radiocromici per ottenere delle misure relative di attenuazione. Entrambi i risultanti data set sperimentali sono stati confrontati con i valori ottenuti mediante simulazioni Monte Carlo dello stesso setup utilizzato.
I risultati ottenuti mostrano una concordanza molto buona tra valori misurati e calcolati. Sia per le misure di HVL che per il depth dose profile con misurazione assoluta, la differenza percentuale tra i dati misurati e quelli teorici, è al di sotto del 2% e al di

sotto del 3% rispettivamente. Questi valori rispettano i criteri convenzionali utilizzati per applicazioni di RT, per i quali la dose misurata può allontanarsi di al massimo 3% da quella attesa. Per quanto riguarda le misure di depth dose profile relative utilizzando i film, i risultati sono comunque buoni, con la maggior parte dei valori entro il 3%, ma pochi valori raggiungono all'incirca il 5% di differenza percentuale con i dati simulati, il che richiede ulteriori investigazioni.
I risultati sono nel complesso molto soddisfacenti e provano che il software utilizzato per simulare lo spettro a raggi x alla beamline ID17 sia affidabile per la simulazione dello spettro reale. I profili di spettro ottenuti possono essere quindi forniti come affidabile input per futuri sviluppi di dosimetria per MRT come l'uso di sistemi di trattamento dedicati per la definizione della dose inviati in prossimi trial clinici.

Parole chiave: radioterapia per microfasci, dosimetria, radiazione di sincrotrone, spettro a raggi x

Contents

1 | Introduction

1.1. Radiation therapy for cancer

Cancer is one of the most spread and deadly diseases in the world: in 2020, only in Europe, almost 4.5 million of people contracted cancers and almost 2 millions died of it [1]. Curing cancer is one of the most challenging objectives for medicine and several techniques have been developed in the years to treat the many types of cancers that can affect different parts or organs of the human body. Radiotherapy, or Radiation Therapy (RT), has been for more than 100 years one of the most effective tools for treating cancer and still is one of the most widely used techniques, alongside chemotherapy [2]. It is a treatment modality that uses ionizing particles to eliminate tumor cells by stopping their growth and division. Different radiation types are used to perform RT, exploiting their peculiar characteristic, like selective in-depth dose deposition from protons and heavy ions. This work will focus on microbeam radiation therapy, an innovative RT approach implemented using X-rays produced by a synchrotron radiation source.
The use of ionizing radiation for the treatment of cancer dates back to the 19th century, soon after the accidental discovery of X-rays by the German physicist W. Roentgen in 1895, while he was studying cathode rays in a high-voltage gaseous-discharge tube [3].
X-rays are electromagnetic radiation of extremely short wavelengths (10^{-8} to 10^{-12} m) and corresponding high frequency (10^{18} to 10^{22} Hz). Having an atomic-like wavelength and very high energy $E = h\nu$, X-rays have the ability to penetrate optically opaque materials, like human bodies. When radiation penetrates in cellular tissues, it can result in either beneficial or dangerous biological effect. Radiation interacts with tissues by inducing biochemical changes in living cells [4]. The X-rays are attenuated when interacting with matter due to different processes: Rayleigh and Compton scattering, photoelectric effect and electron-electron pair production. Any of these processes needs a different photon energy range to happen, as can be seen in the plot of the attenuation coefficient for the water as a function of the X-ray energy, Figure 1.1. For the range of energy used in RT of up to few MeV X-rays, only two of these effects are mainly exploited:

- Photoelectric effect (Fig. 1.2a): the entire photon energy is transferred to an electron

that is bound to an atom. If the acquired energy overcomes the ionization potential, the electron gets ejected by the atom. The kinetic energy of the outcoming electron is: $E = h\nu - E_b$, with E_b the binding energy of the electron;

- Compton scattering (Fig. 1.2b): the photon transfers part of its energy to a weakly bound electron (quasi-free electron) scattering it outside the atom/molecule.

While the Rayleigh scattering could be still taken into account to generate electrons even if it is not the dominant contribution, the pair production cannot happen because it requires much higher energies than those used for RT at the synchrotron (in the order of keV).

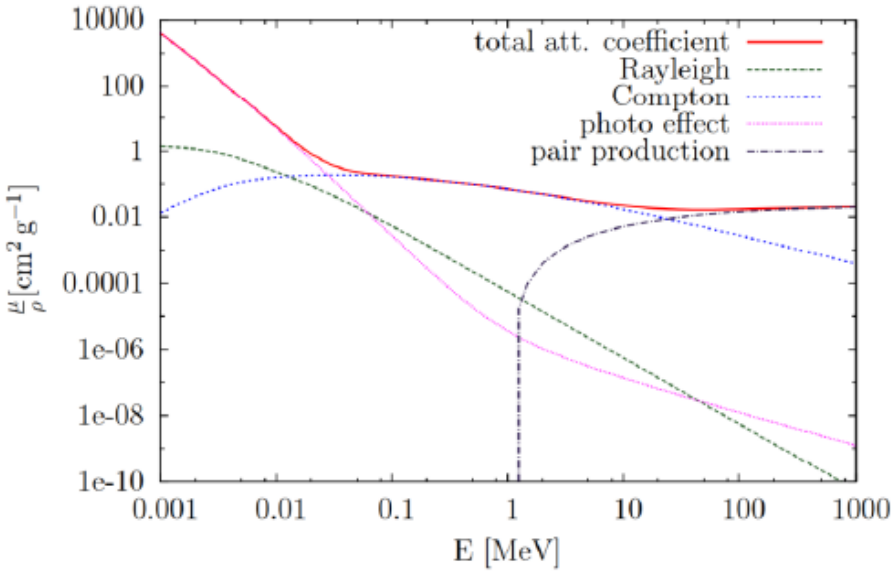

Figure 1.1: Plot of X-ray mass attenuation coefficient as a function of the photon energy in water [5].

The effects of the radiation on cells can be either direct, the break-up of DNA chains when crossed by X-rays, or indirect, when the ejected electrons, called free radicals, ionize themselves other neutral species creating a bunch of reactive particles. Genetic damage is provoked by the break of molecular bonds that are needed for cellular growth. Once cancer cells are not able to reproduce anymore they will die without generating other cells: the tumor will start shrinking in size and hopefully completely disappear [6, 7, 4]. Not only tumor cells are exposed to the radiation, indeed healthy cells are affected and destroyed as well. Luckily, the response of healthy tissue and tumor tissues to the radiation is different: the first are proliferating slowly and this characteristic allows them to have the time to repair quite efficiently. Tumor tissues instead, are proliferating quickly

due to a faster cell-cycle and a re-oxygenation process, thus having no time to react to the damages: cancer cells are more radio-sensitive [8, 9].
Conventional RT aims at maximizing the dose delivered to the tumor while keeping the dose distribution within the target as homogeneous as possible. To deliver the correct quantity of radiation dose, not only the effects of the treatment on tumour tissues, but also on the healthy ones must be considered. The two objectives cannot be fulfilled simultaneously, because both the probability of tumor control and that of undesirable side effects on normal tissues increase with the delivered dose. To measure the effectiveness of radiotherapy, the therapeutic ratio is used, defined as the Probability of Tumor Control (TCP) divided by the Probability of Complications on Normal Tissues (NTCP) [5]. The therapeutic ratio should be kept as high as possible, meaning that TCP should be maximized to increase the tumour control and in the meantime the NTCP should be minimized to reduce unwanted effects on healthy tissues. In Figure 1.3 an ideal situation is shown: the NTCP is under 0.5 while the TCP is above 0.5.

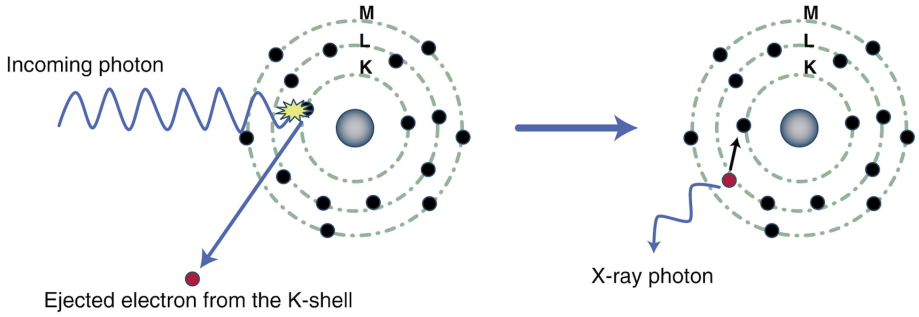

(a)

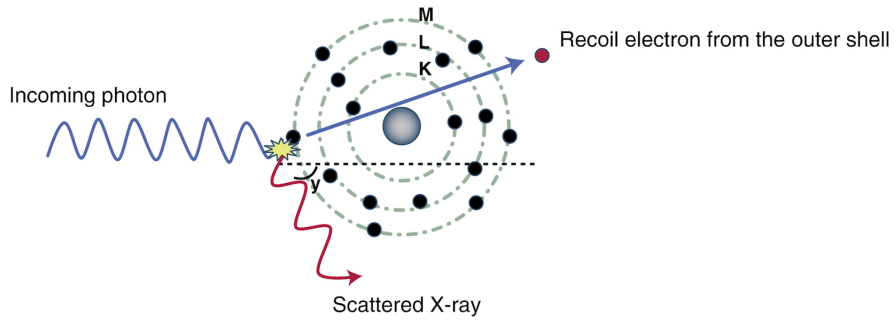

(b)

Figure 1.2: Graphical representation of the photoelectric effect (a) and of the Compton effect(b), the two main processes generating secondary electrons in RT.

A technique to achieve a better result that exploits the ability of healthy tissue to repair better and faster than tumor tissues, is the temporal fractionation of the dose. The

treatment is not performed just once, but in several sessions, fractionating the total dose delivered. In this way healthy tissue has time to repair in between the sessions and toxic effects are lower. Temporal fractionation is one of the cornerstones of modern radiotherapy [10, 11].
Therapeutic effect of radiotherapy is also maximized by increasing the geometric conformity of the dose to the tumor target: the high-dose target region is sculpted as close as possible to the target tumor volume. The majority technical advancements in radiotherapy have revolved around the improvement of the conformity of the dose to the target, to reduce collateral damages and to allow a dose-escalation [11].
Another helpful technique to increase the TCP while maintaining a low dose on healthy tissue consists in irradiating the tumor from different directions: the tumor is reached by beams entering the body from different angles, therefore passing through different healthy areas. In this way the tumor tissue is reached by a higher dose, while the dose delivered to normal tissues can be reduced obtaining the same TCP [12].

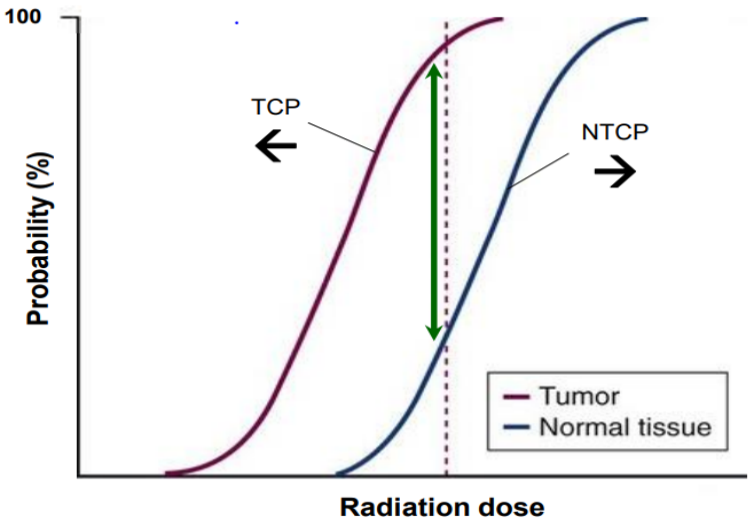

Figure 1.3: The purple curve represents the probability of tumor control (TCP), the blue curve that of complications on normal tissue (NTCP). Both the probabilities increase with the radiation dose used for the treatment: a balance between the two effects has to be found that allows to have the highest possible TCP and the lowest possible NTCP [5].

Despite significant progress throughout the decades, there are still types of cancers that are very hard to treat and have a high tax of mortality. Among these, one of the most dramatic are brain tumors in children: healthy tissues in children are reproducing very quickly as well, meaning that they are more affected by the radiation. A very high risk of complications limits the possibility for treatments and, thus, the chance of surviving.

Further improvements are necessary: the development of new treatments that could be able to overcome these limits is one of the main ways.

1.2. Microbeam Radiation Therapy - MRT

1.2.1. The spatial fractionation concept

A promising alternative to the conventional use of broad beam in radiotherapy is the spatial fractionation of the irradiating field. The idea to fractionate the conventional broad beam was introduced soon after the beginning of X-ray radiation therapy [13, 14, 15]. This technique is built upon the dose-volume effect: the tolerance of normal tissue to radiation increases as the irradiate volume of that specific tissue is reduced.
Microbeam radiation therapy (MRT) is a very promising alternative to conventional RT technique emerged in the last 25 years that exploits the concept of spatial fractionation bringing it to the extreme: the microbeams obtained by dividing the broad beam are of few tens of micrometers wide and carry a dose up to hundreds of Gy without severe damages on mature tissues.

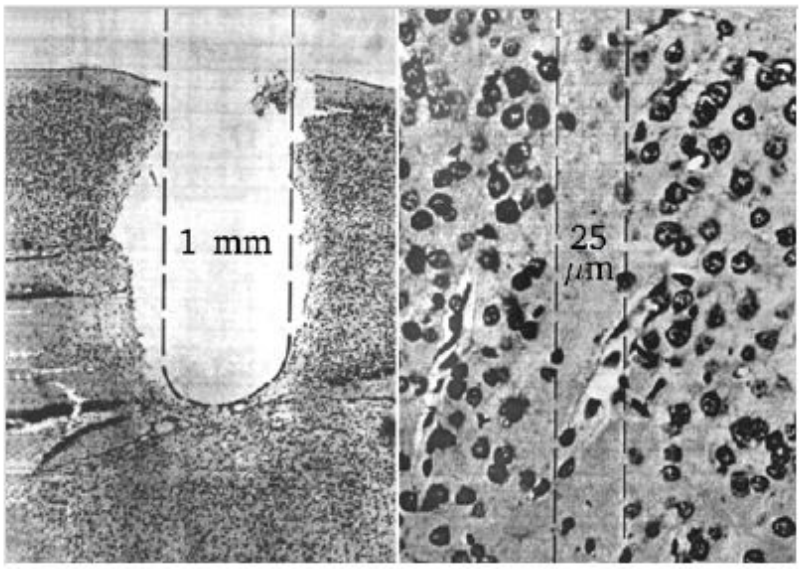

Figure 1.4: Histological images of the tissues of a mouse brain irradiated with a deuterium beam. On the left, tissue irradiated with a 1 mm wide beam of 140 Gy is completely destroyed. On the right, tissue irradiated with a 25 µm beam of 4000 Gy shows only cellular death along the beam path while the tissue architecture and the blood vessel structure is preserved [16].

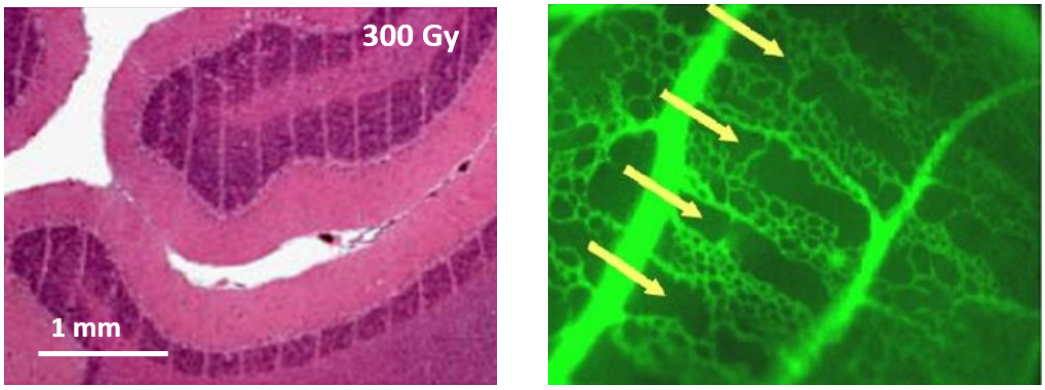

(a) From Laissue et al. [17]. (b) From Blattmann et al. [18].

Figure 1.5: (a). Piglet cerebellum 15 months post irradiation, absence of necrosis and hemorrhages, normal tissue architecture is retained. (b). Microscope picture of damage reparation of the microbeams, observed in vivo in a chick-embryo chorioallantoic membrane [17].

The concept of dose-volume effect related to the use of microbeams was first observed in the 1960s. by W. Zeman, H. J. Curtis and C. P. Baker in a study to understand the effects of cosmic radiation [16]. Using a deuteron beam passing through a mouse brain, they showed that the tolerance of the brain tissue of a mouse could be increased from 140 Gy to 4000 Gy when reducing the diameter of the beam from 1 mm to 25 µm. As shown in Figure 1.4, in the first situation the brain tissue was destroyed completely by the radiation, while in the second the tissue remained intact in the beam path and only a partial loss of cells was observed without major side effects.
Based on this discovery, MRT was first explored as a potential medical application in the early 1990s by D. Slatkin and his colleagues [19], when they proposed a therapeutic use of microbeams array. In the next years scientists repeatedly performed microbeams irradiations on animals and demonstrated the high tolerance of healthy tissues to this configuration of radiation. Laissue et al. [17] exposed two group of weanling piglets to a 15 mm × 15 mm field of 20 µm to 30 µm wide microbeams with 100 µm spacing delivering a dose up to 600 Gy. Despite the absorption of such high-dose by the cerebral tissues, the animals didn't show any behavioral or neurological difference with respect to unirradiated groups (Figure 1.5a). Dilmanian et al. [20] showed that the tolerance of normal tissue mainly depends on the valley dose with only a weak influence from the peak dose.
The therapeutic efficacy of MRT has been proved by a number of mechanisms:

- Reduction of the proliferation capability of cancer cells after the MRT irradiation, while normal tissues retain their architecture and show an ability to launch a coor-

dinated repair (Figure 1.5b) [21];

- Differential transcriptomic effects on the tumor and on normal tissue: these modulated transcripts are mainly related to the regulation of cell-cycle and to the immune/inflammatory response and can partially explain the control of tumor growth by MRT [22, 23];
- Tumor micro-vasculature has a greater radio-sensitivity to MRT compared to that of a normal brain tissue which has important implications on the ability to repair damages of the cells [24, 25].

All these good properties result in a higher probability of survival after the irradiation with the respect to normal radiation therapy treatments (Figure 1.6) [26].

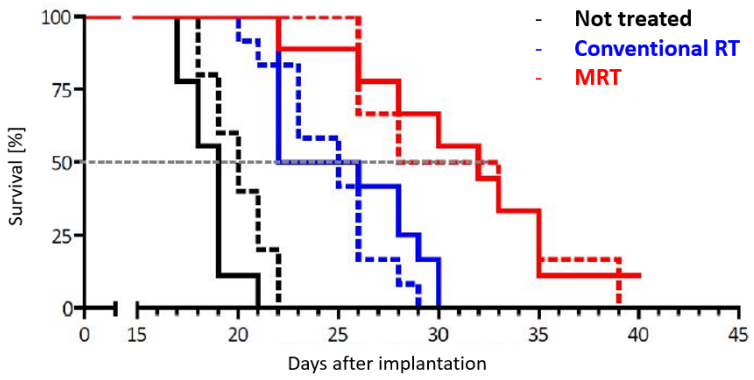

Figure 1.6: Effects of different treatments on the probability of survival for animals carriers of cancer [26].

1.2.2. Further research related to MRT

MRT is still in pre-clinical phase: no human patients have been treated yet. The development of safe protocols to maximally exploit the radiobiological properties of MRT is the challenge. One of the most attractive possible future uses of MRT is for the treatment of brain tumors, especially in in pediatric cases that are otherwise untreatable. The research is right now focused on the treatment of large animals with spontaneous tumors that are a potential good model for further studies on human patients.
Another phenomenon under study is the Flash effect in RT. Flash RT is an emerging technique that uses ultra-high dose-rates in order to deliver the whole needed dose in a time of fraction of seconds. This technique seems able to effectively eradicate tumor while reducing the occurrence and severity of early and late complications [27, 28, 29].

Synchrotron radiation sources provide radiation dose-rates in the Flash regime, and at the ID17 the Flash effect was always unconsciously included in MRT experiments. Further investigation can help with the characterization of both Flash and use of microbeams effect.
The use of microbeams can be helpful in a vast range of clinical scenarios [11]:

- *MRT as a boost for conventional radiotherapy.* Exploiting the normal tissue sparing properties of the spatial fractionation, MRT could be used as a booster within conventional radiotherapy regimen: the peaks of dose would enhance the tumour control while the valley dose would match the daily prescribed dose [30];
- *MRT as a primer for drug delivery.* Exploiting the effect of MRT on the cardiovascularity of tumoural tissues, the treatment could be used to enhance drug delivery by opening a window of higher vascular permeability in the cancer cells [31]. Preclinical studies have demonstrated the enhancing effect of MRT while combined with a range of drugs [32, 33];
- *MRT as a micro-surgical tool in neurological disorders.* MRT shows the potential to alleviate the symptoms of neurological conditions: it could be used to transect neuronal pathways to modulate or suppress the networks responsible for abnormal movement [34, 35].

1.2.3. MRT physics characteristics

In MRT the spatial dose-fractionation is achieved on a microscopic scale: fields are characterized by an array of 25 – 100 µm wide beams separated by a 100 – 400 µm pitch, with a length up to some centimeters, defined by the extent of the radiation field. Today, the most used configuration in MRT is of 50 µm wide beamlets, spaced by 200 or 400 µm pitch. This kind of array creates a periodically alternating dose profile, defining peak and valley dose regions, as shown in Figure 1.7. Along the microbeam path, that correspond to the peaks region, the dose can be up to 100 times higher than the dose in the valley regions (between two consecutive peaks), due to the photon scattering into the target volume. The in-beam doses are up to some hundreds of Gy, i.e. orders of magnitude greater than those delivered in conventional radiotherapy. Managing and controlling the valley dose is of huge importance: the valley dose must be lower than the tolerance limit of the tissue in order to prevent tissue destruction and allowing the tissue to partially or entirely repair. A parameter that is widely used to characterize a MRT irradiation is the Peak to Valley Dose ratio (PVDR): once the maximum valley dose to send to healthy tissues has been defined, starting from the following several factors, the PVDR is obtained

depending on:

- Energy of the microbeams;
- Field size;
- Size of the microbeams;
- Distance center-to-center of the microbeams;
- The tissue volume irradiated;
- The chemical composition of the irradiated tissue.

From the PVDR profile, the needed peak dose to deliver is obtained.

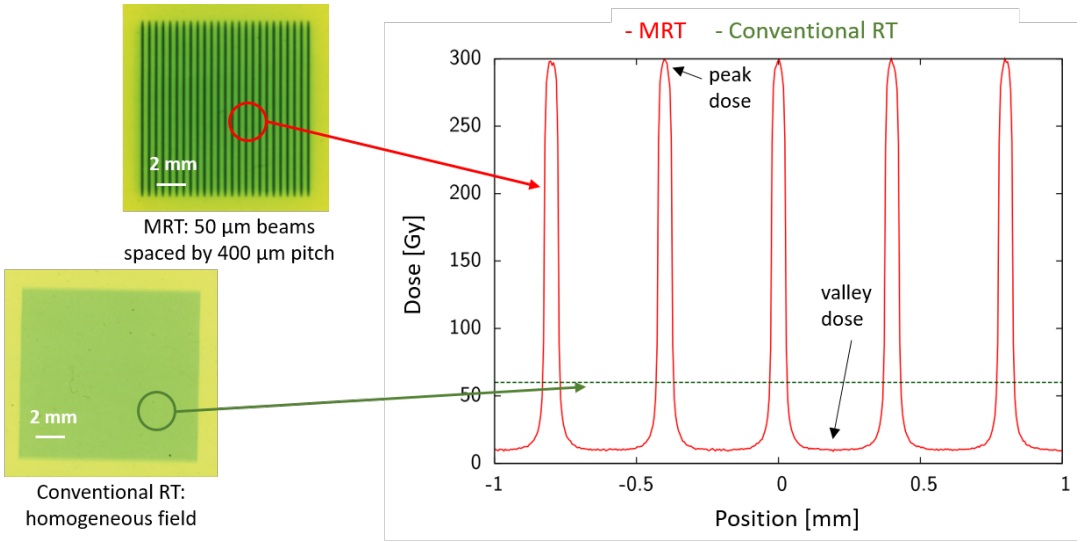

Figure 1.7: The images on the left are can two examples of irradiated radiochromic films showing the difference between conventional RT and MRT in terms of beam profile. The figure shows the corresponding dose profile for both RT and MRT: the latter shows the described profile with peaks and valley of dose [36].

In the 50 keV to 200 keV energy range used for MRT, the produced secondary electrons from primary photons are low-energy, therefore they can travel only up to around 100 µm before thermalizing, generating the peak penumbra. The valley dose, instead, extends farther from the microbeam path: it is generated by secondary electrons scattering from secondary photons, that can travel inside the tissues in the order of millimeters.
Another microbeam characteristics required for effective MRT studies is that an ultra-high dose rate must be reached. The physiological motion of the organs, including cardio-synchronous pulsation of blood vessels and respiration, can strongly affect the dose dis-

tribution if the tissue displacement occurs on a range equal or larger than the beam dimension during irradiation time, by violating the dose-volume principle. The motion inside the human brain can reach 2 mm/s velocity [37]. To mitigate this effect, a fast irradiation in short time is necessary.
A minimal beam divergence is as well needed to maintain the array geometry at microscopic scale: the beam shape and the distance in between microbeams must be preserved in the passage through the target.
Only synchrotron radiation from high-powerful sources is nowadays able to satisfy all these requirements and deliver the optimal peak-valley dose [18]. At the ESRF - ID17 Biomedical beamline, the dose rate that can be reached is 16 kGy/s, allowing for dose deposition of several hundred of Gy with exposure times in the order of 10 ms. Also a low horizontal divergence of about 1 mrad can be reached at the synchrotron, producing quasi-parallel beams.
Only in the late 90s the use of microbeams for treatments became technically possible thanks to the intense and high energy second generation synchrotrons that are able to deliver the required microbeam quality. Nowadays MRT is in the pre-clinical development phase at a small number of synchrotrons across the world: the ESRF - European Synchrotron Radiation Facility (France), the ANSTO - Australian Synchrotron (Australia), the Canadian Light Source (Canada) and the Spring-8 (Japan).
The possibility to develop compact sources to make possible to perform MRT not only in synchrotron radiation facilities is under study [38, 39], and it will be a game changer in the development of MRT techniques.

1.3. The European Synchrotron Radiation Facility - ESRF

The synchrotron radiation was first "discovered" in 1944 by D. Iwanenko and I. Pomarentchouck [40]: they observed a loss of electromagnetic energy through an emitted radiation. In 1947, at the General Electric Laboratories, for the first time, a blue light ray exiting from a transparent glass tube of an electrons accelerator was observed [41]. Synchrotron Radiation (SR) was finally recognized in 1960s as light with exceptional properties:

- High Brightness: SR can be extremely intense and highly collimated;
- High Polarization: SR light is highly polarized;
- Wide Energy Spectrum: the SR light is emitted over a wide range of energies with

a continuous spectrum.

Electrons, when accelerated and deviated by magnetic field, emit energy as electromagnetic radiation. For non-relativistic electrons the emission is isotropic around the particle. When electrons are accelerated to nearly relativistic speed, instead, they're emitted tangentially to the electron direction and the radiation field take the form of a cone with a typical opening angle of $\frac{1}{\gamma}$, with

$$\gamma = \frac{1}{\sqrt{1 - \frac{v^2}{c^2}}} \tag{1.1}$$

where v is the speed of the electrons and c that of light.
Nowadays, synchrotrons are large scale research infrastructures optimized for the production of high-flux photon beams by accelerating electrons to relativistic energy: the ESRF realized in Grenoble, France, is one of these facilities.

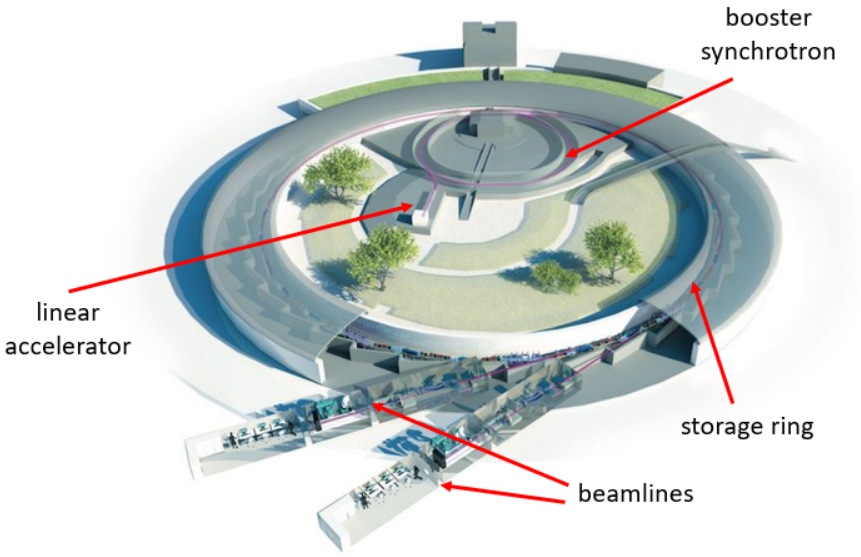

Figure 1.8: Schematic of the ESRF structure, highlighting the principal components of a synchrotron facility: the linear accelerator, the booster synchrotron, the storage ring and the beamlines. Credits to ESRF [42].

At the ESRF electrons are produced in bunches by an electron gun and accelerated in a LINAC (a linear accelerator) up to 200 MeV. Then, the electrons are transferred in a booster synchrotron where they are accelerated up to the relativistic energy of 6 GeV. Finally, electrons are injected into the storage ring where they are kept at the final energy

of 6 GeV energy for the generation of X-ray radiation. The storage ring is a tube of 844 m of circumference where electrons circle for hours at a speed close to that of light. Therefore, the booster is paired with the storage ring only few minutes every day when, almost every hour, new bunches of electrons are sent to in the storage ring. This compensates the electron loss and maintains the desired ring current level. This procedure is called "refill". In Figure 1.8 is shown a schematic of the ESRF synchrotron structure highlighting the main structures [42].
All the storage ring is in Ultra High Vacuum (UHV) conditions to avoid the electrons from losing significant energy by scattering with remaining particles. As the bunches of electrons travel around the ring, they pass through different types of magnets that, bending their trajectory, generate the emission of radiation. The magnets can be:

- Bending Magnets (BM): dipoles magnets situated in the curved section of the ring. They bend the trajectory of the electrons tangentially to the plane of the beam, permitting the closure of the circle. While the trajectory of the electrons is bent, they emit SR: bending magnets are used, thus, as non-tunable sources of SR. The radiation from a BM covers a wide and continuous spectrum, from microwaves to hard X-rays, and is much less focused than that of an insertion device;
- Insertion Devices (ID): are situated in the straight section of the ring and can be either undulators or wigglers. These magnetic structures are made up of a complex array of small magnets that force the electrons to follow an undulating or wavy trajectory. The generated beam is much more focused and brilliant than that of a BM, and the photons are emitted only at certain energies. A more detailed description of the insertion devices is in the section 1.4.1.

Other type of magnets with different characteristics and functionalities are present as well: quadrupoles provide focusing forces to keep the electron beam transverse dimension small and sextupoles are employed to compensate for loss of beam chromaticity around the electrons revolution. A storage ring section schematic is shown in picture 1.9 where he different types of magnets are highlighted.
When SR is emitted, electrons are loosing part of their energy: devices that can restore the lost energy are situated along the storage ring, otherwise the electrons would quickly become unable to circulate. The devices that fulfill the purpose are called Radio-Frequency cavity (RF): they have an inner cavity where electrons pass through and get re-accelerated by an electric field to compensate for their energy loss. The electric field in the cavity is made to oscillate at a given frequency: a synchronization between the electrons and the RF device is, thus, necessary, otherwise the electrons would feel a different acceleration at any time they enter the cavity. The synchronization process is the reason why electrons

cannot circulate continuously, but must be split in bunches.

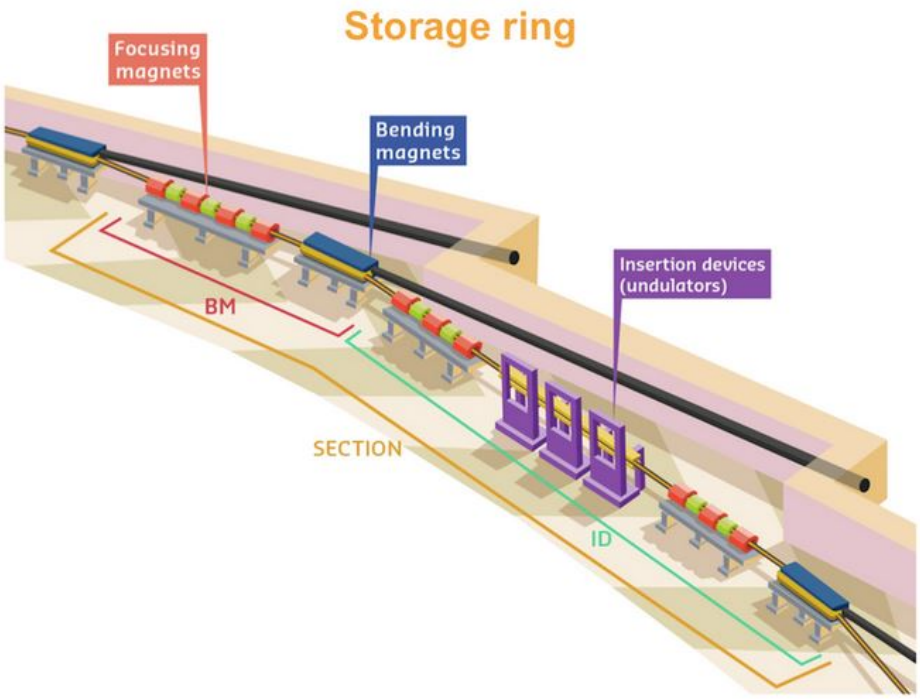

Figure 1.9: Graphical representation of a section of the ESRF storage ring. Bending magnets are responsible for curving the electron trajectory as well as to make them emit radiation, while insertion devices are mainly used to generate X-rays radiation used for experiment. Focusing magnets can be either quadrupoles or sextupoles, used to not allow the spreading of the electron beam during the circulation. Credits to the ESRF [42].

X-rays beams finally emitted by the storage rings, from each bending magnet or insertion device, are directed toward the experimental stations named beamlines. Each beamline is designed to conducct a specific type of research using the incoming beam of X-rays. There are more than 40 beamlines at the ESRF, named with an acronym that is either BM, if they X-ray radiation is coming from a bending magnet, or ID, when the beam is instead coming from an insertion device. The radiation is mainly transported into a pipes under UHV conditions. This tube connects the front-end section, where either the BM or the ID is placed, to the first experimental chamber, called hutch, of any beamline.

1.4. The ESRF - ID17 Biomedical beamline

The ID17 is the Biomedical beamline at the ESRF. It was designed with the main purpose to support new discoveries and innovative works in the fields of radiotherapy and medical

imaging.
ID17 is one of the longest ESRF beamlines, presenting two experimental stations. The first one is served by a polichromatic beam and it is located around 40 m from the radiation source while the second experimental station, served by monochromatic beam, is located around 150 m from the X-ray source point. Three insertion devices are installed in the front end section of the ID17 beamline: one undulator named u126 and two wiggler devices named w125 and w150. Only the w150 wiggler is used to generate the X-ray beam for MRT experiments.
The structure of the beamline is the following:

- Front End Section: connect the storage ring to the first optical hutch, all the different insertion devices are located here;
- First Optical Hutch (OH1): this section contains the optical instrumentation necessary to shape and tune the beam energy according to the requirements of different experiments;
- First Experimental Hutch (EH1): located around 40 m away from the wiggler. Here, a polychromatic beam is available with dose rate up to 16 kGy/s that made this the favorable location for MRT.
- Control Cabin for EH1: next to EH1, contains the control systems and PCs used to monitor the experiments;
- Beam Transfer Tunnel: UHV tunnel to transport the beam from the EH1 to the OH2;
- Second Optical Hutch (OH2): here a monochromator is installed to tune the beam to a specific energy (that for the ID17 is between 30 keV and 200 keV) obtaining a monochromatic beam, used for biomedical imaging;
- Second Experimental Hutch (EH2): this hutch located around 150 m from the wiggler source. Such a long distance allows the use of the beam up to 15 cm wide, useful to satisfy the requirements of biomedical imaging;
- Control cabin for EH2: for EH2 also, a control room is located nearby the hutch to allow the researcher to follow and monitor the experiments.

A schematic of the ID17 beamline is shown in Figure 1.10 where all the elements just listed are highlighted.

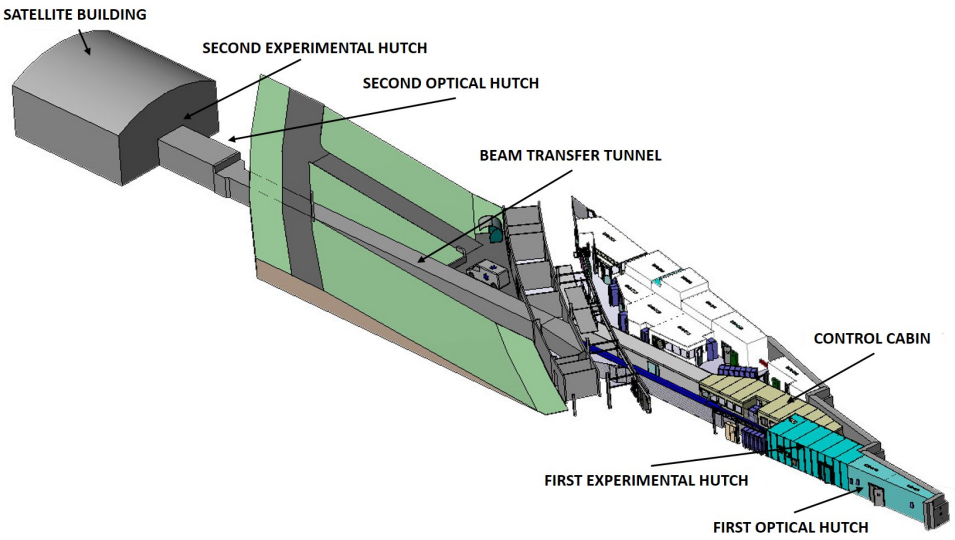

Figure 1.10: Schematic of ID17 beamline showing all the principal sections composing it. Credits to the ESRF [42].

1.4.1. Front End section and wiggler X-ray source

Wiggler and undulators are built by a series of bending magnets of constant length of few centimeters with alternated polarity, that generates a magnetic field. The electrons crossing the wiggler are forced to oscillate with an undulatory trajectory perpendicular to their motion direction. Wiggler provides a strong magnetic field that result in a wide horizontal opening angle of the emitted radiation. Wigglers and undulators are distinguished by the deflection parameters K (the meaning of the parameter is explained better at the end of the section), defined as $K = \delta\gamma$, where δ is the maximum deflection angle and γ the previously defined relativistic parameter from equation 1.1. Wigglers have $K >> 1$ because the electron beam has a large divergence, while undulators have $K \leq 1$. Undulators generate a partially coherent radiation generated by superposition of individual undulations of the electrons, leading to a very narrow cone of radiation and a spectrum characterized by spikes, the so-called undulator harmonics. Wigglers instead, deliver a continuous spectrum with a much higher intensity and a broader fan on the horizontal direction, therefore these devices are more suitable to produce X-ray radiation for MRT experiments [43, 44, 45, 46].

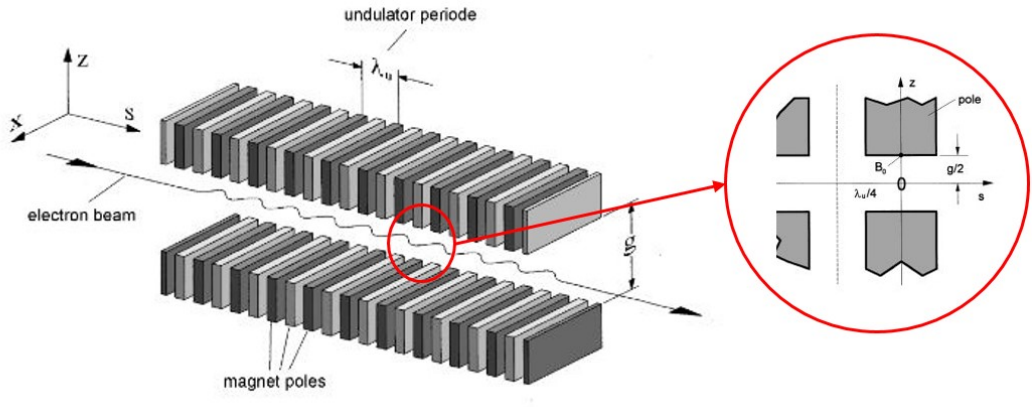

Figure 1.11: Wiggler insertion device. In the red circle the poletip field is shown assuming position s = 0 at the center of the magnet [44].

Focusing on the wiggler, we can describe its magnetic field by its scalar potential

$$\phi(s,z) = f(z)cos(2\pi\frac{s}{\lambda_u}) = f(z)cos(k_u s) \tag{1.2}$$

where s is the coordinate along the beam axis and z is the vertical direction. λ_u is the periodicity of the magnets (Figure 1.11). We can apply the scalar potential instead than the vectorial one because there are no electrical currents around the beam. By applying Laplace equation

$$\nabla^2\phi(s,z) = 0 \tag{1.3}$$

to (1.2), we obtain:

$$\frac{d^2f(z)}{dz^2} - f(z)k_u^2 = 0 \tag{1.4}$$

The solution for the equation (1.4) is:

$$f(z) = Asinh(k_u z) \tag{1.5}$$

Substituting (1.5) into (1.2) we get:

$$\phi(s,z) = Asinh(k_u z)cos(k_u s) \tag{1.6}$$

Now we can derive the magnetic field by deriving the scalar potential (1.2):

$$B_z(s,z) = \frac{\partial\phi(s,z)}{\partial z} = k_u A cosh(k_u z) cos(k_u s) \tag{1.7}$$

To find the constant value A we start from the known value B_0 at $z = \frac{g}{2}$, that is the poletip field (Figure 1.11):

$$B_0 = B_z(0, \frac{g}{2}) = k_u A cosh(k_u \frac{g}{2}) = k_u A cosh(\pi \frac{g}{\lambda_u}) \tag{1.8}$$

The constant A becomes:

$$A = \frac{B_0}{k_u cosh(\pi \frac{g}{\lambda_u})} \tag{1.9}$$

and thus the field:

$$B_z(s,z) = \tilde{B} cosh(k_u z) cos(k_u s) \tag{1.10}$$

with the peak field

$$\tilde{B} = \frac{B_0}{cosh(\pi \frac{g}{\lambda_u})} \tag{1.11}$$

From this expression can be clearly seen that the peak field decreases very rapidly with the gap height g (Figure 1.12). This field calculation is a simple analytic approximation. For the experiments that will be discussed in the next chapters the magnetic field of the wiggler w150 when the gap is $g = 24.8$ mm has been measured. It comprises 10 magnetic field periods spaced $\lambda_u = 15$ cm, hence reaching a peak value of 1.62 T. The measured field is shown in Figure 2.3 where it can be seen that the profile is not perfectly sinusoidal as it is obtained from the simple analytic approximation.

The oscillating field B of the insertion device, forces the electrons to oscillate as well, and when their trajectory is bended the X-ray radiation is emitted.
The wiggler is the most appropriate source for X-rays for MRT, providing a continuous photon flux spectrum and a sufficiently large horizontal amplitude for the desired size of the radiation field. That is obtained due to large value of the wiggler parameter K. By continuing with the analysis, the trajectory of electrons inside the wiggler can be obtained as well as the maximum trajectory angle:

$$\Theta_w = \frac{1}{\gamma} \frac{\lambda_u e \tilde{B}}{2\pi mc} \tag{1.12}$$

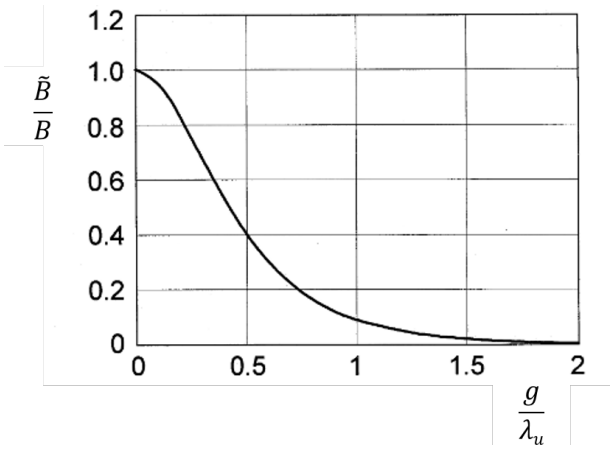

Figure 1.12: Wiggler field behavior as a function of the gap [44].

That is defined as:

$$\Theta_w = \frac{K}{\gamma} \tag{1.13}$$

Thus:

$$K = \frac{\lambda_u e \tilde{B}}{2\pi mc} \tag{1.14}$$

For a gap of 24.8 mm a maximum field of 1.62 T is obtained, leading to $K = 22.65$: the large value of K means that the horizontal opening angle of the radiation from the w150 wiggler source is large. The obtained spectrum at ID17 has low vertical divergence of 0.1 mrad while the horizontal divergence is higher, 3.3 mrad, obtaining a flat, but with an high horizontal fan, beam. Practically, the maximum beam divergence accepted for experiments is of around 1 mrad, defined by a fixed beam aperture between the front end section and the OH1.
The typical spectrum profile of an insertion device shows a rapid loss of intensity for increasing photon energies. Only 1% of the photons generated by the ID17 w150 wiggler have energy higher than 300 keV.
Fundamental is also to provide a high photon flux for the required dose rate delivery in MRT irradiation. That is available with the high brilliance quality of the synchrotron radiation. Brilliance is defined as the flux [ph/s] normalized to the source area [mm^2], to the energy range of the photon as 0.1% of bandwidth, and to the angular divergence of the photons both in horizontal and vertical direction [mrad^2]. A high value of brilliance, up to 10^{22}, is reached at the synchrotron with the new EBS.

1.4.2. First Optical Hutch

From the wiggler the X-ray beam travels inside a long pipe under vacuum conditions along the beamline. All the components in OH1 are kept under vacuum conditions and several valves and Be windows allow the isolation between different sections in vacuum (schematic in Figure 1.13).
Inside the optical hutch, two pairs of motorized slits, called primary slits, define a beam of rectangular shape by absorbing photons exceeding the predefined dimension.
Subsequently, the photon beam pass through a series of water-cooled attenuators to remove by absorption the photons with energies below 50 keV, and therefore harden the X-rays spectrum. Energies below 50 keV are, in fact, not effective for MRT, being strongly attenuated close to the target surface. The combination of five filters made of C, Al and Cu, each of them with more possible choices of absorbing thickness, is available. The configuration of filters is chosen depending on the type of spectrum that need to be used for the experiments: if a high intensity beam is required, a configuration with thin attenuators is used, while instead, when a harder spectrum, more suitable for future clinical applications, is wanted, that is obtained by further filtering the low energy photons using thicker filters. More details on the filter configuration used for MRT applications will be presented in section 2.1.2.
After the attenuators, an ionization chamber (IC0) can be moved into the beam for monitoring purposes. It will be explained more in detail in the next chapter, in section 2.1.2.
To accurately control the exposure time a fast shutter is present, that allows a minimum exposure time of 5 ms with a precision of $\pm$ 0.5 ms. It is composed of two 15 mm thick blades made of tungsten carbide (WC) each coupled to an actuator magnet. The electromagnets works in asynchronized way such that both blades are kept out of the beam when the sample irradiation is performed. As soon as the beam must be cut, the supply for the electromagnets is turned off and the blade goes back to its rest position inside the beam. A photon absorber, corresponding to a 40 mm thick Cu block, protects this delicate "blade" shutter from most of the incoming radiation.
A lead safety shutter with its photon absorber is located at the end of the OH1 to block the propagation of the radiation in EH1 when not necessary.

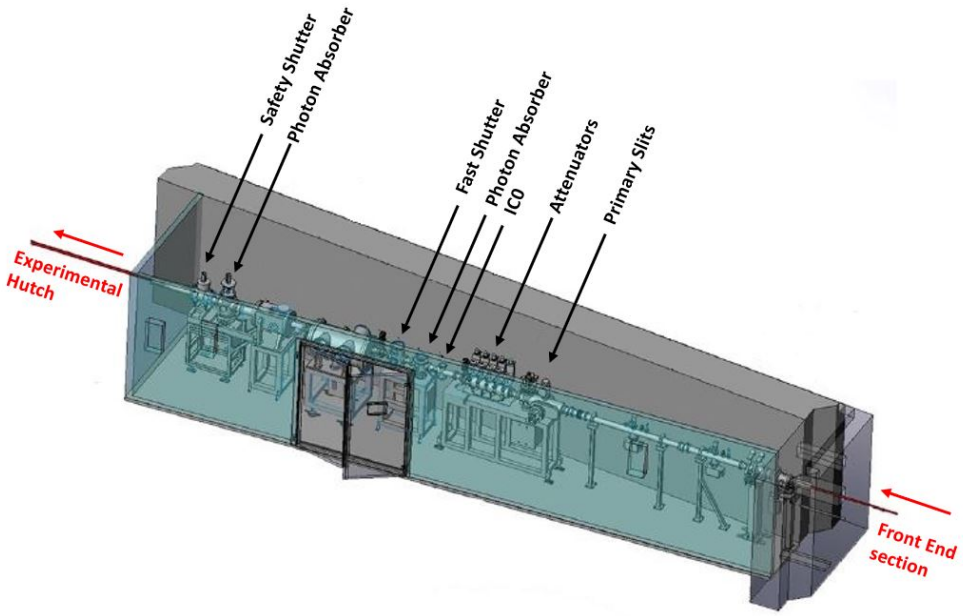

Figure 1.13: ID17 First Optical Hutch. The main components used to define the beam characteristics for MRT irradiation are highlighted in the figure.

1.4.3. First Experimental Hutch

In the experimental hutch the MRT experiments take place. The vacuum pipe ends at the entrance of this chamber, hence the components are no longer in vacuum, but in air, placed on an optical table (Figure 1.14).
A second fast shutter, named "rotary shutter", is the last component used to stop the beam before the target. The rotary shutter is realized by two rotating tungsten carbide blades that are turned parallel to allow the X-ray beam passing between them. This rotary shutter is less mechanically delicate with respect to the blade shutter, but also less precise. This shutter is mainly used during imaging experiments where several opening-closing cycles are necessary in a rapid sequence, but the radiation intensity is significantly lower compared to that of RT and does not damage the shutter.
A couple of mechanical slits define the final horizontal width of the beam, while four vertical apertures of 51 µm, 102 µm, 520 µm and 795 µm allow the definition of the beam vertical height. Only the central area of the beam is selected, to keep the intensity profile of the irradiation as flat as possible.
Another monitoring device named IC0bis, is composed by two equal PTW 34070 Bragg peak chamber and can be located along the beam path. The precise description of this device is present in section 2.1.2. When irradiation in a clinical scenario is performed, the IC0bis is the last component placed in front of the target when irradiation in a clinical

scenarios are performed. These detectors monitor in real time the dose delivered to the target and, if necessary, can trigger a signal to stop the irradiations when safety parameters are not respected.
Due to the intrinsic properties of the wiggler radiation source, the limited vertical dimension of the beam does not allow the irradiation of targets higher than few millimeters. To overcome this limit, the target is scanned vertically in front of the beam. At ID17 a 3-axis-Kappa-type goniometer is paired with translational motors, allowing the positioning of the target in the beam with micrometric precision. The target can be vertically scanned along a range of around 14 cm, with a constant speed between 1 and 100 mm/s.

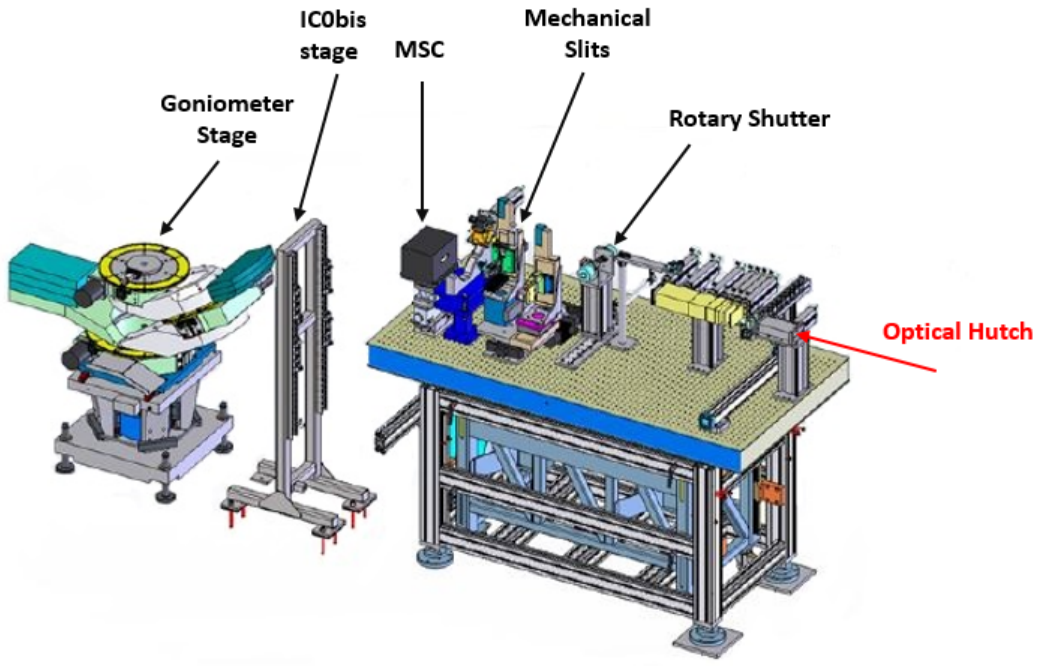

Figure 1.14: Graphical representation of a section of the EH1 at ID17. The technical drawing shows the optical table with the main components used for MRT and the goniometer stage where the sample is placed for irradiation.

To achieve the creation of microbeams, before the target is necessary to place a multi slit collimator (MSC) [47], i.e. a block of metal with equidistant apertures that define the periodicity of the microbeams (shown in Figure 1.15). The X-rays beam is, in this way, transformed into an array of beamlets. Different combinations of 25 – 100 µm wide beam with 100 – 1000 µm pitch have been tested, but the favorable solution for MRT is the one of 50 µm wide apertures and a center-to-center spacing of 400 µm.
The metal used to realize the MSC is tungsten carbide (WC) that allowed a machine

process with the required sub-micrometric precision. The MSC is situated inside an aluminum box with a nitrogen cooling system to dissipate the heat produce by the photon absorbed by the metal. The box is mounted on a rotational stage that allows a precise alignment of the MSC inside the beam.

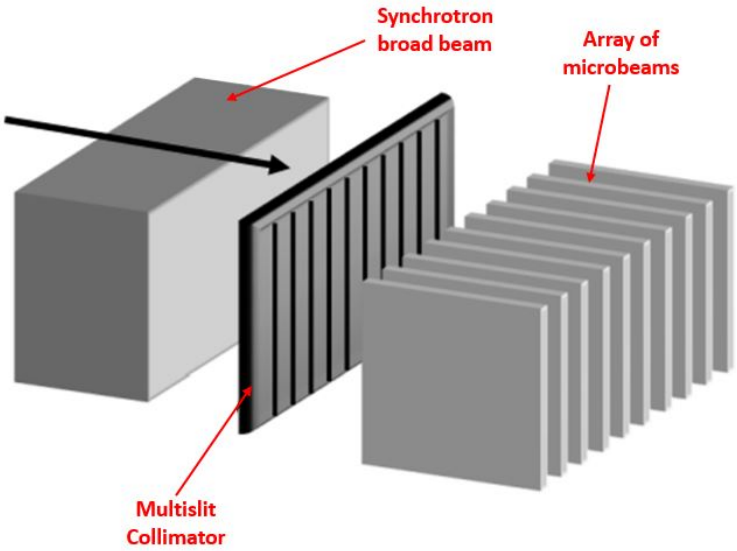

Figure 1.15: Graphical representation of the Multislit Collimator, where the broad beam is transformed into an array of beamlets.

1.5. Motivation for the study

Reliable and robust dosimetry protocols are at the basis of any radiation therapy: a high accuracy on the dose delivered during radiotherapy is mandatory for a positive treatment outcome, both for broad beam and microbeam studies. The absorbed dose by the material directly depends on the depth of penetration of the photons and on the range of length that scattered secondary electrons can travel, thus a precise knowledge of the spectrum is at the basis of each RT treatment.

The energy spectrum of the pre-clinical beam at ID17 have been already measured few years ago using the powder diffraction technique [48]. Later, Crosbie et al. [49] validated a calculated spectrum using attenuation measurement because various modifications were made to the ID17 beamline in preparation of veterinary trials.

In 2015 the ESRF started the new ESRF Extremely Brilliant Source (EBS) project that was concluded with the renovation of the storage ring in 2020.

The improvement of the storage ring combined with the renovation of components of the ID17 beamline in recent years generated the need for a new complete characterization of the X-ray spectrum used for irradiation at ID17, in order to perform an accurate dosimetry in preparation of veterinary trials.
The raw spectrum of the insertion device has been simulated for the first time using the OASYS software [50], developed internally to the ESRF (see section 2.1.1). The validation of the spectra has been performed following the Half Value Layer protocol, the same used by Crosbie et al. [49], i.e. validate a calculated spectrum using attenuation experimental data. The newly defined spectra have been used to perform depth dose profile measurements in order to verify that the simulated and measured dose delivered agreed, confirming the goodness of the simulated spectra. For these measurements, a standard configuration for reference dosimetry using a water-equivalent plastic phantom and a homogeneous beam was used.
The spectra resulting from the study will be at the basis of the future experiments and projects related to radiation therapy at the ID17 beamline. The simulated spectra will substitute the already existing ones for all the simulations preceding the experiments. The definition of a new reference dataset for irradiation in MRT is now possible and can be considered the natural continuation of this work.

1.6. Outline of the thesis

The outline of the work is as follow:

- Chapter 2 presents the experimental methods used to to perform the validation of simulated spectra, as well as the theoretical methods to obtain these former. At first, the OASYS software that is able to reproduce the X-ray radiation from the wiggler and an in-house developed code that calculate the final spectra at ID17 are presented. To validate these data the approach used is the Half Value Layer method, that consists in a measurement of the attenuation of the beam.
  The newly defined spectra are then used to perform dosimetry following the depth dose profile method, that is presented in this chapter. It consists in absolute dose measurement with an ionization chamber inside a water-equivalent plastic phantom, as well as relative dose measurements using radiochromic films as detectors. Both these two set of experimental values are compared to calculated data from Monte Carlo simulations of the interaction of radiation with matter. Two different algorithms used for the Monte Carlo simulation are presented in this chapter as well, the conventional method and an innovative hybrid approach for calculation.

The uncertainty budget related to all the different methods is presented at the end of the chapter.

- Chapter 3 presents all the results obtained from both calculation and experimental methods explained in the previous chapter: the different set of measured data are compared to the respective simulated data to reach the validation of the hypothesis.
- Chapter 4 presents the discussion about all the results presented in the previous chapter, as well as with possible improvement in the methods and comparison to previous literature works.
- Chapter 5 presents the main conclusion of the work.

2 | Methods and Instrumentation

2.1. X-ray spectra definition

The starting point for the characterization is the simulation of the expected spectrum at ID17 to be compared with experimental measurements. The simulation of the spectrum starts with the photon emission through the wiggler, followed by the passage through all the optical components of the beamline: absorbers, detectors and slits. The different steps leading to the final simulation of the spectrum were performed using different methods, that will be described in the following sections.

2.1.1. The OASYS software

For the simulation of the raw spectrum, the OrAnge SYnchrotron Suite (OASYS) platform was chosen. This is a software developed in-house at the ESRF, with the goal of enabling scientists to fully model virtual synchrotron experiments. OASYS relies on existing well known codes and libraries that are available thanks to the open-source community. The open-source mechanism allows the use of valuable tools developed at synchrotron facilities and made available to the community, with credits given to the authors and supporting institutions [50, 51].
With the OASYS software it is possible to perform simulation of:

1. The electron beam: description and propagation;
2. The photon source: generation of X-ray beams emanating from either bending magnets or insertion devices;
3. The beamline optics: description and effect of the optical elements or components of the beamline on the X-ray beam;
4. The interaction of the sample with the photon beam: detection and analysis of the scattered radiation to obtain information about the operation of the instruments or the sample itself.

OASYS provides an intuitive graphical interface for interactive simulations. It is presented as a graphical workspace (canvas) that can be filled with applications (widgets) from different simulation packages, called add-ones. The add-ones are connected by "wires", channels for exchanging information, that can simulate the propagation of the beam from one component to the next one. Each widget has several functionalities: it contains the input parameters, triggers a calculation or a data flow and displays the results. These functions are all embedded in a single window, as shown in Figure 2.1 [51].
For the characterization of the X-ray spectra used for the radiation therapy study at ID17 beamline, the OASYS – ShadowOui widgets were used to reproduce the beam generated by the w150 wiggler and passing through the slits used to define its final shape. ShadowOui is a code library implemented in Python that uses the ray tracing technique to perform the wanted simulations [52, 53]. This technique can be used to model most of the effects that limits the performance of X-ray optical elements like aberrations and errors in optical surfaces. Raytracing is a technique that uses Monte Carlo simulation to study the interaction between the incident photon beams and optical elements.
Widgets based on the ShadowOui library are embedded in OASYS. To simulate the raytracing with the Shadow library, there are two options: either use the OASYS widgets on the user-friendly platform or directly launch the Python code, which can also be extracted from the widgets.

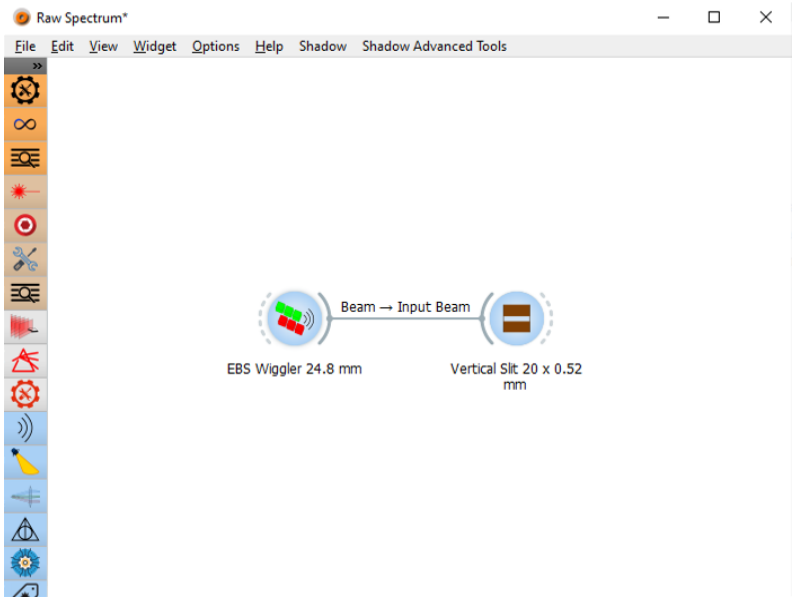

Figure 2.1: OASYS software layout. The two widgets used to calculate the raw spectrum are shown, connected by the wire that passes the signal generated by the wiggler widget to the vertical slit widget, which defines the final dimension of the beam used during experiments.

For the simulations of the raw spectrum, two widgets were used:

- Wiggler widget (Figure 2.2a): this widget allows the simulation of the X-ray beam generated by the wiggler source. It is possible to adjust the basic settings for the raytracing Monte Carlo simulation, such as the number of rays used, the seed and the energy range. The source setting can also be changed directly through the widget: the electron energy and current in the storage ring, the parameters of the storage ring and the parameters of the wiggler. The magnetic field of the wiggler can be either the conventional field (the sinusoidal field described in section 1.4.1), set with the wiggler parameters used (gap, period, number of periods), or the measured magnetic field of the wiggler, which is more precise because it considers the limited dimension of the system.
  The wiggler widget provides the diagrams of the behavior of the electrons (trajectory, velocity, curvature) and the generated raw spectrum;

- Screen – Slits widget (Figure 2.2b): this widget of the ShadowOui library allows to insert an element in the beam which can be either a slit, i.e. an element that cuts off part of the incoming photons, limiting the dimension of the beam, or a screen, that cuts off part of the photons by absorption.
  The distance between the wiggler source and the element can be chosen, as well as the dimensions and position of the element within the beam, and thickness and absorbing material when used as a screen.

In the study, the parameters of the EBS storage ring (6 GeV and 200 mA) were used and the magnetic field chosen was the measured one at a wiggler gap of 24.8 mm (Figure 2.3). To our knowledge, this is the first time that the measured magnetic field of the w150 wiggler was used for the calculation of the raw spectrum. The number of simulated rays was set to 10^7 to achieve the desired precision in simulating the raw spectrum. For the second widget, a vertical slit of 20×0.52 mm^2 (horizontal and vertical, respectively) was simulated as used in the experimental sessions. The horizontal dimension of the beam is defined by the motorized primary slits in the OH1, at about 38 m from the wiggler source, while the vertical dimension of the beam is defined by one of the four fixed-dimension vertical apertures installed in EH1 a few meters ahead of the target.
The output file from OASYS is the raw spectrum at ID17 in terms of the spectral flux for each energy considered: from 100 eV to 600 keV with a step of 100 eV. The spectral flux is usually given by the number of photons $N(E)$ versus the photon energy E, per unit time and per unit energy bandwidth [54]:

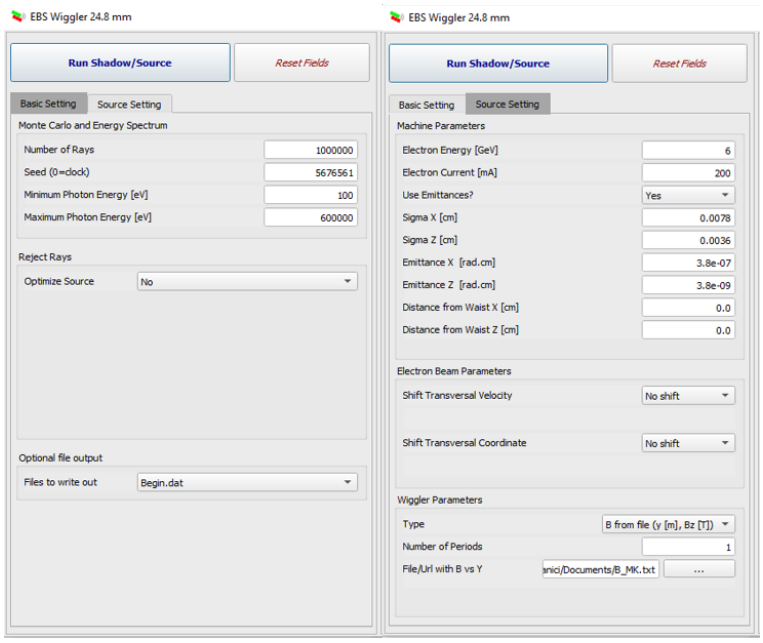

(a)

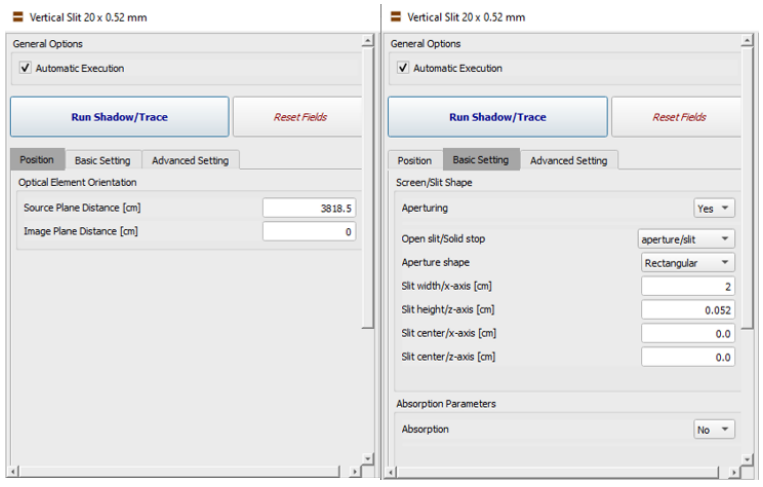

(b)

Figure 2.2: (a) Screenshot of the Wiggler widget specifications chosen for the simulation. (b) Screenshot of the Vertical Slit widget specifications chosen for the simulation.

$$\frac{Number\ of\ photons}{s \times Energy\ Bandwidth} \tag{2.1}$$

where the energy bandwidth is given as a value that depends on the energy and is usually defined as 0.1% of the photon energy:

$$Energy\ Bandwidth = \frac{\Delta E}{E} = 10^{-3} = 0.1\%BW \tag{2.2}$$

That is, if the brilliance is 3.8 10^{13} photons/s/0.1%BW at 9 keV, the source emits 3.8 10^{13} around 9 keV in the bandwidth of $\Delta E = 10^{-3} \times E = 9$ eV, i.e., in the energy interval [8995.5, 9004.5] eV.

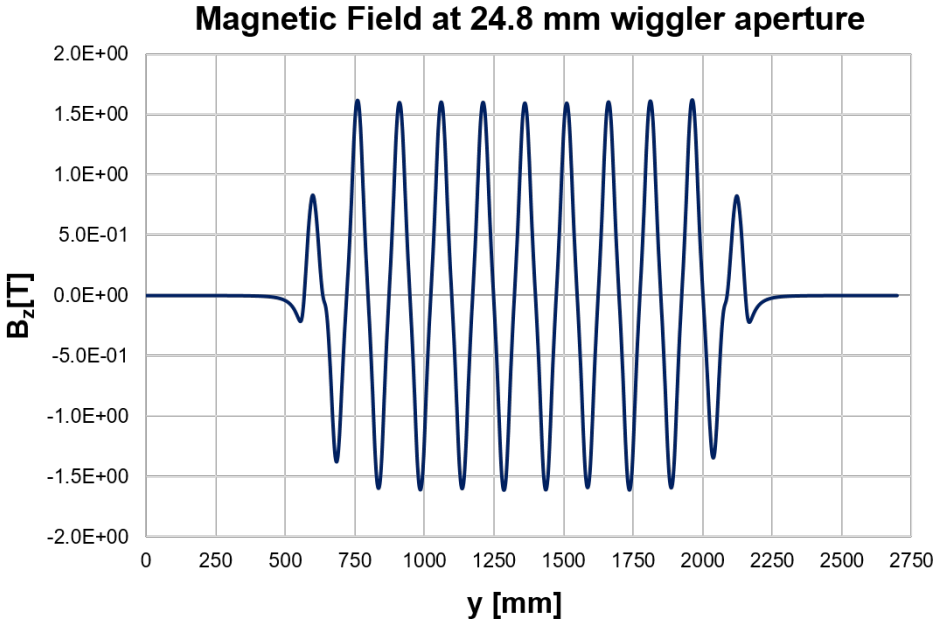

Figure 2.3: Measured magnetic field of the wiggler w150 when the gap is set to 24.8 mm.

2.1.2. Spectra configurations

Different spectra were studied at ID17 corresponding to the configurations most used for MRT experiments. The different configurations are possible by varying the attenuators and the monitoring detectors within the beam. As explained in section 1.4.3, the beam encounters different materials along its path to cut off its low-energy photons component and tune the average beam energy. There are a few Be and Al windows in the vacuum tubes to separate the different sections, with a fixed total thickness of 2.3 mm for the Be and 0.5 mm for the Al. For the experiments of RT, the following attenuating elements can

be chosen: one attenuating element made of glassy carbon, two aluminum filters and two copper filters, which are the most attenuating. The available thickness of the attenuating elements is listed in Table 2.1.
The monitoring devices are two: the IC0 in OH1 and the IC0bis in EH1 (already introduced in sections 1.4.2 and 1.4.3, respectively). The IC0 is a Compton scattering ionization chamber made of two pairs of Al plates serving as electrode, each 0.5 mm thick [55]. Both surfaces of each electrode are covered with an extremely thin layer of Au, for a total thickness of 0.28 µm. The ICObis is composed by two identical PTW 34070 Bragg peak chambers [56]. Figure 2.4 shows a picture of the PTW 34070 Bragg Peak chamber and its schematic. Each of the two PTW detectors has an entrance window of 0.335 cm PMMA, 0.002 cm graphite and 0.01 cm varnish, for a total thickness of 0.347 cm. The entrance window is followed by an air cavity of 0.2 cm and by an exit window of 0.738 cm PMMA. The chamber should be well approximated by 22 mm PMMA. To verify this assumption each spectrum with IC0bis was also simulated with 22 mm PMMA instead of the IC0bis.

	Abs 1: C	**Abs 2: Al**	**Abs 3: Al**	**Abs 4: Cu**	**Abs 5: Cu**
Thickness 1 [mm]	none	none	none	none	none
Thickness 2 [mm]	1.41 (graphite)	0.28	0.64	0.30	4.60
Thickness 3 [mm]	1.13 (glassy)	0.64	1.17	1.04	0.071 Au
Thickness 4 [mm]	2.83 (glassy)	1.4	2.62	1.40	0.68

Table 2.1: Attenuators available in OH1 for tuning the photon beam. For each attenuator column only one option can be selected at a time.

In Table 2.2 all the spectra configurations investigated for this work are presented.
The most used spectra are those corresponding to configuration 2, 3, and 8. Spectrum 2 is the spectrum traditionally referred to as "conventional" and used in MRT studies. It is the most intense spectrum used in experiments. Spectrum 3, which has a thicker copper layer than the previous one, is the Preclinical spectrum used in preclinical studies and has a higher average beam energy, but lower intensity than the conventional spectrum. Spectrum 8 is instead referred to as the Clinical Spectrum and was obtained with the beamline setup in the configuration intended for future clinical applications. It has the filter configuration of the PreClinical spectrum and both IC0 and IC0bis monitoring

detectors in the beam.

(a) (b)

Figure 2.4: (a) Picture of a PTW-Bragg peak chamber. (b) Schematic of the thickness of composing materials of one of the two Bragg peak chambers composing the IC0bis. The grey regions are the chamber walls made of PMMA, while in blue is represented the air cavity.

Spectrum 1 is that with the lowest attenuation from filters, therefore it's the spectrum with the overall maximum intensity, but similar properties to the conventional MRT spectrum. From Spectrum 4 to 6 the filters configuration remains the same and all the monitoring devices are inserted one at the time. This was done to characterize individually the monitoring devices in order to recognize easily possible differences with respect to the theoretical model. In Spectrum 4 the IC0 is tested alone, in Spectrum 5 and 6 the PMMA and the IC0bis are tested, respectively. Being the 22 mm of PMMA supposed to attenuate as the IC0bis, these two spectra are supposed to be the same. Same for the Spectrum 7, supposed to be the same as the 8, being the Clinical spectrum but with PMMA instead of IC0bis.

2.2. The Half Value Layer method

2.2.1. The Lambert-Beer law

The Lambert-Beer law describes the attenuation of a monochromatic beam of photons passing through a material. It is represented as:

Spectrum	1	2: Conv	3: PreClin	4	5	6	7	8: Clin
Be window [mm]	2.3	2.3	2.3	2.3	2.3	2.3	2.3	2.3
C [mm]	1.13	1.13	1.13	1.13	1.13	1.13	1.13	1.13
Al [mm]	0.28	0.28	0.28	0.28	0.28	0.28	0.28	0.28
Al [mm]	0.64	1.17	1.17	1.17	1.17	1.17	1.17	1.17
Cu [mm]	0.3	0.3	1.4	1.4	1.4	1.4	1.4	1.4
Cu [mm]	0.68	0.68	0.68	0.68	0.68	0.68	0.68	0.68
Al window [mm]	0.5	0.5	0.5	0.5	0.5	0.5	0.5	0.5
IC0	NO	NO	NO	YES	NO	NO	YES	YES
IC0bis	NO	NO	NO	NO	NO	YES	NO	YES
PMMA	NO	NO	NO	NO	YES	NO	YES	NO

Table 2.2: Spectra configuration: from 1 to 8 there is an increasing presence of filtering layers. Monitoring devices are inserted to validate their structural characteristics from Spectrum 4.

$$I = I_0 e^{-\mu x} \tag{2.3}$$

where I_0 is the an-attenuated intensity of the beam before passing through the filtering material, I is the intensity transmitted through the attenuating material of thickness x and μ mm^{-1} is the linear attenuation coefficient of the material for the given energy of the beam. μ is defined as the mass attenuation coefficient $\frac{\mu}{\rho}$ in $\frac{kg}{m}$, where ρ is the material density. By multiplying the mass attenuation coefficient to the density of the material, the linear attenuation coefficient is obtained.
In a polychromatic beam, like that obtained from the wiggler at ID17, the linear attenuation coefficient of the material is not unique but depends on the energy of the photons passing through it. The equation 2.3 thus, cannot accurately model the entire system. What must be used, instead of just one linear attenuation coefficient, is a different attenuation coefficient for each energy of the beam. The attenuation coefficient, in fact, depends on the scattering processes taking place when the photons hit the material. Each of these processes has a different cross-section depending on the energy of the incoming photons, so it must be specific for each energy.
When performing HVL calculation, the goal is to find the thickness x of the material that can attenuate the intensity of the beam to half of its initial value, that means:

$$\frac{I}{I_0} = 0.5 \tag{2.4}$$

$\frac{I}{I_0}$ is called Intensity Ratio (IR). The thickness for which the IR is 0.5 is called first Half Value Layer (HVL1). The concept can be extended to secondaries half value layers: HVL2 is the thickness for which 75% of the intensity of the beam is absorbed by the material, thus $IR = 0.25$, while HVL3 is the thickness for which $IR = 0.125$, so only 12.5% of initial intensity is transmitted.

2.2.2. Final spectra simulation

After the calculation of the raw X-ray spectrum it was necessary to compute the different spectra profiles used at ID17 for RT experiments. For the purpose, a Python code was developed in-house to simulates the presence of the filters and monitoring devices through which the beam passes. The code (attached in appendix A), takes as input file the Raw Spectrum obtained with the OASYS software: it consists in a text file containing the brilliance of the beam for each previously defined energy step (section 2.2.1). Based on the Lambert-Beer law extended for a polychromatic beam, each filter is represented by its attenuation coefficient for each of the photon energies of the incoming beam. The attenuation coefficients used are those of the XRayDb library for Python, that provides atomic data, characteristic X-ray energies, and X-ray cross sections for the elements. The provided data from XRayDb library are taken from the NIST database and put in a new database for X-ray spectroscopy calculations [57]. The same approach was used for monitoring devices: each of them is divided into the individual materials with the corresponding thickness. The only missing simulating element is the varnish layer on the IC0bis, since the actual composition of the material used is not known. Being a very thin layer of non highly absorbing material, the result should not be worsen by this missing part.
The code allows to simulate each of the spectra under study by just changing the thickness of the filtering components and of the monitoring devices that can be "inserted" in the beam. For each energy, the Lambert-Beer law is applied with the correct attenuation coefficient giving as output the spectrum after each filtering object. For each energy the applied formula is thus:

$$\frac{I}{I_0} = e^{-\sum_L \mu_E x} \tag{2.5}$$

where L is the total path of the beam through all the attenuators and monitoring devices, and μ_E is the attenuation coefficient, which depends on the photon energy and on the material traversed.

2.2.3. HVL calculation

Once the final spectra at ID17 were obtained, the second step consisted in simulating the presence of additional layers in the beam, the materials whose purpose was to attenuate the beam by half of its initial value. To obtain the expected values for HVL using the simulation, the same approach defined above to quantify the attenuation of the filters in OH1 was used. Additional layers of Cu or Al, are inserted into the beam by mean of their attenuation coefficients for each energy step.
The program is able to directly provide the expected value for the HVL1 or secondary HVLs: it loops by increasing the material thickness, computing at each step the value of $\frac{I}{I_0}$. When the IR is close enough (the stopping interval can be chosen as a parameter depending on the desired precision) to the wanted value (0.5 for HVL1, 0.25 for HVL2 and 0.125 for HVL3), it gives as an output the Cu or Al thickness that define the HVL.
Another possibility is to obtain as output file all IRs for a given range of the material thickness used in HVL measurements. In this way, it is possible to make a comparison with the exact thickness used for the measurement as explained in the following section.
The final brilliance of the beam, for each energy step after the total additional layer thickness, is also given as an output file.

2.2.4. HVL experimental setup

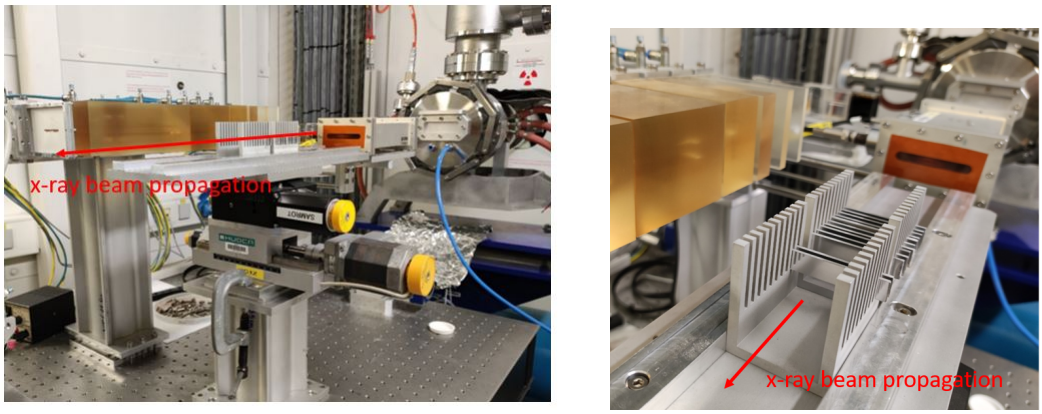

(a) (b)

Figure 2.5: (a) Photo of the experimental HVL setup: extra Al are positioned inside the beam path on the top of stage to allow the alignment. (b) Photo of the Al extra layers inside onto the slit holder.

The experimental measurement for HVL consisted in the insertion of different layers of copper or aluminum sheets with purity above 99.9% inside the beam path. The extra

layers were placed at the beginning of EH1, on some slits to hold them perpendicular to the beam, as it can be seen from the pictures in Figure 2.5. The attenuation to the intensity of the beam due to their presence in the path is measured.
There were available 19 sheets of Al with thickness around 1 mm and 19 with thickness around 2 mm. Of Cu, instead, 20 sheets with thickness around 1 mm, 12 around 0.5 mm and 9 with thickness around 0.1 mm were available. The thickness of each sheet was measured before the irradiation by mean of a caliper.
Measurements were done for each of the eight spectra previously defined (section 2.1.2) with both Al and Cu sheets: in total 16 different sets of data were obtained, two different sets of measures for each of the spectra. 12 data points were taken for each setup: based on the prediction obtained with the simulations, the total thickness of the extra sheets to insert in the beam was chosen in order to obtain an IR curve with a point around every 7-8% points of attenuation. The experimental points are then compared to the values obtained with the Python simulation; the fitting of the experimental curve allows as well to obtain a precise value for all the wanted HVLs.
The aperture of the slits to define the vertical height of the beam was chosen to be 0.52 mm, therefore the final equivalent beam of 20×20 mm^2 at the measuring point was obtained scanning vertically the detector of 20 mm. The attenuators setup and the presence of monitoring device were chosen depending on the desired spectrum.
PTW PinPoint ionization chamber was used to measure the transmitted signal. The detector and the procedure used are explained more in detail in the next section (2.3.1).
The IR for each point is obtained by dividing the normalized dose measured (D_n [Gy/mA]) for the normalized dose of the spectrum under examination without any extra layer added (D_{n_0}). The normalized dose is obtained by measuring with the PinPoint IC the total dose (D [Gy]) carried by the beam and dividing it by the current of the storage ring at the moment of the irradiation I [mA].

$$IR = \frac{D_n}{D_{n_0}} \tag{2.6}$$

For statistic each measure was taken three times.

2.3. Absolute dosimetry

Experimental dosimetry is fundamental for the validation of the dose delivered during RT treatments. It is a challenging measure, due to the extreme conditions under which MRT is performed: high doses used in MRT, as well as the high dose rate of the synchrotron

X-ray sources can lead to the saturation of the detectors.
Absolute dosimetry is performed in a homogeneous field before microbeam irradiation, following as close as possible the International Atomic Energy Agency - IAEA protocol TRS 398 for reference dosimetry [58]. The most important dosimetric variable is the mean absorbed dose (D), that is the quantity of energy deposited by particles per unit mass:

$$D = \frac{dE}{dm} \tag{2.7}$$

Being photons uncharged particles, they're indirect radiation source because the dose is actually deposited by secondary electrons generated by the interaction of the photon beam with the matter. The dose is measured in Gy that corresponds to one $\frac{J}{kg}$.

2.3.1. PTW PinPoint ionization chamber

Ionization Chambers (ICs) are the standard dosimeter in conventional radiation therapy: they are used to perform absolute dosimetry, but don't have enough spatial resolution for dosimetry at micrometric scale, that needed for MRT. The validation of a treatment planning system (TPS) in conventional RT is usually performed with IC and it is approved only if the calculated dose and the measured dose match within a 3% of error considering all the possible correcting factors and uncertainties [58].

Figure 2.6: PTW PinPoint 31014 [59]

The PTW PinPoint 31014 [59] (in Figure 2.6) is the detector used for the measurement performed in this study. It is a cylindrical IC, recommended for medium energy kilovoltage

X-ray beam, therefore is used as the reference dosimeter at ID17. It has a very small sensitive volume of only 0.015 cm^3 allowing measurements of radiation fields down to 20 $\times$ 20 mm^2.
Cylindrical ICs consist of an air cavity where ions are generated by the interaction between the incident radiation and the air. The inner wall of the IC cavity is conductive and serves as external electrode, while the collection electrode is located at the center of the air cavity. Applying a polarization voltage of few hundreds volts between the two electrodes, the motion of the created charges toward one of the electrode is induced, avoiding their recombination. If the applied voltage is positive, the collecting electrode detects positive ions. A guard electrode prevents the signal electrode from detecting leakage current and parasitic signals coming from regions with a distorted electric field. The IC measures the quantity of charge collected in Coulombs (C), directly proportional to the absorbed dose, and the signal is read by an electrometer [60]. The absorbed dose to water $D_{w,Q}$ is given by:

$$D_{w,Q} = M_Q \times N_{D,w,Q_0} \times k_{Q,Q_0} \tag{2.8}$$

where N_{D,w,Q_0} is the IC calibration factor in Gy per nC applied to convert the measured current into absorbed dose: it is dosimeter specific and provided by a metrology lab in terms of absorbed dose in water at reference beam quality Q_0. If the measurement are performed at a beam quality Q different from Q_0 a correction factor k_{Q,Q_0} needs to be applied. PinPoint IC is calibrated at PTW with a TH200 beam quality, that means a mean energy of 109 keV and a spectrum quality closest to the Clinical spectrum used during MRT irradiation [60, 61]. M_Q is the raw reading M_{raw} corrected by some factors that considered the influence of different quantities by mean of correcting factor k_i:

$$M_Q = M_{raw} \times k_i \tag{2.9}$$

k_i contains different correcting contributions that need to be taken into account when reading the IC values [60]:

- Correction for Temperature and Pressure $k_{T,P}$: the mass of air contained in the cavity depends on the atmospheric condition (T and P) at the time of the measurements that can differ from those at the time of the calibration. The $k_{T,P}$ correcting factor accounts for this effect:

$$k_{T,P} = \frac{P_0 T}{T_0 P} \tag{2.10}$$

where $T_0 = 293.2$ K and $P_0 = 1013.2$ hPa are respectively the temperature and air pressure at the time of calibration, while T and P are those at the time of the measurement;

- Correction for Polarity effect k_{pol}: parasitic radiation-induced current arising from secondary electrons generated in the wall and in the electrodes of the IC can cause a polarity effect. The potential difference between the guard and the central electrode can as well distort the electric field inside the cavity causing a polarity asymmetry. Both these effects are taken into account by this correcting factor;
- Correction for Ion Recombination k_s: if the applied voltage to the IC is not high enough, the current measured during irradiation will be dependent on the applied voltage, because the ions created inside the air cavity will recombine before reaching the electrode, resulting in an underestimation of the dose. That's why IC needs to be used in saturation regime, where all the charges are collected due to a small ion recombination. However, the IC readings still need to be corrected for this effect by applying the recombination correction factor k_s;
- Correction for Electrometer Calibration k_{elec}: factor determine by the metrology lab when calibrating the electrometer and the IC.

When using the PinPoint IC, its plastic cover was put on, that is helpful to guarantee the electronic equilibrium, i.e. to avoid electrons escaping from the cavity during the measurement not being balanced by incoming.

2.3.2. Dosimetry for HVLs

The first experiment performed was the verification of HVLs by measuring the attenuation generated by the addition of extra layers to the beam path. The PinPoint IC on its own was centered into the irradiating field and placed in air on the goniometer sample stage. To cover the whole irradiating field during the measurement, the PinPoint is vertically scanned inside the beam, as shown in Figure 2.7: by doing that the IC measures the absorbed dose D [Gy]. The dose rate $\dot{D}$ [Gy/s] is then obtained as:

$$\dot{D} = \frac{D \times v}{z_{beam}} \tag{2.11}$$

$$\dot{D}_{scaled} = \frac{D \times v}{z_{beam} \times I} \tag{2.12}$$

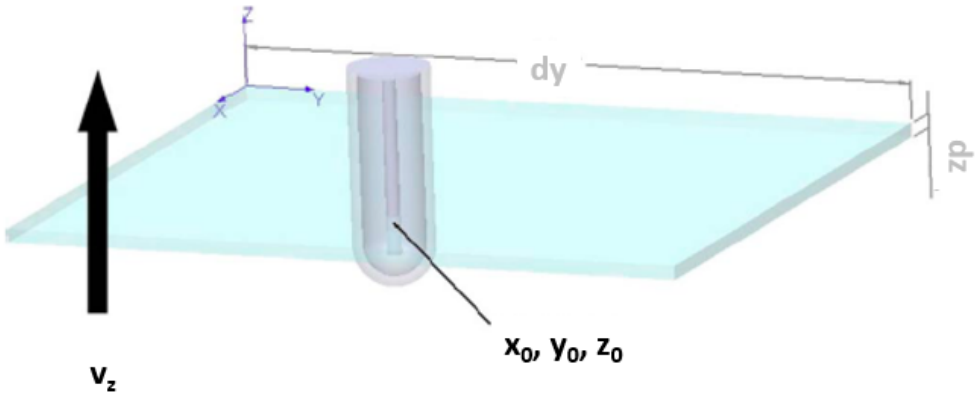

Figure 2.7: Scanning movement of the PinPoint IC inside the beam to measure the dose rate [62]

where z_{beam} is the beam height [mm], v the scan speed, I the current of the storage ring and $\dot{D}_{scaled}$ is the dose rate divided by the current $\frac{\dot{D}}{I}$. The vertical scanning speed for the measurement was set to 20 $\frac{mm}{s}$.
The measure was performed for each different configuration defined by changing the extra layer configuration to obtain the complete IR curve as explained in section 2.2.4.
To take into account the correcting factors, the T and P inside the experimental hutch were measured before the start of the irradiation series: the measured value was inserted in the electrometer giving as a result the initial $k_{T,P}$. Temperature and pressure were monitored during the irradiation, by placing two thermocouples close to the PinPoint IC: that was done to control the variation of the factor from the initial measured value during the whole experiment.

2.3.3. Reference dosimetry

Reference dosimetry consists in the determination of the absorbed dose to water under reference conditions. Reference conditions means to measure the dose in the same conditions in which the IC was calibrated. The protocol TRS 398 [58] for medium energy kilovoltage X-ray beams prescribes to measure the dose in water at 2 cm depth under a 10×10 cm^2 field size.
Differently to dosimetry for HVL calculation that was performed in air thus, for this experiment a LAP EASY CUBE phantom is used (in Figure 2.8) [63]. It is a water equivalent plastic cubic phantom with a total dimension of $180 \times 180 \times 180$ mm^3 and removable

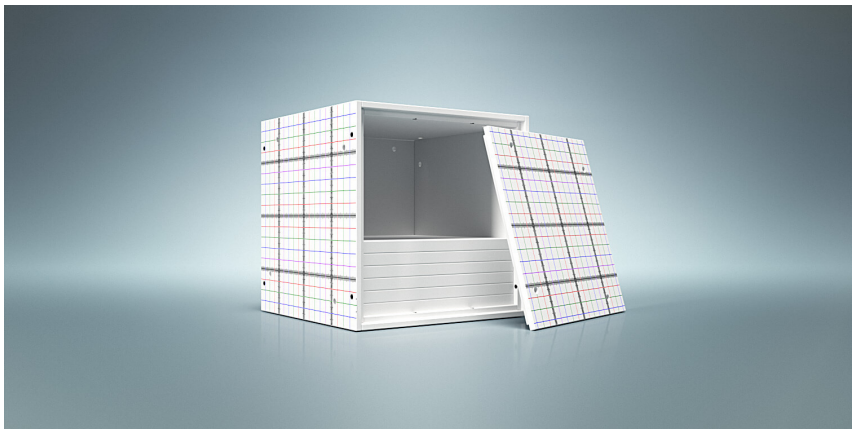

Figure 2.8: LAP EASY CUBE. On the inside are shown some of the 1 cm thick slabs, one of which was drilled to create a hole for the PinPoint IC. [63]

slabs 10 mm thick. One of these slabs has a machined hole used for the insertion of the IC. This kind of device is used instead of a water tank to simplify operational aspects of the measurement.

The reference position for the reference dosimetry is fixed at 20 mm from the surface of the phantom, as recommended in the TRS 398 protocol, thus the slab with the hole for the PTW PinPoint is positioned first behind the front wall of the cube. The active volume of the IC is aligned in the in the center of the 20 $\times$ 20 mm^2 irradiating field: in fact, the current maximum horizontal beam dimension for MRT is in the order of 30 mm, limited by the component's window through which the beam passes. This does not allow to use a field size as prescribed by TRS 398 protocol, hence a 20 mm wide beam is adopted which is reliably defined.
In the same way described in the previous section 2.3.2, the phantom loaded with the PinPoint detector is scanned in front of the beam, measuring the dose in reference conditions.

2.3.4. Depth dose profile

For the purpose of spectrum validation, the concept of reference dosimetry can be extended to obtain the profile of the dose measured at different depth inside the water cube: this method is called depth dose profile. The measured value is then compared to the calculated dose value in the same points by using MonteCarlo (MC) simulation (see section (2.5).
To perform depth dose profile, instead of measuring just at 2 cm deep, the slab containing the PinPoint is positioned at different depth inside the water equivalent cube. For this

study the dose was measured at 10 different depth: 1, 2, 4, 6, 8, 10, 12, 14, 16 and 17 cm deep inside the cube. Three measures of the dose were taken at each depth in order to make an average and diminish the measurement error. From the measured value the IR was calculated as previously explained in section 2.2.4, but in this case for the normalization the value in reference conditions, i.e. 2 cm in deep, was chosen.
The depth dose profile was performed for six different spectra: the three main one, Conventional, Clinical and Preclinical, but also for Maximum Intensity one, the Preclinical one with the IC0 as well and the Clinical with the PMMA in place of the IC0bis.

2.4. Relative dosimetry

2.4.1. Radiochromic films

To reinforce the dosimetry study and provide two sets of experimental data obtained with different detectors, depth dose profile measurement using radiochromic films was performed. Radiochromic films (RCF) are a valid detector to perform dosimetry with microbeams due to their high spatial resolution. Application of radiochromic films for radiotherapy is possible since a sensitive dye was developed allowing radiation measurements. The radiochromic films used in the study are the GAFchromic films produced by the International Speciality Products Inc. (ISP) [64].

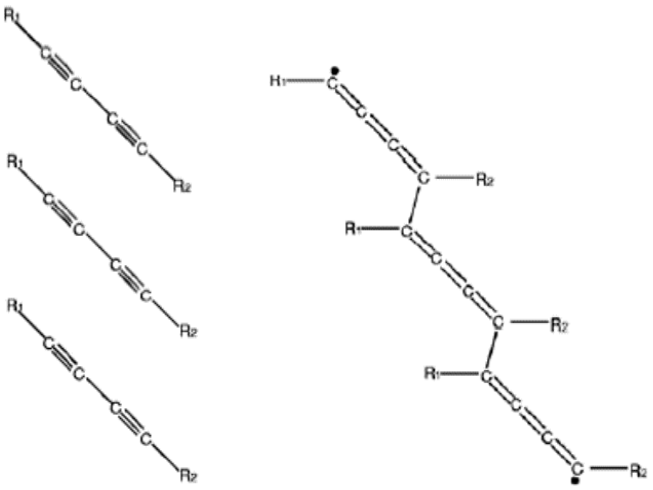

(a) (b)

Figure 2.9: (a) Pentacosa-10,12-diyionic acid molecules before exposure to radiation. (b) The molecules in figure (a) have undergone a polymerization process during the exposure to radiation that results in a polymeric chain. The process was driven by the R_1 and R_2 end groups. Images from [65].

Radiochromic films are made of a thin flexible sheet of plastic coated with the active material responsible for the radiosensitivity. The latter is generally a diacetylene, such as pentacosa-10,12-diyionic acid, the one chosen for recent Gafchromic films [66, 67, 65]: when exposed to heat or radiation the material undergoes a polymerization process by creating polymer chains that increase in length with the level of exposure. As a consequence of the process, the optical density of the film changes. In Figure 2.9a are shown some monomers, with a length in the order of 0.75 µm: those molecules undergo a polymerization process when exposed to light, driven by the R_1 and R_2 end groups, resulting in the molecule shown in Figure 2.9b.

The film used for this study are the HD-V2 model of the Gafchromic films that are nominally able to measure doses between 10 Gy and 1 kGy. They are nominally made of 97 µm thick plastic layer with 12 µm thick active layer, as shown in Figure 2.10. The active layer is exposed to possible contamination and scratches so must be handled carefully with cotton gloves. The film is also not symmetrical, hence attention must be payed on the orientation of the film during the irradiation.

To determine the delivered dose, the variation of film absorbance after being irradiated must be measured. The optical density of the film, $OD = \log_{10} \frac{I_0}{I}$ is defined to quantify this change, where I_0 is the initial transmitted intensity and I is the intensity transmitted after the film irradiation. In this work, the transmitted light through the film was studied using a scanner, therefore the film OD was defined as the color value of the acquired digital image.

The measurement performed using RCFs are relative, because no absolute dose value is given as an output. It is thus fundamental to define a calibration curve for the films under reference conditions, to establish their dose response. During the calibration the delivered dose and the number of films used for calibration must be chosen to fall inside the region of interest for the experimental measurements.

To prepare the films both for the experiment and for the calibration curve, a sheet of HD-V2 paper was cut in small squares of 30×30 mm^2 dimension. This was done in order to leave some extra film edge for film handling, having the beam an area at the measuring point of 20×20 mm^2. Each film was marked with a unique identification alphanumeric code for the post irradiation study as well as to recognize the orientation, using a permanent marker outside the beam area. Radiohromic films are light sensitive, therefore each film is wrapped into a protective aluminum foil when not used for irradiation or read-out.

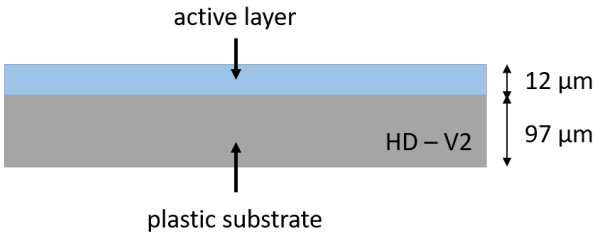

Figure 2.10: Representation of the structure of the HD-V2 radiochromic films.

2.4.2. Calibration curve

The first step consists in performing reference dosimetry with a broad beam, reproducing the same irradiation condition defined as reference using the PinPoint IC. The film is placed inside the water equivalent phantom at 2 cm in deep, with its center aligned at the center of the field. The film is attached on the surface of one of the squared slabs with some tape. Knowing the dose rate, beam height and the storage ring current at the moment of irradiation, once the desired dose D_x is chosen, the vertical speed of the stage is defined starting from the formula 2.11:

$$v = \frac{\dot{D} \times z_{beam} \times I}{D_x} \tag{2.13}$$

One film at a time is positioned inside the water phantom at the same position 2 cm in deep inside the cubic phantom. For this study, calibration films were irradiated starting from a dose of 50 Gy increasing by a step of 50 Gy each time, up to 400 Gy, with one extra point at 10 Gy, the minimum dose quantity nominally measurable with the HD-V2 RCFs. Two calibration curves were taken, one for the Conventional spectrum and one for the Preclinical and Clinical one, because the two spectra are close enough in energy to allow to use just one calibration curve for both. The films for the calibration curve are scanned, as explained more in detail in the next section, and by mean of a MatLab program in-house developed by Paolo Pellicioli [36], the digital image is analyzed obtaining as a result the grey value for each irradiated area. The program takes as an input the image and allows to select only the area of interest, i.e. the central region of the irradiated area, easily recognizable due to the change in the color of the active layer.
The calibration curve is obtained by giving as input for the fitting the dose sent to each film for calibration and the corresponding grey value obtained. The calibration points are fitted with following function, suggestion by Lewis et al. [68]:

$$D(x) = a + \frac{b}{x + c} \tag{2.14}$$

where x is the grey value from the image, D is the delivered dose and a, b and c are the fitting parameters. This suggested function describes the OD change of the film, with a R^2 higher than 0.99.

2.4.3. Radiochromic films irradiation

Depth dose profile measurement are conducted using the calibration curve to establish the dose delivered to films irradiated not in reference conditions.
To proceed with the experimental spectrum measurement, films are positioned inside the water phantom at the same depth used during depth dose profile measurements with the PinPoint IC (see section 2.3.4). Therefore, 10 films are inserted at different positions at the same time inside the water phantom and to get irradiated together.
Knowing the beam dose rate under reference conditions, the delivered dose at 2 cm in depth is chosen such that all expected doses on the different films fall inside the defined calibration curve. Three spectra were studied: the Conventional one, the Preclinical and the Clinical one. For statistic, three irradiation were performed for each of the three spectra.
As already done for the irradiated film for the calibration curve, the films are scanned after the irradiation to obtain a digital image. The three series of grey values for each different spectrum are averaged and then compared to the calibration curve to obtain the dose value at each depth. An image of the obtained calibration curve with the corresponding films used is shown in Figure 3.13.
The measured dose in reference conditions is divided by the actual dose delivered to obtain a scaling factor to reconstruct the expected dose curve. Multiplying the dose measured at each depth by the scaling factor the expected dose at each depth is obtained.

2.4.4. Film read-out

One of the limits of the film dosimetry is the impossibility to get a direct dose measurement: a reading instrument need to be used to obtain a relative value of the dose. For the purpose of this study an Epson Flat Panel Scanner model v750 was used: it is a professional scanner to turn photos and films into digital images. The sensor system is a linear CCD array: each array is realized with three lines of pixels with on-chip colors filters for red, green, and blue, that allow to scan colored pictures. Each pixel needs to fulfill the requirement of a large active area to achieve a large dynamic range, defined

as the ratio between the largest and the lowest value of the light intensity that can be detectable by the pixel. The spatial resolution of the scanner is expressed in DPI (dots per inch): it can go up to 6400 dpi covering an area until 14.8 width, with 113280 pixels across the area.
On the panel of the scanner a setup was mounted for the scanning of the film: it is a metal frame with an internal squared hole that is larger than 20×20 mm^2, but smaller than the whole film, in order to center the irradiated film on the scanner and to keep the film flat during the digitalization. Images of the films were taken twice: pre and post irradiation. The pre scanning is used obtain the zero of the calibration curve as a grey value, but can be also useful to have in case some defects were to appear in the post irradiation scan to check whether they were already there or not. Before the scanning of the film procedure the devices has always been warmed up by doing some empty scanning.

2.5. Monte Carlo simulations

Monte Carlo simulations (MC) have been used to obtain expected value for the depth dose profile measurements. Two sets of simulated data, based on different dose calculation algorithms, were calculated to reinforce the dosimetry validation of the study.
The Monte Carlo method is the solution of a macroscopic system simulating its microscopic interactions. MC simulations are a class of computational algorithms that rely on the repetition of a stochastic process to obtain an estimate of the expected value of the considered quantity by averaging the results over all the history observed. They provide numerical solutions to problems that can be described as a temporal evolution of "objects" (particles in the physics case). The estimate gets more precise as the number of histories increase: the error between the real value and the estimated value can be written as [69]:

$$s(N) = \sqrt{\frac{\langle x^2 \rangle - \langle x \rangle^2}{N}} \tag{2.15}$$

where N is the number of repetitions and x is the quantity under study. This is the estimated variance of the process that converges towards zero as the expectation values $\langle x^2 \rangle$ and $\langle x \rangle^2$ are converging towards a constant hence, the precision of a MC simulation is increased by increasing the number of histories.
When studying the microscopic interactions in a system each of them is represented by the probability to happen. In RT dose calculation, MC is used to simulate the path of ionizing particles inside the matter. The probability of interaction inside with the matter

are calculated based on theoretical models: they define the random path for each of the particle. To obtain statistically independent results making every trajectory unique, pseudo-random number generators are used with a repetition period that is larger than the number of random numbers used for the simulation. Pseudo-random and not random because their series is reproducible: that is useful for detailed investigation of rare events and for code debugging.
MC simulations allow to obtain highly accurate results when the interactions between the particles and the material in the case in question are very well known as a function of the material composition, mass density, particle energy and can be well modeled. Not only the primary particles are simulated, but all of the secondary particles generated by these primary one by the interaction with the material during the simulation. In our study the interaction of the photons with the matter for the generation of secondary electrons due to different physics phenomenon is simulated, as well as the cascade generation of other particles by these secondary electrons and so on. The simulation proceeds until either all the particles have lost their kinetic energy that has been absorbed by the material or the particles have exited the region of interest for the study.
The calculation of the radiation path inside the material need the path to be discretized. Not all the projects are in fact already discrete: the propagation of a particle inside a magnetic field is a continuous process that is divided into segments of arbitrary size, called steps. The size of the steps has a major impact on the quality and time-efficiency of the simulation: if the step size is short the distance travelled by a particle before its momentum and direction are recalculated gives a more precise result, closer to the real trajectory of the particle. Reducing the step size, the total number of steps increases and hence the total time to perform the simulation, because at each step some calculating time is needed. Depending on the particle type and energy, as well as on the interacting medium and on the spatial scale of interest, the adequate step size must be chosen.
For charged particles is very impractical to calculate the individual interactions when moving inside the matter because they are in the order of millions and would slow down the calculation. That's why condensed history calculations were introduced, it summarizes in one step a huge amount of quasi-elastic collisions, speeding up the simulation of orders of magnitude. A condensed history step has a net deflection angle and a continuous energy loss of a particle along its way in between two interaction points. The exact path of the particle cannot be reconstructed, so it's advisable to use this approach only when the scale of interest is larger than the order of magnitude of the step size [5, 69].

2.5.1. Conventional Monte Carlo algorithm

The code used to perform the simulation was in house developed by Mattia Donzelli using the Geant4 toolkit and it was modified in some of its parts for the study. Geant4 (acronym for Geometry and Tracking) is a toolkit implemented in C++ that provides an ensemble of classes which constitute the basic functions of a MC simulations [70]: the user can extend the applications according to its specific requirements. It was originally developed for calculations in the field of high energy physics and it's the result of a huge international collaboration. It covers a huge range of physical processes (electromagnetic, hadronic and optical processes) as well as a large set of particles, materials and elements over a wide range of energy. Geant4 exclusively uses the condensed history approach for charged particles making the calculation time-efficient. For the development of the Monte Carlo simulation, the Geant4 10.03.p03 version was used, selecting the PENELOPE physics model [71].

The code allows to reproduce the water cube phantom used for the experiment with a volume of 180 $\times$ 180 $\times$ 180 mm^3. Inside the phantom volume, a second volume was defined for the precise dose calculation. It was chosen a rectangular volume of 180 $\times$ 30 $\times$ 30 mm^3 respectively in x, y and z where x is the direction of the beam. The dimension of the field in fact is 20 $\times$ 20 mm^2 in y and z respectively, hence it is completely contained inside the chosen scoring volume. It was chosen a resolution of 500 µm for all the directions inside the scoring volume. The resulting dose was calculated by averaging over a volume equivalent to the PinPoint IC active volume.

The simulation was performed for each of the 6 spectra used to measure the depth dose profile. The final spectrum for each of the different configurations obtained from the Python code, explained in section 2.2.2, was given as an input in terms of photon flux [ph/s] per energy step [keV]. For each of the spectra 20 simulations of 10^9 photons each were performed and averaged to obtain a better statistics. Using an in-house developed Python code, the 20 simulations were then summed and it is possible to display the result as a color map with the error in each of the slice as well. The simulation error in fact, decreases by increasing the number of photons used in the simulation, and it increases going in deep inside the phantom because less photons reach the final part of the volume. The main limit of the classic Monte Carlo algorithm is that it is time consuming for complicated system to simulate, being very accurate.

2.5.2. Dose kernel convolution algorithm

The development of a new algorithm called dose kernel convolution algorithm, that will be explained hereafter, allowed to obtain a faster simulation by orders of magnitude, at the price of losing accuracy in the transport of scattered photons inside inhomogeneous geometries. A better compromise between the two available algorithms is obtained with the concept of hybrid dose calculation: it allows to have a fast and at the same time accurate algorithm.

Given a photon interaction at a certain point (x_0, y_0, z_0) in a radiation field, a point kernel $K_{(x_0,y_0,z_0)}(x, y, z)$ describes the energy distribution by scattering particles around this point. Dose kernels are thus defined as the spatial distribution of the mean energy dE per mass element dm caused by a primary particle interaction at the origin. For the dose kernel algorithm, kernels are generated by a simulation obtaining score deposition matrices as a function of the distance from the primary interaction point. The basic idea of the approach is to split electron and photon absorption due to their different ranges.

Mackie et al. [72] presented a solution in which two different kernel types are used: truncated first scatter kernel (TFS) that account for all dose deposition generated by the first photon interaction not exceeding a specific radius around the first interaction point and and residual and multiple scatter kernels (RFMS) that account the dose deposition from primary interactions exceeding the chosen radius and all following photon scatters. The RFMS are more homogeneous and have a lower dose gradients, hence are recorded on a broader resolution. In a homogeneous phantom the relative fluence distribution is convoluted with the two dose kernels to obtain a relative dose distribution, that means kernels are superposed along the primary beam depending on the interaction probabilities. For inhomogeneous geometries the O' Connor's theorem [73] on dose kernel scaling is used. According to it, the kernel is invariant to the change of mass density of the absorbing media if the product of distance and mass density $l\rho$ is taken as a reference instead of just the distance l. Mackie et al. [72] to deal with inhomogeneities in the target, scaled the TFS kernel with the mean density between the kernel origin and the point of deposition, while for RFMS kernels, the mean density of the target geometry is used.

The assumptions on which these algorithms are based are valid only for high energy photons when the dominating scattering mechanism is Compton scattering: in fact, in this energy domain the attenuation coefficient has no dependence on the atomic composition. For photons with energy in the order of keV the photoelectric effect is significant, that has an important non-linear dependence on the atomic number. An analytical method to derive the dose kernels adapted to photons in keV energy range was developed by Bartzsch and Oelfke [74], but the kernels for photons propagation are not adapted to

inhomogeneities in the target.

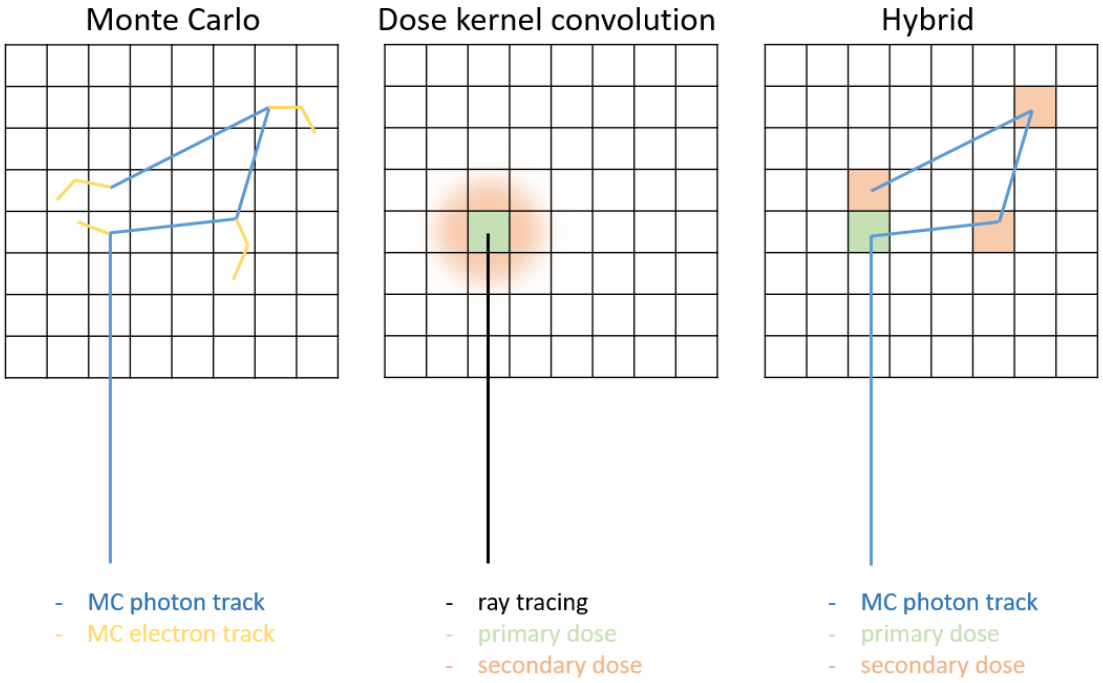

Figure 2.11: On the left is shown the method behind the conventional MC simulations: it consists in following the path of both the photons at first and the electrons when generated inside the material. In the middle is shown the idea of the dose kernel algorithm, the ray tracing technique to follow the photon path and the generation of a kernel where each photon impact. In the image on the right is shown instead the hybrid algorithm, that consists in a mix of these two first techniques: the photon are treated as in the conventional MC simulation, but for the electrons a kernel is generated whenever there is a scattering event. Credits to Mattia Donzelli [5].

2.5.3. Hybrid Monte Carlo algorithm

The hybrid calculation [5, 75] approach aims at combining the advantages of Monte Carlo techniques and dose kernel convolution based techniques in order to provide a faster algorithm which is free of systematic error due to the assumption of homogeneity for the transport of scattered photons. Still, classic MC remains the only correct option to reproduce the propagation of photons in an heterogeneous geometry.
The hybrid algorithms separates photon and electron energy transport. Photon transport is calculated with Monte Carlo simulation performed on a millimetric scale based on the voxel size, taking only photon interactions into account. The energy of the generated electrons is calculated using a dose kernel algorithm in a range that is typically smaller

than the size of a typical voxel, so within the voxel the material is assumed homogeneous [5, 76, 75].
The first stage consists in a Monte Carlo simulation for photon transport: it determines the average energy transfer of primary photons coming from the source to each voxel of the target geometry. The primary dose is constituted by all energy transferred in the first scattering event of a photon, that can happen by mean of Compton scattering or photoelectric scattering, while pair production is energetically impossible.
In the second stage of the hybrid algorithm the electron energy absorption is calculated for each voxel individually applying a few reasonable assumptions: homogeneous material composition and density within a single voxel, photon spectrum and beam intensity unchanged during the passage through the voxel. Convoluting the fluence distribution of primary photons with the electron dose kernel generates the relative dose distribution. It can be calculated as:

$$D(r) = D_{Scatter}(r) + D_{Primary}(r) \cdot ({K_{el}}^{3D} * \nu(r)) \tag{2.16}$$

Where ${K_{el}}^{3D}$ is the electron kernel, as the dose kernel of scattering electrons created in a primary photon interaction convoluted with the $\nu(r)$ that describes an energy transfer event (either Compton or photoelectric scattering). $D_{Scatter}$ and $D_{Primary}$ are the Monte Carlo primary and scatter dose contributions. A scheme on the different types of algorithms for MC is shwon in Figure 2.11.
For the current work, Varian Eclipse^{TM} software was used as a graphical tool to define the simulation geometry and the irradiation parameters as it occurs in Treatment Planning Systems (TPS), while dose calculation with hybrid algorithm was performed to a Linux workstation paired to the Varian machine [77, 78]. TPS are at the heart of RT: they are software on which the user can upload images and datasets to identify the tumor and the system will develop the best plan to treat the patient, providing the expected dose distribution in patient's tissue, the level of penetration influenced by the type of tumor. Using the hybrid algorithm for MC simulation on the TPS Eclipse^{TM}, accurate results for the irradiation with microbeams can be obtained.
The platform allows you to choose the setup: as done for the conventional MC the 180 $\times$ 180 $\times$ 180 mm^3 equivalent to water cubic phantom was simulated. The voxel sizes was chosen to be 1 mm.
Hybrid simulation from the *Eclipse*^{TM} was performed for the Conventional spectrum, the Preclinical spectrum and the Clinical spectrum in order to compare the results with that obtained from the conventional MC simulations. In Figure 2.12 it's shown the interface of the TPS.

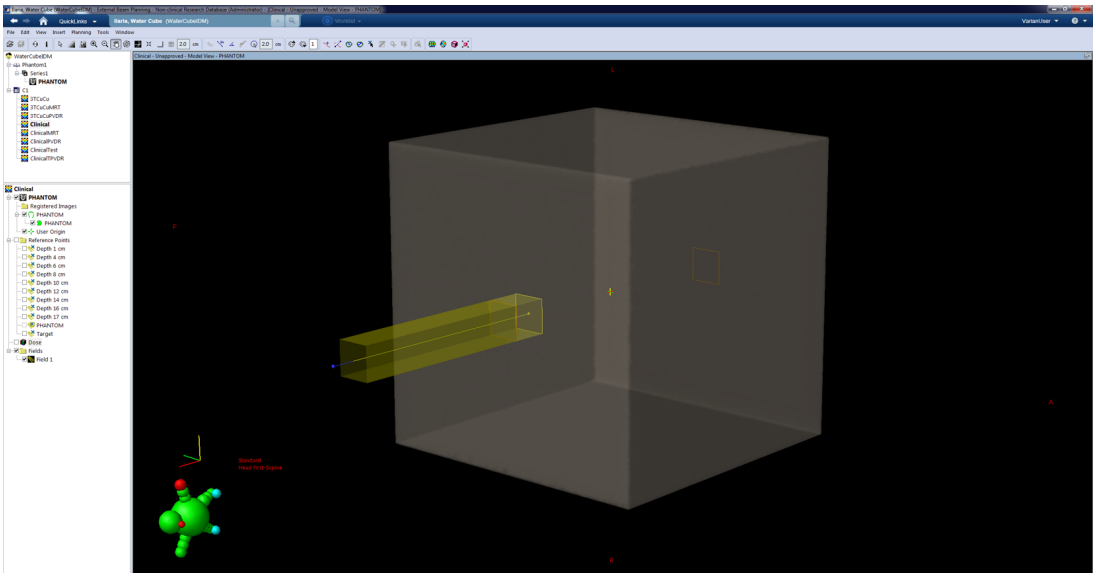

Figure 2.12: In the image is shown a screenshot of the *Eclipse*^{TM} TPS with the setup used for the simulation.

2.6. Uncertainty budget

2.6.1. Uncertainty for HVL calculation

The attenuation coefficient used in the XrayDb library are taken from the NIST database [79, 80], that provides an uncertainty for the data that is 1% far from the k-edge and other principal absorbing edges of the materials and an uncertainty around 2% for energies that are above 200 keV [81]. The spectra used are cut well above the absorbing edges of the material used as attenuators and have only few photons at energies above 200 keV. To remain conservative, an uncertainty of 2% on the mass absorption coefficient was assigned, following the same approach used by Crosbie et al. [49].

2.6.2. Uncertainty for HVL measurements

For the HVL measurement the uncertainties are related mainly to three factors: the dosimetry performed with the PinPoint, that will be analyzed in the following section, the uncertainty due to the measurement of the thickness of the metal sheets and the uncertainty on the beamline components.
The digital caliber precision is ±0.005 mm. The % uncertainty on a single piece depends on the measured value, taking the average measured value one that is around 1 mm we get an uncertainty of 0.5%. For the measurement of the HVL many sheets were put together, hence to calculate the total uncertainty the contribution from each of the sheets can be

summed in quadrature. The largest number of components put together was 37 pieces for Al calculation and 12 pieces for Cu HVL, thus the largest uncertainty due to the caliber would be:

$$\frac{\sigma_t}{t} = \sqrt{37(0.5)^2} = 3.04\% \tag{2.17}$$

Assuming a similar uncertainty for the thickness of all the components of the beamline, hence five attenuators and thickness of the components of monitoring devices, other 10 pieces giving an uncertainty of 0.5 % can be taken into account. This brings the largest uncertainty due to thickness measurements to:

$$\frac{\sigma_t}{t} = \sqrt{47(0.5)^2} = 3.42\% \tag{2.18}$$

This value is quite exaggerated because such an high number of components inside the beam was present only for very few measurements. On average around 20 attenuating layers were inserted in the beam. This would lead the uncertainty to:

$$\frac{\sigma_t}{t} = \sqrt{20(0.5)^2} = 2.24\% \tag{2.19}$$

This second value will be considered for the total uncertainty.
For all the components also an uncertainty on the position, i.e. the precision on the degree of inclination, should be added. Using the same value from the work of Crosbie, that is around 0.8 %.
Another component that could introduce an error is the vertical slit of 0.520 µm. Its size was measured with a Silicon Strip Detector with ±1 µm precision, obtaining an uncertainty of 0.19 %.
Summing up in quadrature all the uncertainty values cited it is obtained a total of 2.38% at 1σ. Expanding the value at 2σ for coherence to what done in the next section the total value obtained is of 4.76 %.

2.6.3. Uncertainty for absolute dosimetry

Factors considered for the evaluation of the uncertainty on the irradiation were the variation of the vertical speed of the stage compared to the nominal selected speed and the variation of the current in the storage ring, as well as the uncertainty in the measurement with the PinPoint IC.

From the measurement performed by the the ESRF - ISDD. Mechanical Engineering Group, Advanced analysis and precision unit the measured speed has a variation smaller than 0.06% at 2σ compared to the value defined from the user interface. For the storage ring current, the value is given with a 0.05%, 2σ precision.
The uncertainty in dosimetry measurement is due to the uncertainty on the correction factors for the PinPoint that was explained in section 2.3.1. To determine the relative uncertainty of the reference dosimetry we follow what determined by Fournier et al. [61]. The relative uncertainty was determined by summing in quadrature all the uncertainties related to the correction factors applied to the PinPoint chamber reading.
On the PTW calibration certificate for the PinPoint 31014 the uncertainty on the k_Q calibration factor for the TH 200 beam quality is given equal to 3.7%. The uncertainty on the calibration of the electrometer k_{elec} is given equal to 0.5%. The correction factor for the polarization effect k_{pol} is reported to be $\leq$ than 1.0%, so in order to remain conservative it was chosen to use $\pm$ 1%. All values from PTW are given at 2σ so the same level was maintained also for the following uncertainties. The thermocouples have an accuracy of $\pm$ 0.1 degree, that divided by the environment T in K, gave a negligible error. Assuming that, due to the positioning of the thermocouples, the error on the measured T could go up to $\pm$ 0.5 degree, the error becomes around 3% at 2σ. The barometer has a precision of 0.05 hPa that over the environment P gives a much smaller error. The total uncertainty on $k_{T,P}$ depends on both factors, hence it can estimated to be around 0.3%.
Values for k_s were experimentally evaluated in 2020 by P. Pellicioli and M. Krisch at the ESRF (unpublished). Following the protocol chosen in 2014 by Fournier et al. [61] the ramping method was used: k_s factor was determined by ramping up the storage ring current while keeping the beamline setup fixed. The measured dose rate in $\frac{Gy}{s}$ is divided by the synchrotron current: recording the dose rate in $\frac{Gy}{smA}$ as a function of the ring current it is obtained, as expected, a decrease of the dose rate when increasing the storage ring current (Figure 2.13a).
It was chosen to express the recombination factor as a function of the dose rate as can be seen in Figure 2.13b were it can be seen that by increasing the dose rate the k_s increases as well.

For the error on k_s, having obtained different results from that proposed by Fournier [61], it was decided to use the standard deviation of the measurement. Every experimental point was measured five times for statistic, and the final error at 2σ is around 0.08%.
Finally also an error in the PinPoint IC alignment in the beam axis was introduced. This error has to be introduced only for the depth dose profile that has to be performed in reference conditions, i.e. 2 cm in deep inside water. For the HVL measurement that is

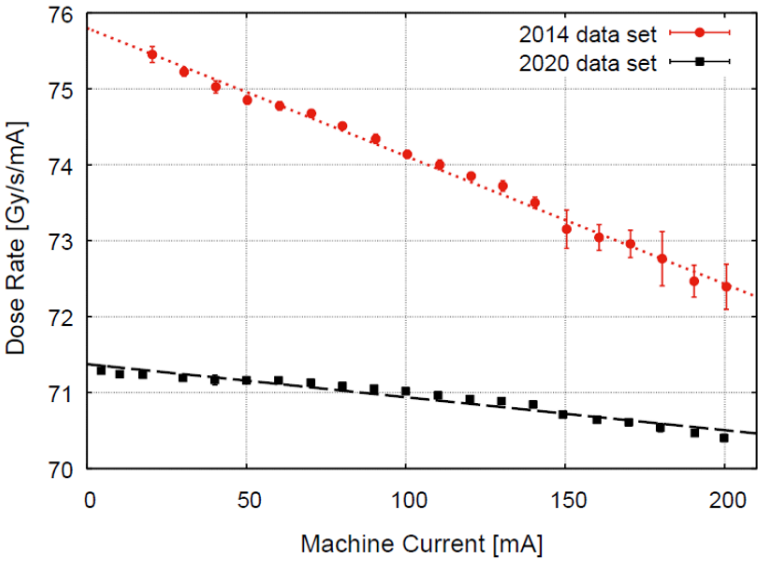

(a)

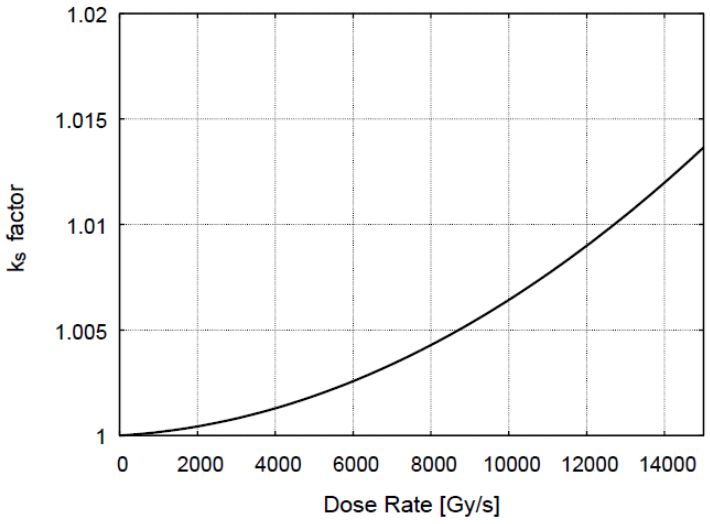

(b)

Figure 2.13: (a) The image shows the dose rate as a function of the machine current resulting from the ramping experiment. Two curves are present: the red one shows the result obtained by Fournier et. al [61] in 2014, while the black one shows the results for the same experiment obtained by P. Pellicioli and M. Krisch in 2020. (b) In the graph is shown the k_s correction factor as a function of the dose rate resulting from the ramping experiment carried out in 2020.

performed in air there is no misalignment on the position, while for the reference dosimetry the positioning error introduce a change in the dose reading of ±1.6%.
Summing up all the contributions in quadrature, the uncertainty for the dosimetry in air was:

$$\begin{aligned}\frac{\sigma_D}{D} &= \sqrt{\frac{\sigma_{k_Q}}{k_Q}^2 + \frac{\sigma_{k_{pol}}}{k_{pol}}^2 + \frac{\sigma_{k_{elec}}}{k_{elec}}^2 + \frac{\sigma_{k_{T,P}}}{k_{T,P}}^2 + \frac{\sigma_{k_s}}{k_s}^2} \\ &= \sqrt{(3.7)^2 + (1)^2 + (0.5)^2 + (0.3)^2 + (0.08)^2} \\ &= 3.88\%\end{aligned} \tag{2.20}$$

For the PinPoint used in reference inside the water-equivalent phantom, the total uncertainty was:

$$\begin{aligned}\frac{\sigma_D}{D} &= \sqrt{\frac{\sigma_{k_Q}}{k_Q}^2 + \frac{\sigma_{k_{pol}}}{k_{pol}}^2 + \frac{\sigma_{k_{elec}}}{k_{elec}}^2 + \frac{\sigma_{k_{T,P}}}{k_{T,P}}^2 + \frac{\sigma_{k_s}}{k_s}^2 + \frac{\sigma_{position}}{D}^2} \\ &= \sqrt{(3.7)^2 + (1)^2 + (0.5)^2 + (0.3)^2 + (0.08)^2 + (1.6)^2} \\ &= 4.16\%\end{aligned} \tag{2.21}$$

Summing up in quadrature with the uncertainty on the beamline components described in section 2.6.1 we get a total uncertainty around 6.14% at 2σ for the dosimetry in air and an uncertainty of 6.32% at 2σ for dosimetry in reference conditions.

2.6.4. Uncertainty for radiochromic films dosimetry

For the film homogeneities, the provider guarantees an uniformity in the response of the film better than 3%. The pre-scanning make it possible to establish the regions where the film has lower variations, in order to limit the non-homogeneities due to the production process: this improve the uniformity with a variation of 1% [82].
Starting from the standard deviation obtained from scanning the irradiated films in the same conditions, a maximum uncertainty of 2.3% at 1σ is obtained. Summing up in quadrature the two types of uncertainties a total value of 2.51 % at 1σ is obtained. To be conservative, being the uncertainty due to the scanning process not well known, it was decided to use the uncertainty at 2σ obtaining a total value of 5.02 %. This value will be used for the analysis of the data in chapter 3.

2.6.5. Uncertainty for Monte Carlo simulations

The conventional Monte Carlo simulation give as an output the error for the dose calculation for each of the slices in which the system was divided. The error increases going in deep into the phantom because less particles are reaching the last slices, being the photons partially absorbed during their propagation. As shown in the equation 2.15 the standard deviation decreases by increasing the number of history N: the final result is the average of 20 simulations with 1 billion photons each, hence the final error is diminished with respect to the single simulation.
From the output, the error on the first slices was in the 0.074% - 0.076% range for all the spectra, while in the last slices goes up to 0.28% - 0.33% for all the spectra at 1σ, hence at 2σ the error can be up to 0.152% on the first slice and 0.66% on the last slice.
For the hybrid MC simulations the uncertainty is given in the output file as the average uncertainty of a voxel for both the primary and secondary dose, i.e. the photons and electrons dose respectively. The values are reaching a maximum of 0.25% for the primary dose and 0.47% for the secondary dose, hence summing up in quadrature an uncertainty of 0.53% at 1σ is obtained. To be coherent with the rest of the study the 2σ uncertainty is used, for a total value of 1.06%.

Uncertainty parameter	Standard uncertainty [%]
Spectra Simulations	
Mass absorption coefficient	2
HVL measurement	
Average caliper uncertainty (counting additional sheets and attenuators)	2.24
Degree of inclination	0.8
Vertical slit size	0.19
Total uncertainty (2σ)	4.76
Dosimetry	
k_{elec}	0.5
k_{pol}	1
k_Q	3.7
$k_{T,P}$	0.3
k_s	0.08
$k_{position}$	1.6
Total uncertainty air dosimetry (2σ)	3.88
Total uncertainty reference dosimetry (2σ)	4.16
Film read-out	
Film non-homogeneity at micrometric scale	1
Non-homogeneity over different films	2.3
Combined standard uncertainty (2σ)	5.02
Monte Carlo simulations	
Conventional MC	0.66
Hybrid MC	1.06

Table 2.3: Uncertainty budget.

3 | Results

3.1. Spectra calculation

3.1.1. Raw spectrum

The resulting raw spectrum from the wiggler with a gap of 24.8 mm and the spectrum average after the passage through the vertical slit (VS) of 20 mm × 0.52 mm as obtained from OASYS are both shown on the same plot in Figure 3.1. The spectra are expressed in terms of the brilliance [ph/s/0.1%BW] normalized by the current used for simulation (200 mA) and the area of the vertical slit, thus [ph/s/0.1%BW/mm^2/mA], in logarithmic scale, as function of the photon energy [keV]. The same units will be used to present all the spectra in the following sections.

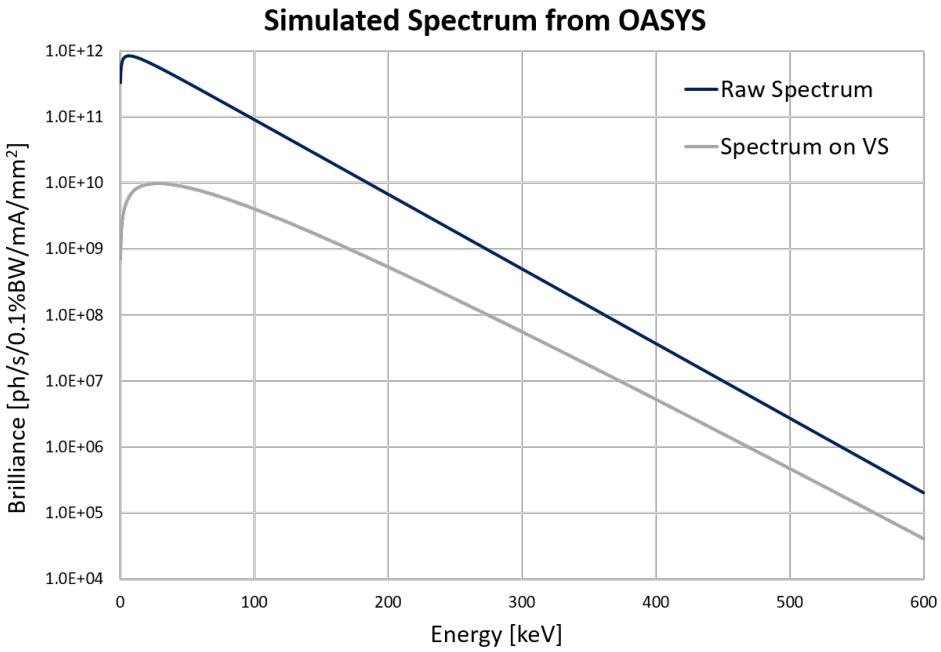

Figure 3.1: In blue is shown the raw spectrum from the ID17 wiggler when the gap is 24.8 mm, while in grey is shown the same spectrum after the passage through the vertical slit of size 20 × 0.52 mm. Both results are obtained from the OASYS software.

3.1.2. Final spectra

Once the raw spectrum from OASYS was obtained, it was given as an input to the Python code in-house developed to simulate the presence of the attenuators and monitoring devices in the beam path. In this section the spectra resulting from different configurations, as generated by the Python simulation explained in section 2.2.2, are presented. For the name of the spectra and the respective components the beam crosses, refer to table 2.2 in section 2.1.2.
In the first Figure 3.2 is shown the comparison between the three most important spectra: the conventional one, the preclinical one and the clinical one. The conventional spectrum and the preclinical one differs just for a thickness of a Cu filters, while the clinical one has the same configuration of filters of the preclinical spectrum, but as well the two ionization chambers used as monitoring devices are inserted.

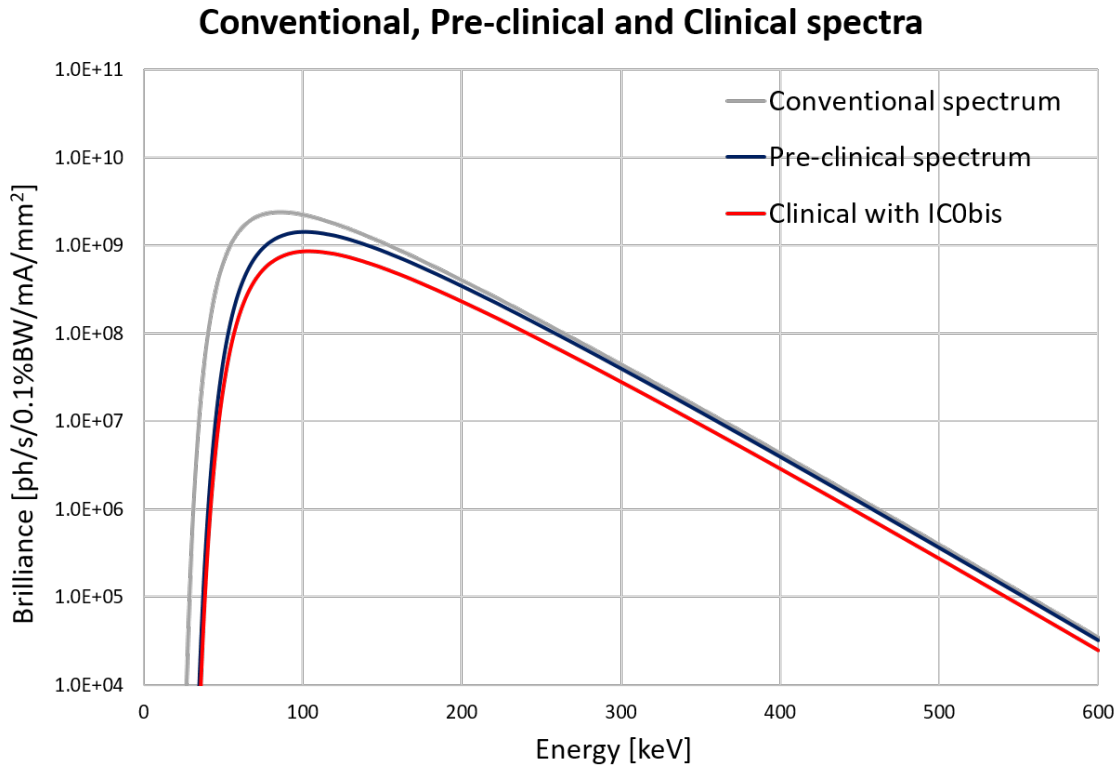

Figure 3.2: In grey is shown the conventional spectrum, the pre-clinical spectrum is in blue and the clinical spectrum with ICO and IC0bis in red. These spectra have all been obtained simulating the presence of the attenuators with the Python code, starting from the raw spectrum on the VS obtained from the OASYS software.

As it can be seen from the plot, the presence of the attenuators cut the low energy photons

changing the mean and the peak energy of the spectra, with respect to the non attenuated one. In Table (3.1) the mean energy in keV and the peak energy in keV values are given for all the studied spectra. The mean energy of the spectrum is calculated summing up all the brilliances for each energy point, multiplying by 1000 and dividing by the sum of all the photon flux [ph/s/mA/mm^2] per each energy point:

$$E_{mean} = \frac{\sum_{E_{min}}^{E_{max}} Brilliance(E)}{\sum_{E_{min}}^{E_{max}} Photon\ Flux} 10^3 \tag{3.1}$$

Starting from the definition of the brilliance given, in equation 2.2 at the end of section 2.1.1, the photon flux is obtained by eliminating the energy bandwidth dependence, thus dividing the brilliance value by the corresponding energy point E and multiplying by 10^3. Summing up all the brilliances for each energy point and multiplying by 10^3 what is obtained is the number of photons per second weighted for the central energy value E; dividing by the total number of photons per unit time the mean energy is obtained.
The peak energy, instead, is the energy for which the brilliance reaches its maximum value.
In the Table 3.1, on the third column, the dose rate as measured by the PinPoint during dosimetry in air conditions (section 2.3.2) is reported, being an important value to characterize the spectra in RT.

	Mean Energy [keV]	Peak Energy [keV]	Dose rate [Gy/s]
Maximum Intensity Spectrum	101.4	84.2	16162.4
Conventional Spectrum	101.8	85.8	15699.2
Pre-Clinical Spectrum	117.3	101.4	9807.8
Pre-Clinical + IC0 Spectrum	118.2	102.2	9005.4
Pre-Clinical + PMMA Spectrum	119.2	102.2	6578.8
Pre-Clinical + IC0bis Spectrum	119.2	102.2	6582.0
Clinical with PMMA Spectrum	120.0	102.2	6048.7
Clinical with IC0bis Spectrum	120.0	102.2	6045.2

Table 3.1: Mean energy [keV], peak energy [keV] and measured dose rate [Gy/s] for the eight different spectra.

In Figure 3.3 the clinical spectra with either IC0bis or PMMA are plotted to see whether some big differences in the attenuation provoked by the two elements can be seen. As it can be observed from the top plot, the two spectra are very similar, the one with IC0bis resulting just a little less attenuated. To quantify the difference between the two spectra,

on the bottom plot the % difference between the two is shown. As it can be seen, it goes up to a maximum of around 1% for significant energy values: where the most of the photons are cut by the attenuators the % difference is increasing because the brilliance has a value close to zero.
The difference between the two spectra can be explained by the fact that to obtain the exact clinical spectrum with IC0bis, the composition of the varnish layer inside the Bragg Peak chambers should be known, as explained in section 2.2.2. The similarity between the two spectra should allow to say that using 22 mm of PMMA at place of the IC0bis is a good approximation, but to be even more precise, the same comparison has been carried out using the HVL obtained for the two spectra, as it will be shown in the next section 3.2.

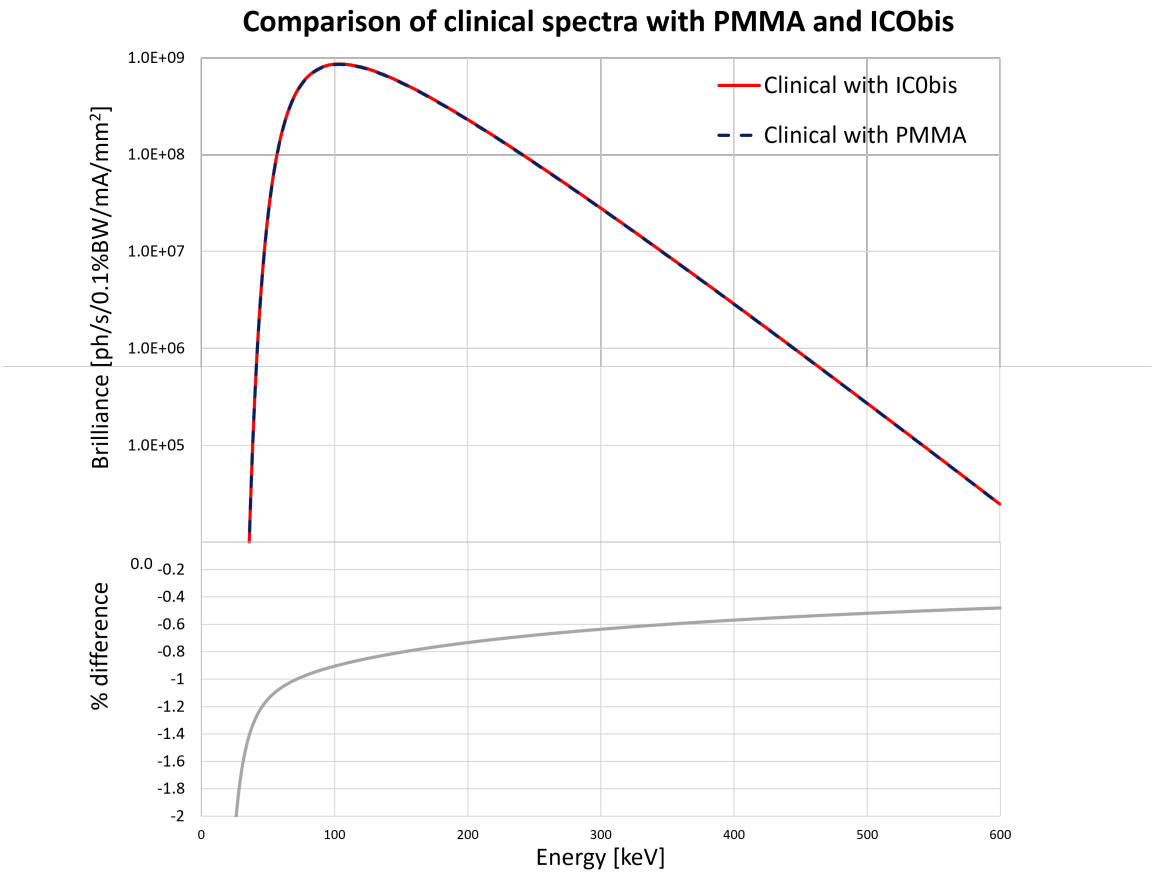

Figure 3.3: On the top plot the clinical spectrum with either IC0bis(in red) or PMMA (in blue) are shown: the two spectra can be considered almost equivalent, as it can also be observed from the bottom plot, where the % difference between the two spectra can be seen.

3.2. Half Value Layers measurements

In this section, the results of Half Value Layer measurement compared to that obtained from the HVLs simulation are presented.
In the following Figures 3.4, 3.5 and 3.6, the top plot shows the comparison between the measured intensity ratio (IR_{meas}) and the simulated intensity ratio (IR_{sim}) as a function of the thickness of the extra sheets of Al and Cu. The bottom plot instead, shows the percentage difference between the measured and the simulated data, always as function of the thickness of the extra layer material. The percentage difference is evaluated as following:

$$\%\, difference = \frac{(IR_{meas} - IR_{sim})}{IR_{sim}}\,\% \tag{3.2}$$

The trendline connecting each point showing the % difference between the two set of data has been added just to help the reader in the visualization.
The results are shown for the three main spectra: the conventional one, the pre-clinical one and the clinical one with IC0bis, those that have been used for all the different methods of characterization. The plots and data for the other spectra can be found in the appendix B. The resulting % difference is below 2% for all the measurement performed using Al extra sheets and below 3% for all those in which Cu extra layers were used, with a large part of the values that stays even below 1%. These values mean that the simulated spectra are well representing the real situation.

The plotted IR are considering all the correcting factors for the PinPoint IC measurements explained in section 2.3.1, improving the agreement between the two dataset.
As regards the $k_{T,P}$ correcting factor, the formula 2.10, using as T the one measured with the thermocouples close to the PinPoint and as P the one measured inside the chamber, has been followed. The factor was used to correct the initial value of $k_{T,P}$ inserted in the electrometer obtained measuring both the variables at the beginning of the experiment, that was already take into account during measurements.
For the k_Q correcting factor for the mean energy of the beam, the number of photons corresponding to each of the energy of the calibration curve from PTW has been weighted for its respective calibration factor. In the following table the calibration values from PTW for the PinPoint IC with the corresponding mean energies are shown:

For each of the inserted extra layer material in the beam, the resulting spectra has been calculated. The number of photons per second at each of the energy of the calibration curve has been multiplied by the respective correcting factors and the resulting numbers

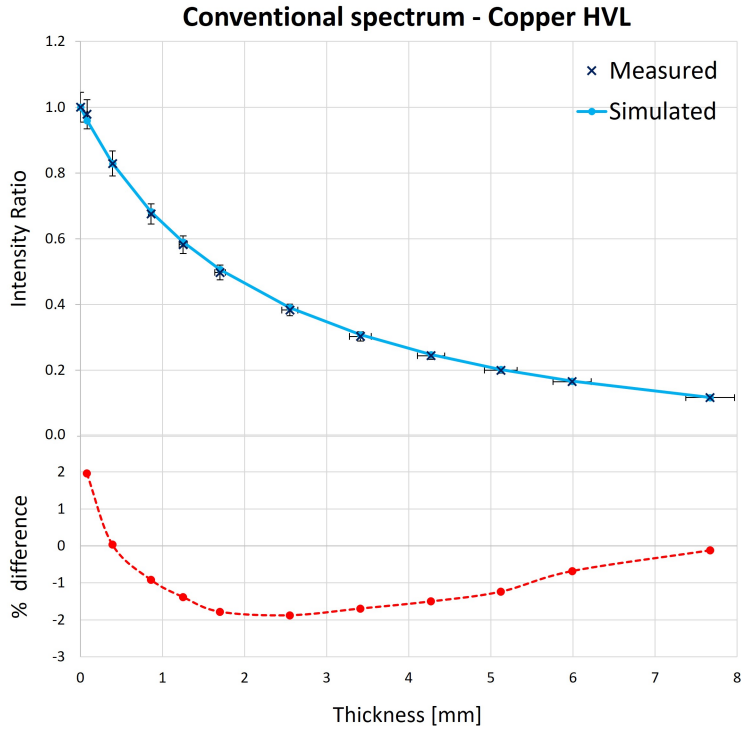

(a)

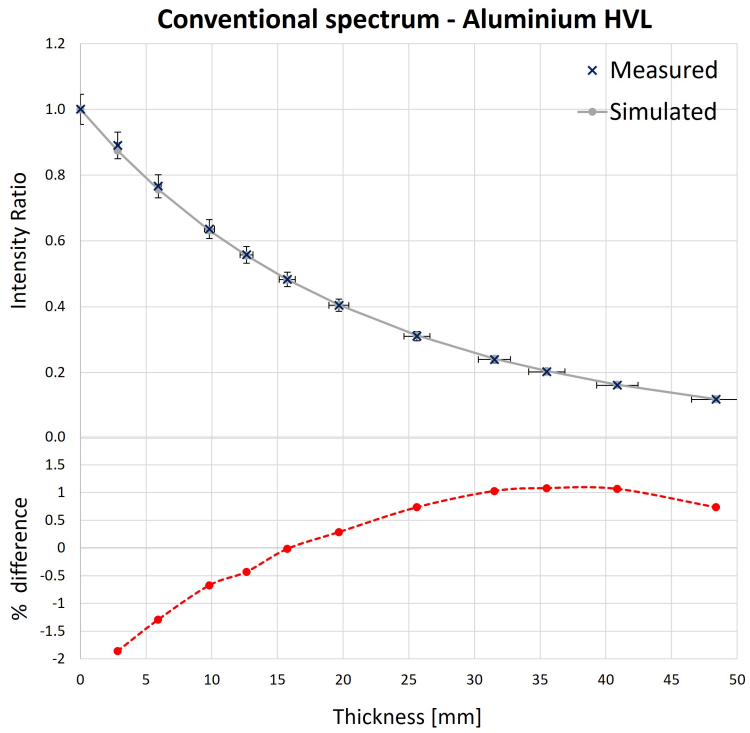

(b)

Figure 3.4: (a). Plot of measured data (blue) against the simulated data (light blue) for HVL, using extra Cu sheets, conventional spectrum. (b). Plot of measured data(blue) against the simulated data (grey) for HVL, using extra Al sheets, conventional spectrum.

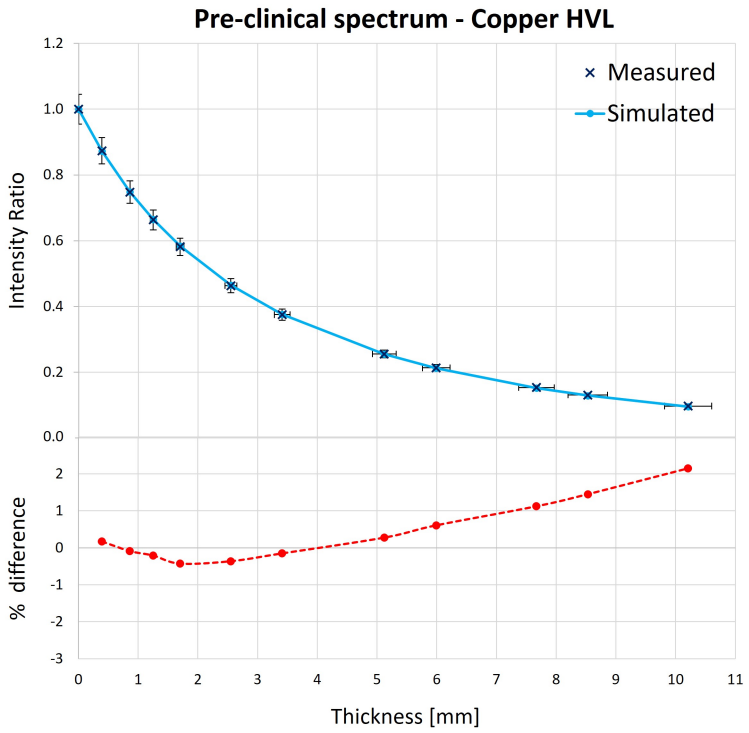

(a)

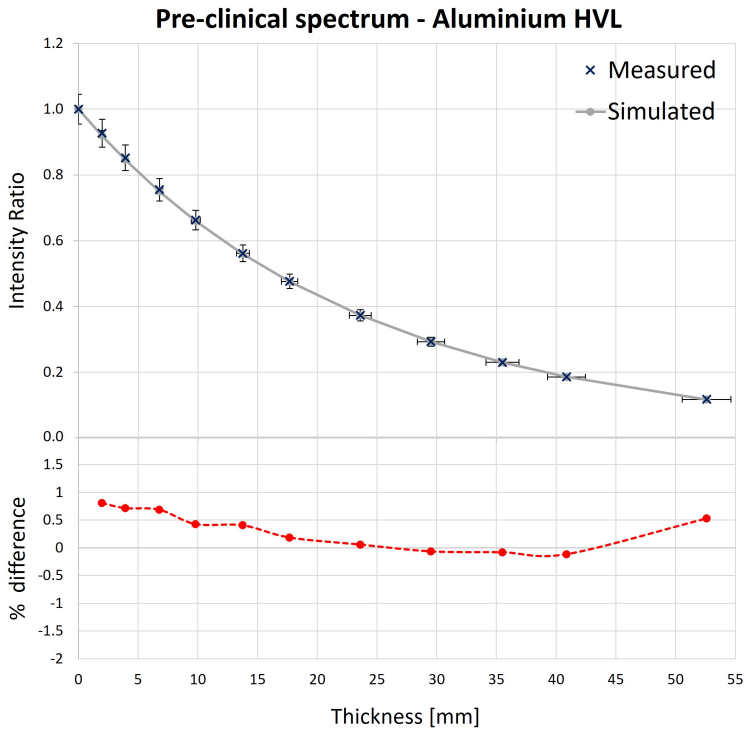

(b)

Figure 3.5: (a). Plot of measured data(blue) against the simulated data(light blue) for HVL, using extra Cu sheets, pre-clinical spectrum. (b). Plot of measured data(blue) against the simulated data (grey) for HVL, using extra Al sheets, pre-clinical spectrum.

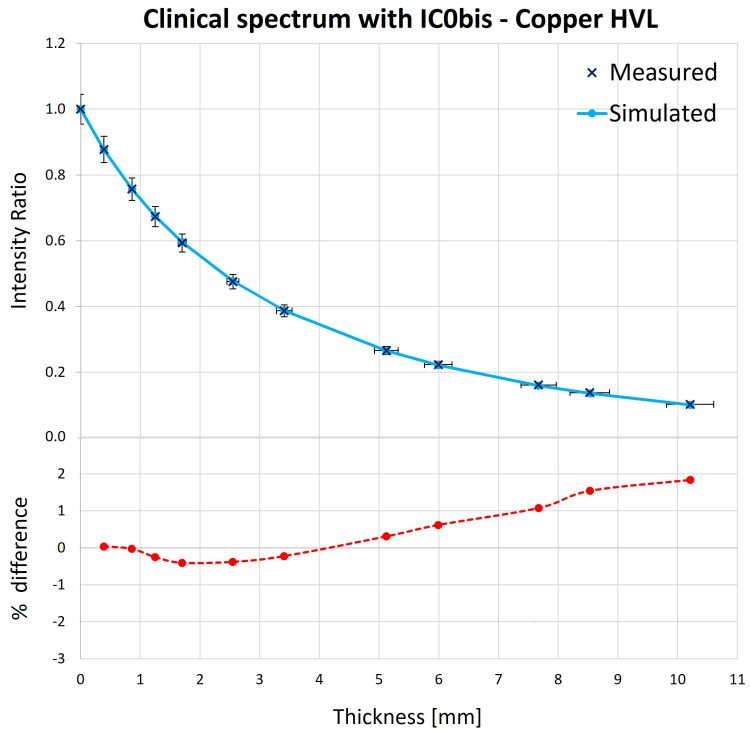

(a)

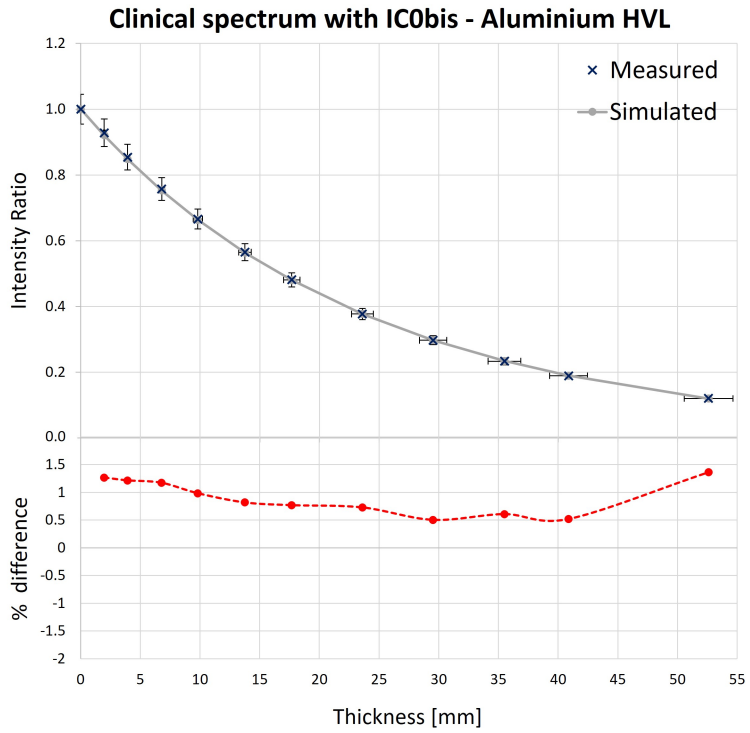

(b)

Figure 3.6: (a). Plot of measured data (blue) against the simulated data (light blue) for HVL, using extra Cu sheets, clinical spectrum. (b). Plot of measured data (blue) against the simulated data (grey) for HVL, using extra Al sheets, clinical spectrum.

Beam Quality	Mean Energy [keV]	Correcting Factor k_Q
TH280	163.0	0.951
TH200	109.0	0.948
TH140	65.7	0.966
TH100	46.4	0.983

Table 3.2: Correcting factors as a function of the mean energy of the beam for the different beam qualities as provided by PTW in the calibration document for the TW31014 PinPoint IC, serial number 000981, calibration 09/2020.

were summed up and divided by the sum of the number of photons at each energy point, following the procedure presented by Butler et al. [83]:

$$k_Q = \frac{n_{ph@163.0keV}0.951 \ + \ n_{ph@109.0keV}0.948 \ + \ n_{ph@65.7keV}0.966 \ + \ n_{ph@46.4keV}0.983}{n_{ph@163.0keV} \ + \ n_{ph@109.0keV} \ + \ n_{ph@65.7keV} \ + \ n_{ph@65.7keV}} \tag{3.3}$$

The obtained correcting factors was used to correct the calibration factor already used, the one for TH280 beam quality.
The last correcting factor inserted is the k_s, polarization correcting factor: from the unpublished analysis performed by Paolo Pellicioli and Michael Krisch, it can be obtained as a function of the dose rate [Gy/s], measured following this equation:

$$k_s = \dot{D}^2 \, 5.34 \cdot 10^{-11} \ + \ \dot{D} \, 1.09 \cdot 10^{-7} \tag{3.4}$$

The error bars present on the plots are represented following the uncertainties calculated in sections 2.6.1 and 2.6.2. The vertical error bars represent the uncertainty on the dose measurement obtained with the PinPoint ionization chamber and the uncertainty on the thickness of the components inside the beam: by summing in quadrature 3.88% for the dosimetry in air and an average value of 2.24% for the beamline components uncertainty, a total value around 4.55% was considered, as explained in section 2.6.3. The horizontal error bars are the uncertainty due to the thickness of the extra material inserted in the beam: it has been used 3.87% at 2σ as an average value.
For all the spectra, are shown here the expected HVLs from the simulation compared to the measured HVLs. It was not possible to measure the exact thickness predicted

from the simulation by using the extra layer that were at dispose, hence the measured HVL is obtained fitting the IR curve. As explained in section 2.2.1, being the beam polychromatic, the Lambert - Beer law is no longer exponential, hence the fit need to be done with another function. The function has been re-written as:

$$x = \frac{-\ln \frac{I}{I_0}}{\alpha} \tag{3.5}$$

where α is different for all the beam energies and x is the thickness to be found. It was decided to use as a fit a polynomial function of second order (3.6) to find the HVLs thicknesses. Being the function not an exponential, whatever function that was a good fit for the curve could have been chosen. The choice to use a polynomial function of second order has been already followed by Crosbie et al. [49], hence it was decided to see the results for the same fit.

$$x = a_0 + a_1 \ln IR + a_2 \ln IR^2 \tag{3.6}$$

It was imposed the passage by the origin, being the thickness of extra layer zero when the intensity is I_0, and therefore only the parameters a_1 and a_2 were the output of the fitting. The fitting for one of the curves is shown in Figure 3.7. All the fittings show an R^2 value that is either 0.99 or 1, meaning that the chosen function was suitable for the data.

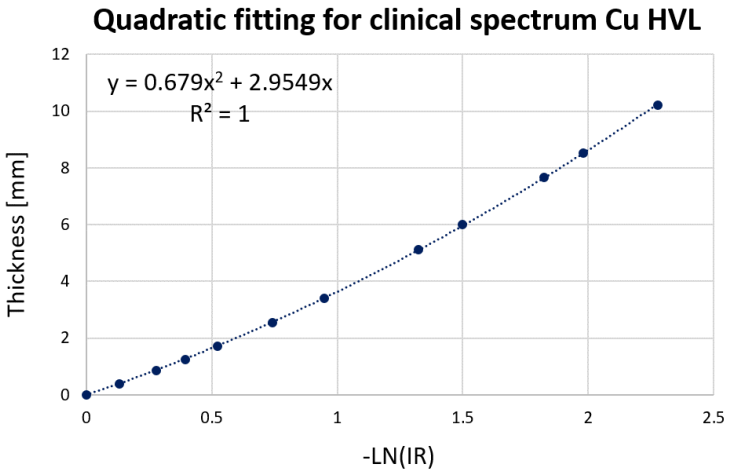

Figure 3.7: The quadratic fitting obtained for the Cu HVL using clinical spectrum is shown here with its equation and the R^2 parameter to see the quality of the fitting.

By imposing the IR to be 0.5 the HVL1 is found. Then, for HVL2 and HVL3 the IR was

imposed respectively 0.25 and 0.125.
The error on the measured value used in the following tables has been obtained considering the total uncertainty factor of 3.88% for dosimetry in air condition summed up in quadrature with the average uncertainty for the measured thickness of the extra sheets and of the beamline components of 4.76%, as described in sections 2.6.3 and 2.6.2, respectively, obtaining a total uncertainty of 6.14%. For the simulated value it was taken into account only the uncertainty due to the absorbers and monitoring devices attenuation coefficients used in the simulation of the spectrum, that has been accounted to be 2% (section 2.6.1).
The percentage difference between the measured HVL and the expected value from the simulation is shown as well, using the same method from equation 3.2.
The results are shown in tables 3.3, 3.4 and 3.5. As it can be seen the percentage difference obtained for the HVLs is in accordance to what obtained with the fitting curve. The % difference is below 2% for the Cu HVL, while it's always below 1% for the Al data.

Conventional	Experimental Cu [mm]	Theoretical [mm]	% diff
HVL1	1.71 ± 0.10	1.74 ± 0.04	-1.99
HVL2	4.16 ± 0.26	4.24 ± 0.09	-1.88
HVL3	7.36 ± 0.45	7.36 ± 0.15	0.06

(a)

Conventional	Experimental Al [mm]	Theoretical [mm]	% diff
HVL1	14.99 ± 0.92	14.97 ± 0.30	0.11
HVL2	30.64 ± 1.88	30.76 ± 0.62	-0.41
HVL3	46.94 ± 2.88	47.24 ± 0.95	-0.63

(b)

Table 3.3: (a). Experimental measured HVLs of Cu compared to theoretical predictions for conventional spectrum. (b). Experimental measured HVLs of Au compared to theoretical predictions for conventional spectrum.

It can be observed that the uncertainty is higher than what proposed by Crosbie et al. [49], and this is due to both considering more uncertainty factors and using a larger thickness of extra materials, as require to find the different HVLs using Al that is less absorbing than the Cu.
The last analysis on HVLs experimental measurements was performed to confirm more clearly that the 22 mm of PMMA are a good approximation for the IC0bis. As already shown in the previous section, the clinical spectra with PMMA and that with the IC0bis instead are almost equivalent. To quantify this similarity, the measured IR for the same

Pre-clinical	Experimental Cu [mm]	Theoretical [mm]	% diff
HVL1	2.28 ± 0.14	2.27 ± 0.05	0.37
HVL2	5.20 ± 0.32	5.21 ± 0.10	-0.13
HVL3	8.77 ± 0.54	8.70 ± 0.17	0.86

(a)

Pre-clinical	Experimental Al [mm]	Theoretical [mm]	% diff
HVL1	16.51 ± 1.01	16.46 ± 0.33	0.33
HVL2	33.50 ± 2.06	33.45 ± 0.67	0.14
HVL3	50.95 ± 3.13	50.91 ± 1.02	0.07

(b)

Table 3.4: (a). Experimental measured HVLs of Cu compared to theoretical predictions for pre-clinical spectrum. (b). Experimental measured HVLs of Al compared to theoretical predictions for pre-clinical spectrum.

Clinical	Experimental Cu [mm]	Theoretical [mm]	% diff
HVL1	2.37 ± 0.15	2.37 ± 0.05	0.19
HVL2	5.40 ± 0.33	5.4 ± 0.11	0.02
HVL3	9.08 ± 0.56	8.99 ± 0.1	1.01

(a)

Clinical	Experimental Al [mm]	Theoretical [mm]	% diff
HVL1	16.73 ± 1.02	16.69 ± 0.33	0.22
HVL2	33.91 ± 2.08	33.88 ± 0.68	0.08
HVL3	51.54 ± 3.16	51.54 ± 1.03	0.00

(b)

Table 3.5: (a). Experimental measured HVLs of Cu compared to theoretical predictions for clinical spectrum. (b). Experimental measured HVLs of Al compared to theoretical predictions for pre-clinical spectrum.

extra layer thickness was compared for both these two spectra. In plot 3.8 is shown the percentage difference between the values (calculated as the $\frac{(IR_{spec7} - IR_{spec7})}{IR_{spec7}}$ % in function of the extra Al sheets thickness obtained.
As it can be seen from the plot, the % difference goes up to 1% at maximum. Similar results were obtained for the insertion of Cu layer instead than Al, hence it can be confirmed that the 22 mm of PMMA can be used to approximate well the IC0bis.

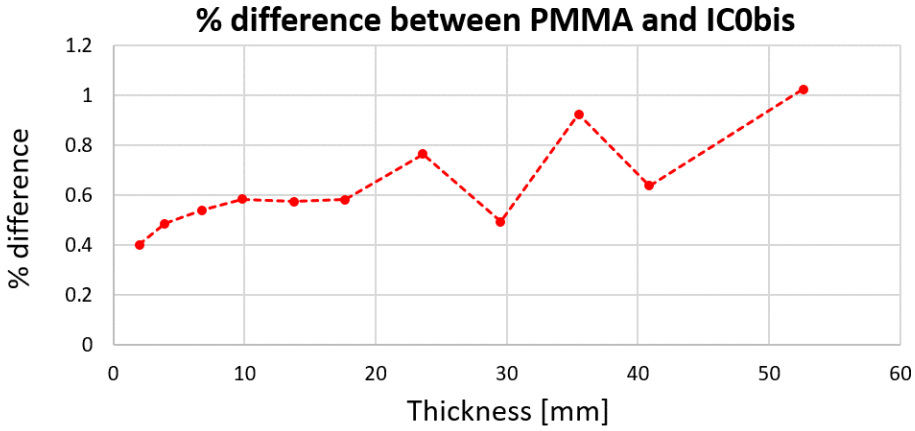

Figure 3.8: % difference between IR measured values for the same Al extra layer thickness for clinical spectrum with PMMA and clinical spectrum with IC0bis.

3.3. Depth dose profile

In this section the results of the depth dose profile measurement are shown and compared to the Monte Carlo simulations. To facilitate the result analysis, the comparison between the results obtained with the two types of different Monte Carlo approaches are presented.

3.3.1. Monte Carlo simulations: conventional vs. hybrid algorithm

As already presented in section 2, two different types of Monte Carlo simulations were performed: conventional MC and hybrid MC. The hybrid MC is based on a different dose calculation algorithm and can be considered a good and independent alternative to conventional MC simulations. In Figure 3.9 is shown an interface of resulting dose distribution of the simulation for the clinical spectrum using the hybrid algorithm on the $Eclipse_{TM}$ TPS. The purpose of the first analysis here presented, is to compare the two different types of MC simulations obtained starting from the same spectrum, to confirm their equivalence.

The analysis is performed on the conventional spectrum, the pre-clinical one and the clinical one. The results are shown in Figures 3.10, 3.11 and 3.12: for each of them on the top plot is shown the comparison between the dose profile of the two different simulations as a function of the depth inside the water equivalent phantom, while on the bottom plot the % difference between the two datasets is calculated as:

$$\%\, difference = \frac{(IR_{hybridMC} - IR_{conventionalMC})}{IR_{conventionalMC}}\,\% \tag{3.7}$$

The maximum difference between the two datasets is around 1% close to the exit wall of the phantom, while at the entrance of the cube is negligible. The hybrid simulations are almost equivalent to the conventional ones. The difference can be explained by the fact that hybrid simulations can potentially be less precise for how the interaction of electrons and matter is managed using an electron kernel. Secondly, for the conventional MC a number of photons 20 times higher than that used for hybrid MC have been simulated, generating much more history and thus, a higher precision. As it was shown in equation 2.15, the higher the number of histories the smaller the error of the simulations. Even if both these factor can be further developed to increase the agreement between the simulations, we can state that for this setup the hybrid MC simulations are matching the conventional MC ones.
The uncertainties on both the MC simulations are very low, as explained in section 2.6.4, hence the resulting small vertical error bars were not reported for an easier plot reading.

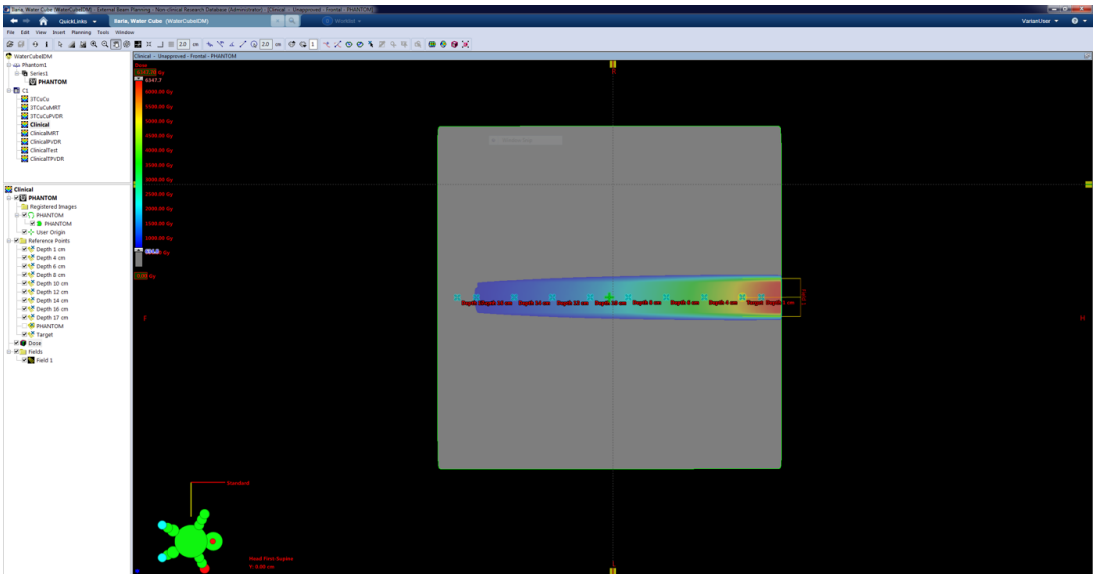

Figure 3.9: In the image is shown a screenshot of the *Eclipse*^{TM} TPS showing the dose distribution inside the cube resulting from the simulation. The phantom is observed from the top while the beam is entering from the right. The points indicated with a cross on the image are highlighting the depth inside the phantom at which the dose was experimentally measured.

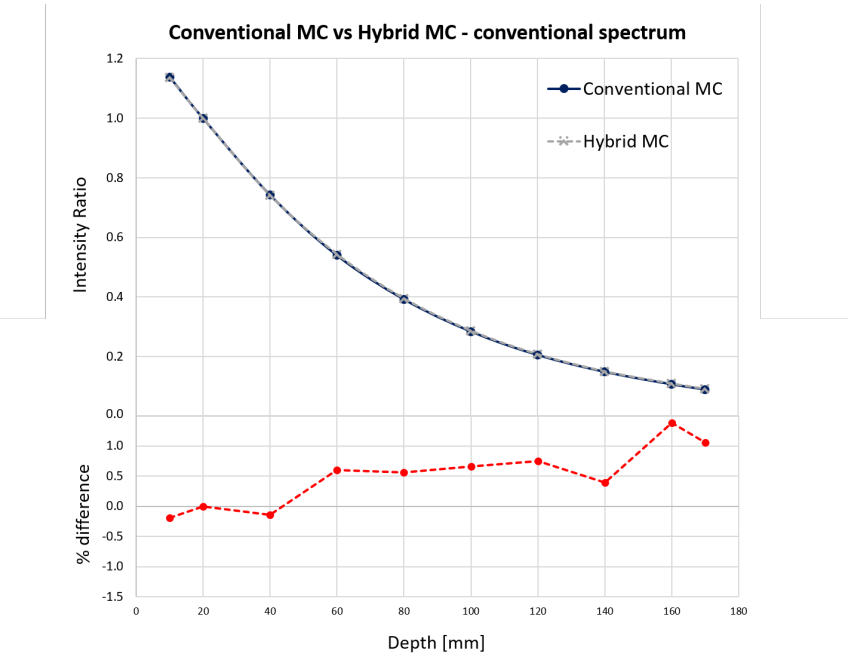

Figure 3.10: Conventional spectrum. On top, the plots of the depth dose profile for the conventional MC simulation and the hybrid MC simulation are shown. On bottom, the % difference between the two different set of data is plotted.

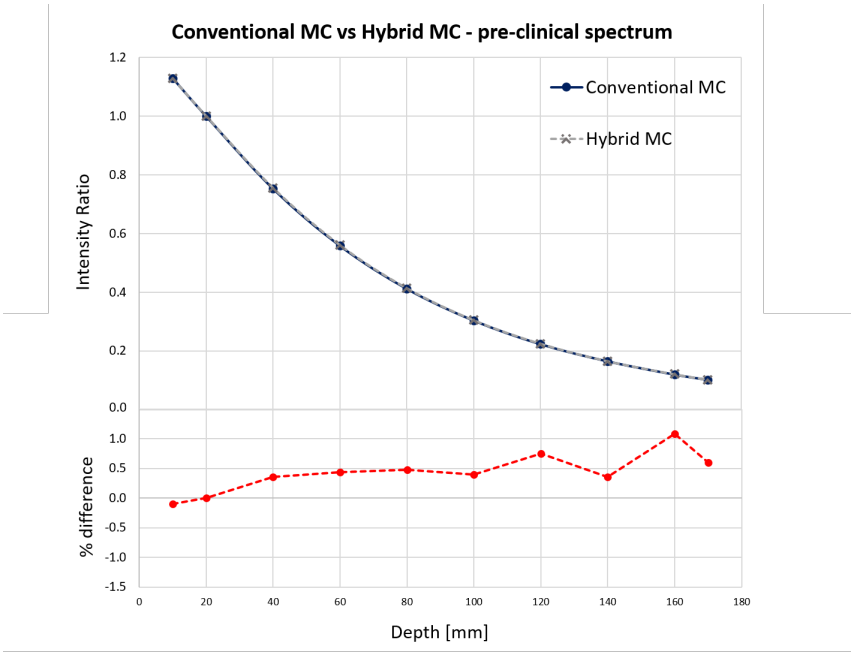

Figure 3.11: Pre-clinical spectrum. On top plot the conventional MC simulation profile and the hybrid MC simulation profile are shown. On bottom plot the % difference between the two different set of data is shown.

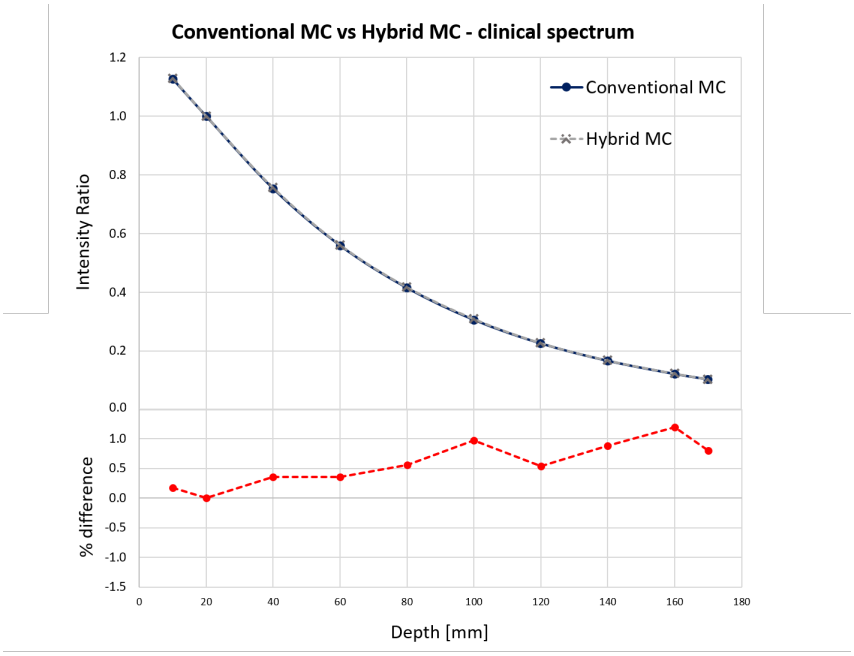

Figure 3.12: Clinical spectrum. On top plot the conventional MC simulation profile and the hybrid MC simulation profile are shown. On bottom plot the % difference between the two different set of data is shown.

3.3.2. Experimental dosimetry

Now that the accuracy of the simulations has been proven, the simulated data can be compared with the actual measured one, obtained both from the PinPoint and from the radiochromic films. To facilitate the reading of the plots presented for the results analysis, only the conventional MC dataset will be used.

The data obtained with the PinPoint are once again adjusted by taking into account the correcting factors for the device. The same approach described in the previous section, 3.1.2, has been used. The k_Q correcting factor for the mean energy of the beam has been recalculated at each depth inside the phantom where the PinPoint was placed, to take into account the attenuating power of the water on the energy of the spectrum. The $k_{T,P}$ correcting factor, instead hasn't been recalculated for any iteration of the PinPoint, because, being this one inside the water equivalent cube, the experimental setup was not allowing a suitable placement of the thermocouples. Only the T and P measured before starting the experiment have been used: the resulting correcting factor $k_{T,P}$ was directly inserted in the electrometer before the beginning of the measurements. For the k_s factor the equation 3.4 is used without any change, depending only on the measured dose rate.

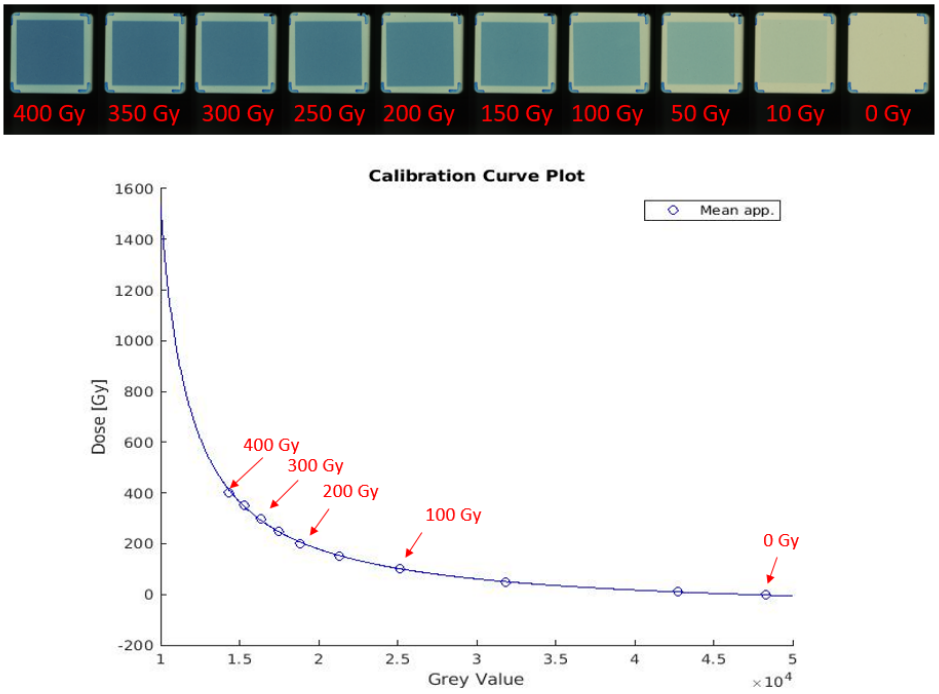

Figure 3.13: The figure shows the calibration curve for the pre-clinical spectrum obtained, turning the color of the irradiated films (shown on top) into a scale of grey. Knowing the dose used to irradiate each of the films (written in red over the images of the films), the calibration curve allows to turn any value of grey into an absolute dose value.

For what regards the film dosimetry, in Figure 3.13 the obtained calibration curve from the irradiated radiochromic films for the preclinical spectrum is shown. It can be seen how the "color" of the irradiated films is translated into a grey value, and associated after to the absolute value of dose it was irradiated with. The calibration curves obtained from the fitting in equation 2.14 all have an R^2 value above 0.99, meaning that the used fit is well representing the behavior.
Once the dose on the to the film for depth dose measurement have been established by comparison with the calibration curve, the IR is calculated normalizing the dose value for each film by the nominal dose used to irradiate the film in reference conditions, i.e. the one 2 cm in deep inside the cube, that is a known value. The IR curve were then compared to the data obtained with the MC simulations.
In Figures 3.14, 3.15 and 3.16, the IR values obtained with both films and PinPoint measurement are compared to the conventional Monte Carlo simulations for the following spectra: conventional, pre-clinical and clinical.

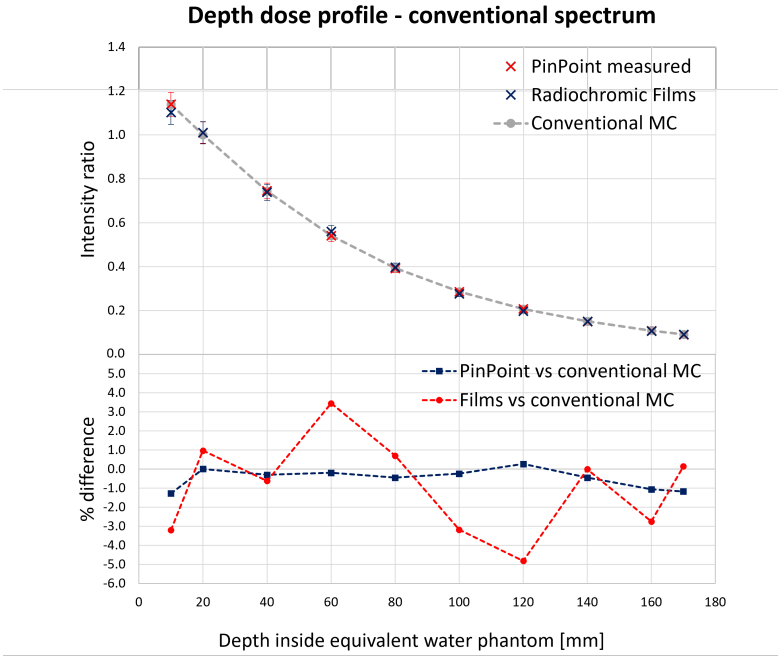

Figure 3.14: Conventional spectrum. Top plot shows the measured IR at different depth inside the cube compared to the results obtained with the conventional MC simulations. Bottom plot shows the % difference between the measured data and both the simulated data.

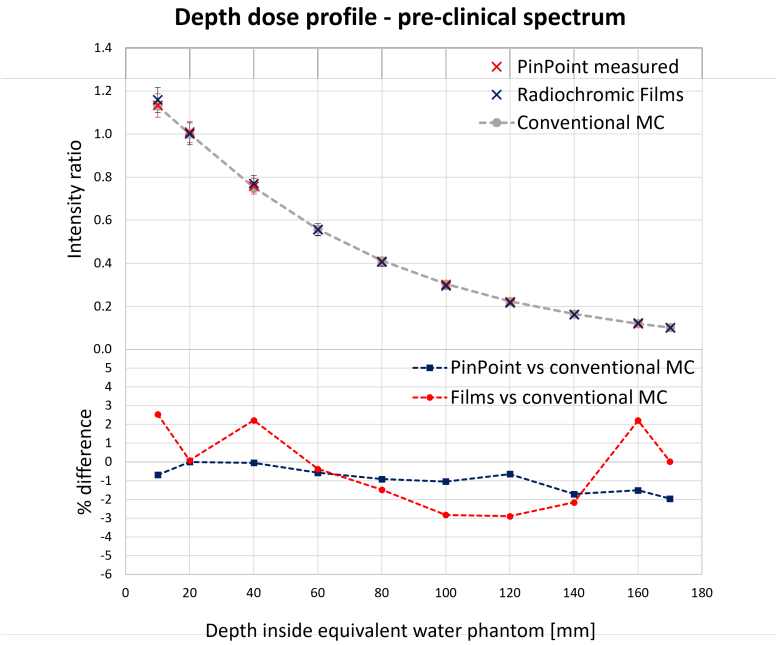

Figure 3.15: Pre-clinical spectrum. Top plot shows the measured IR at different depth inside the cube compared to the results obtained with the conventional MC simulations. Bottom plot shows the % difference between the measured data and both the simulated data.

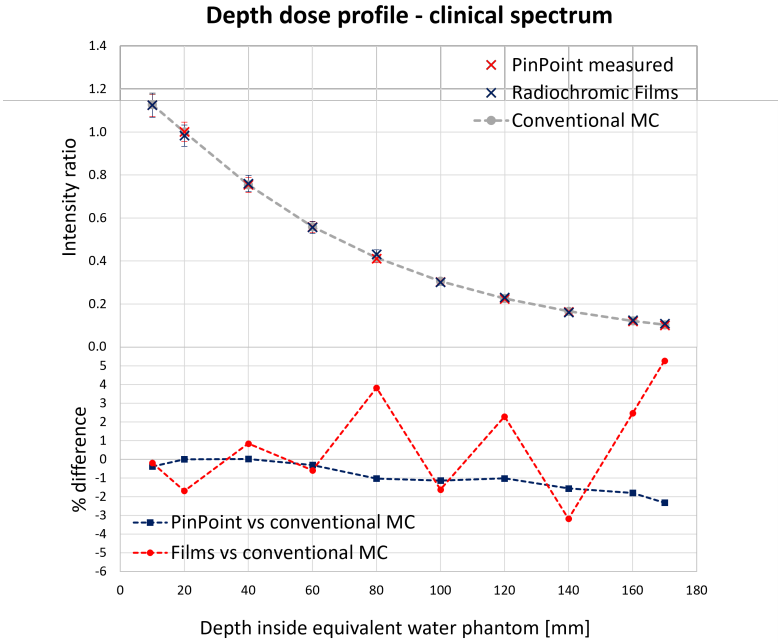

Figure 3.16: Clinical spectrum. Top plot shows the measured IR at different depth inside the cube compared to the results obtained with the conventional MC simulations. Bottom plot shows the % difference between the measured data and both the simulated data.

The results for the depth dose profile in water obtained with the PinPoint show that the % difference stays always below 3%, like already happened for HVL measurements. For the radiochromic films instead, the resulting % difference with respect to the MC simulations stays within 3% for most of the points, but few points are going up to 5% difference. The uncertainties of the experimental points (see section 2.6.3) are graphically represented on the plots as vertical error bars one the measured data.
The uncertainty on the conventional MC simulations is very low, as explained in section 2.6.4, hence the error bars are so small that they have not been reported, to facilitate the plot reading. In Figure 3.17 it is shown the resulting dose deposition of one conventional MC simulation along with the uncertainty calculated on the first and on the last slice in which the cubic phantom is divided for the simulations.
The results are overall satisfactory. All differences between datasets are smaller than the error bars, and in most of the cases below the 3% value that is necessary to validate irradiation in a clinical scenario. Only few dose values from film dosimetry are above the 3% difference with respect to MC simulations, but these can be considered acceptable looking at the higher level of uncertainties associated to film measurements. Considering the entire set of measurements, including two independent dose calculation and two different detectors used for dose measurements, the dosimetry validation obtained by using

the newly characterized spectra can be considered reliable for MRT application.

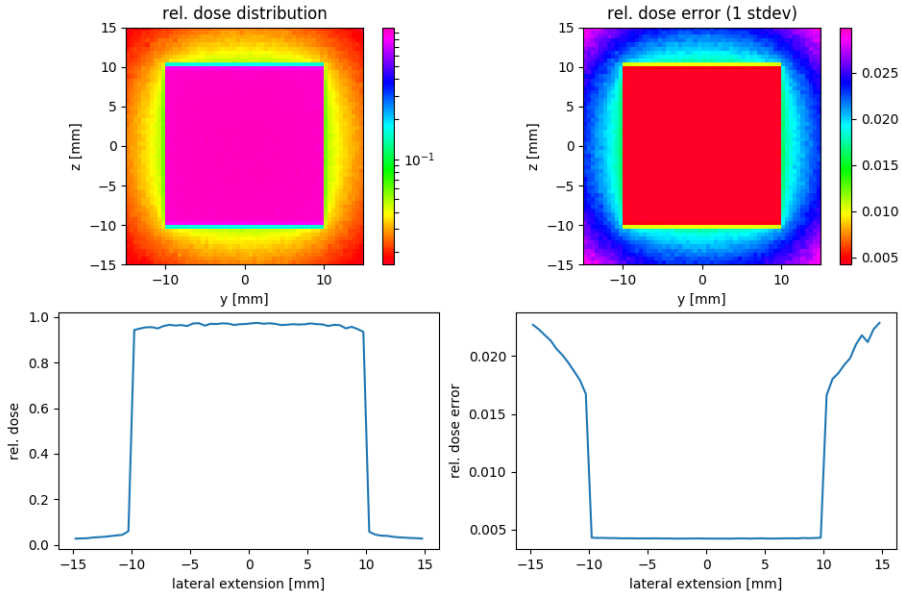

(a)

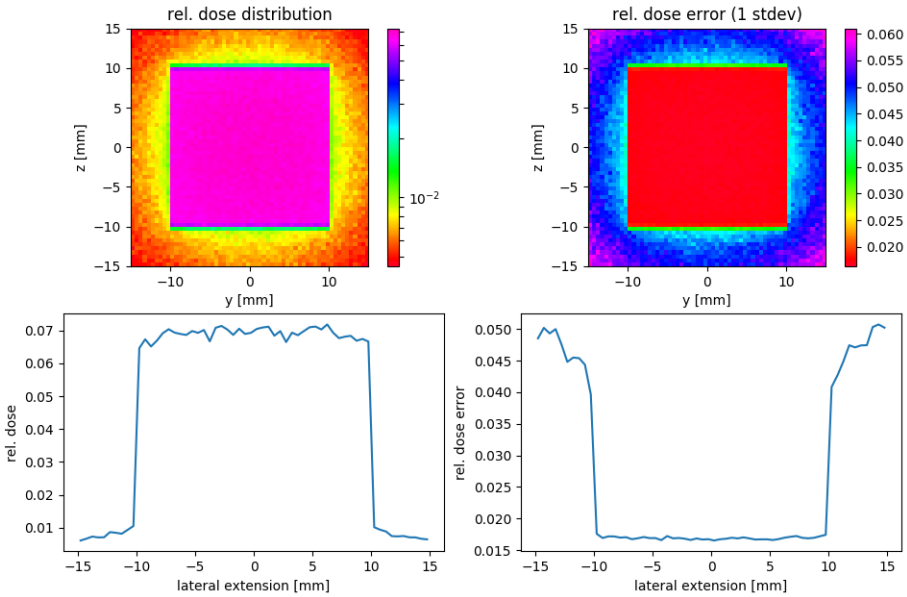

(b)

Figure 3.17: (a). Conventional MC simulation for clinical spectrum, the first 0.5 mm thick slice at the entrance of the phantom is considered. On the top-left the resulting 2-dimensional dose distribution is shown, while the dose profile along the horizontal field extension is reported in the bottom-left plot. On the right of the figure, the 2-dimensional uncertainty map and the details of the uncertainty plot are shown for the same first slice inside the cube. (b). The figure reports the same study for the last slice of the phantom, showing the increased uncertainty on the dose definition.

4 | Discussion

The aim of this work was the charcaterization of the X-ray spectra used at the ESRF - ID17 biomedical beamline for RT experiments. This study was necessary due to the reconstruction of the ESRF storage ring that brought to life the first fourth generation synchrotron in the world as well as the renovation of some components of the beamline in the last years. In RT, in fact, a highly accurate dosimetry before treatments is mandatory and a precise knowledge of the X-ray spectrum is at its foundation. After the spectra characterization, a dosimetry study for homogeneous field irradiation on the beamline has been conducted, focusing on the three most used spectra in preclinical and clinical trials. In the following sections, a discussion about the methods and instrumentation used along with the results obtained will be presented.

4.0.1. Spectra calculation and Half Value Layers

For the first time the OASYS software, specifically the last version of the Shadow library, has been used at ID17 to simulate the X-ray wiggler spectrum obtaining extremely satisfactory results. Nevertheless, the ray tracing algorithm at the base of the Shadow library requests a high number of photons to obtain precise results with a consequent long computation time. The study of an analytical approach, able to reduce the calculation time while keeping the same reliability and level of details provided by the Shadow library, is already under investigation. With this new approach it would be also convenient to perform the complete simulation of the beamline, including the attenuators and monitoring devices part, directly on the OASYS software, avoiding the Python simulations step, as done for this work. The choice to split the simulation of the final spectra in two parts was made because performing the ray tracing technique for all the attenuators and monitoring devices of the beamline would have been very time consuming from the computational point of view.

A new feature implemented in OASYS is the possibility to use the measured magnetic field of the insertion device to take into account the finite dimension of the device, instead of one obtained from theory simulated as perfectly sinusoidal. This approach can be considered more realistic and correct as well, as shown by the agreement within 2% between

simulated and measured HVLs. The characterization was done only for the clinical setup with the wiggler in a narrow configuration at 24.8 mm, the one used for RT experiments, but the use of the measured magnetic field could be extended to different configurations of the insertion device.

Analyzing more in detail the attenuation measurement for all the IR experimental points, the % deviation with respect to simulated data was below 3%, mostly below 2%. The agreement is even improved when considering the exact value of the HVL obtained by fitting the measured IR curve, as explained in section 3.2. The percentage difference between the fitted HVL values and the simulated ones is always below 2%, and averaging the obtained % difference values, the result stays below 0.5% for each spectrum considered. This confirms that the polynomial fitting used for the IR curve is actually a good choice. The HVL measurement results confirm that the theoretical model used, i.e. the OASYS and python simulation, are representing well the real situation and to further improve the precision for HVL measurement and reduce the uncertainty, thicker blocks of Cu and Al should be preferred instead of using a large number of thin layers.

A significant improvement of the agreement between simulation and experiment arrived from the use of all the PinPoint correcting factors that, to our knowledge, was never so deeply investigated. The k_Q correcting factor has been of importance especially for the measurement when a significant number of additional layers were inserted in the beam path, moving the mean energy of the X-ray beam far from that of the TH200 beam quality. The k_s factor gave an important contribution as well, considering that from the higher dose rate to the lowest one it changes up to 1.2%. The $k_{T,P}$ factor contribution was mainly due to the T variation in the chamber during the measurement, while the P remained almost constant for the whole duration of the experiment.

Overall, it can be concluded that the results show an improvement with respect to the work of Crosbie et al. [49]: this validates the potentiality for the use of the OASYS software for future studies and confirms as well that the precise use of all the PinPoint correcting factors can really ameliorate the results .

From the spectrum simulation and HVL measurement it has been possible to confirm as well the hypothesis that the IC0bis ionization chamber (IC) can be well approximated by 22 mm of PMMA: the experimental IR points obtained from the two different configurations only show a maximum of 1% difference. When the IC0bis ionization chamber is not needed for its monitoring functions during clinical trials, the PMMA can be used at its place, avoiding the deterioration of the fragile device when not necessary.

4.0.2. Depth dose profile

Moving on to the dosimetry validation, the depth dose profile study provided a confirmation about the possibility to deliver the desired dose into a basic target volume, represented by water-equivalent plastic, while using a homogeneous synchrotron X-ray beam. To reinforce the validity of the results, two different simulation approaches (conventional and hybrid algorithm MC simulations) and two independent dosimeters (PinPoint ionization chamber (IC) for absolute dosimetry and radiochromic films for relative dosimetry) were used.

Regarding the Monte Carlo simulations, the correspondence between the conventional MC and hybrid MC results is quite good, below 1.2%. The remaining difference could be caused by the different physics libraries used for the two types of simulations as well as due to different Geant4 versions used. Increasing the number of photons simulated with the hybrid algorithm could improve the uncertainty budget related to this method, but would not improve the accordance between the two methods.

Regarding the data obtained with the PinPoint IC in the water phantom, the agreement between the experimental values and the simulated values from the conventional MC is excellent, being below 3% for all the spectra, as shown in section 3.3.2 for the three main spectra. The use of the correcting factors for the PinPoint IC, in this case only k_Q and k_s for each of the measurement, improved again the goodness of the final data. A further improvement in the measurement could be obtained using an actual water phantom instead of the equivalent to water material cube. The water equivalent phantom, even if projected for clinical use in RT, was not specifically designed for irradiation with low keV photons.

Radiochromic film dosimetry provided overall the less convincing agreement, even if the percentage difference between the experimental and simulated data was below 3 % for most of the studied points, with an exception only for few data points. The radiochromic films measurement are the most critical: obtaining absolute values from the irradiated films required few passages, such as the definition of a calibration curve under reference conditions, hence different sources of error were introduced. Both for the calibration curve and for the film used for the measurement, an average over grey values of three different films irradiated with the same nominal dose was giving a standard deviation up to 2.3 %. This shows that still there was a quite high variation in the film reading with respect to the PinPoint IC measurements.

Even if the scanner was used for film reading only after an adequate warm-up, the instrument may not be stable over the entire range of time of a few hours necessary to read out all the films, therefore introducing brightness variation in the acquired images.

To reduce the uncertainties on the film read-out related to possible inhomogeneities of the active material, a more strict protocol could be introduced, confronting film after the irradiation with a pre-scanned image in a more systematic way.

Overall the results are very satisfactory, the study has been performed in a complete and systematic way, bringing the innovation related to the use of new software that opens new possibilities for future researches. The obtained results confirms that the spectra simulated starting from the OASYS software are matching the real spectrum configuration at the ID17 beamline, hence they can be used for further studies, improving what was obtained in the past. The dosimetry study performed showed that, on average, all the four dataset obtained from simulation and experiments are in agreement within the 3% range, satisfying the typical level of agreement used in the clinic for conventional RT applications with a homogeneous irradiating field. The natural follow-up of this work is the application of the characterized X-ray spectra for dosimetry study in the typical MRT configuration, i.e. using arrays of microbeams for the field definition.

5 | Conclusion

The development of the MRT project toward a clinical reality is of great importance because the spatial fractionation technique could push a step further the research to defeat cancer. Moving MRT toward a clinical stage, requires very robust and reliable dosimetric protocols, and at the basis of these a very precise knowledge of the photon spectrum characteristics is needed. The goal of this study was the characterization of the X-ray spectrum at ID17, the biomedical beamline at the ESRF, after the recent renovation of the storage ring and of the beamline.

The study characterization has been performed using the Half Value Layer method that consists in measuring the attenuation of the spectrum when additional layer where introduced in the beam path, to find the thickness that is able to attenuate the spectrum intensity to half of its initial value. The experimental results were compared to the final spectra at ID17 simulated by OASYS software and Python code, in-house developed at ID17 during the study. The results obtained are excellent: the agreement between the theoretical and experimental data for the HVL are always below 3% and in most of cases below 1%. The OASYS software is able to predict with reliability the spectrum generated by the ID17 wiggler and the HVL values show a better agreement than that obtained in the previous literature [49]. The complete use of correcting factor for the ionization chamber detector used during measurement provided a significant improvement for the data agreement.

The newly characterized spectra have been used for dosimetry studies in reference conditions with a homogeneous broad beam, measuring the depth dose profile delivered into a water-equivalent phantom. This study was performed both with absolute measurement by mean of a PTW PinPoint IC detector and with relative measurement using radiochromic films. The resulting sets of data were compared to two independent Monte Carlo simulations datasets of the used setup. The results obtained for absolute measurements using the PTW ionization chamber show that the differences with respect to simulated depth dose profiles are always below 3%, the limit value considered in conventional RT to validate a treatment plan. Film dosimetry can be considered satisfactory, with most of the dosimetry values respecting the 3% limit of difference with respect to calculated doses,

even if there are few outliers, hence a further investigation of the protocol used can potentially improve the final agreement.
This work show that a reliable X-ray spectra definition can performed at the ESRF-ID17 biomedical beamline for continuing studies in the radiation therapy field also after the storage ring upgrade and the most recent beamline modifications. The dosimetry validation confirmed that the definition of radiation plans under reference conditions can be considered correct for phantom configuration tested. These results can be considered the correct starting point for future works concerning dose calculation and treatment planning in a clinical scenario for all the necessary RT applications developed at ID17 beamline.

Bibliography

[1] "Cancer." https://www.who.int/health-topics/cancer.

[2] "How chemotherapy works." https://www.cancerresearchuk.org/about-cancer/cancer-in-general/treatment/chemotherapy/how-chemotherapy-works.

[3] W. C. Röntgen, "Ueber eine neue art von strahlen," *Annalen der Physik*, vol. 300, no. 1, p. 12–17, 1898.

[4] S. R. Adhikari, "Effect and application of ionization radiation (x-ray) in living organism," *Himalayan Physics*, vol. 3, p. 89–92, 2013.

[5] M. Donzelli, *Improving dose calculation and treatment planning techniques for microbeam radiation therapy with computational methods*. PhD thesis, ICR–Institute of Cancer Research Sutton, UK, 2018.

[6] S. Gianfaldoni, R. Gianfaldoni, U. Wollina, J. Lotti, G. Tchernev, and T. Lotti, "An overview on radiotherapy: From its history to its current applications in dermatology," *Open Access Macedonian Journal of Medical Sciences*, vol. 5, no. 4, p. 521–525, 2017.

[7] C. J. Dean, M. G. Ormerod, R. W. Serianni, and P. Alexander, "Dna strand breakage in cells irradiated with x-rays," *Nature*, vol. 222, no. 5198, p. 1042–1044, 1969.

[8] G. C. Barnett, C. M. West, A. M. Dunning, R. M. Elliott, C. E. Coles, P. D. Pharoah, and N. G. Burnet, "Normal tissue reactions to radiotherapy: Towards tailoring treatment dose by genotype," *Nature Reviews Cancer*, vol. 9, no. 2, p. 134–142, 2009.

[9] P. P. Connell and S. Hellman, "Advances in radiotherapy and implications for the next century: A historical perspective," *Cancer Research*, vol. 69, no. 2, p. 383–392, 2009.

[10] L. R. Holsti, "Development of clinical radiotherapy since 1896," *Acta Oncologica*, vol. 34, no. 8, p. 995–1003, 1995.

[11] S. Bartzsch, S. Corde, J. C. Crosbie, L. Day, M. Donzelli, M. Krisch, M. Lerch, P. Pel-

licioli, L. M. Smyth, M. Tehei, and et al., "Technical advances in x-ray microbeam radiation therapy," *Physics in Medicine & Biology*, vol. 65, no. 2, 2020.

[12] E. Bräuer-Krisch, H. Requardt, P. Régnard, S. Corde, E. Siegbahn, G. LeDuc, T. Brochard, H. Blattmann, J. Laissue, A. Bravin, and et al., "New irradiation geometry for microbeam radiation therapy," *Physics in Medicine and Biology*, vol. 50, no. 13, p. 3103–3111, 2005.

[13] J. W. Hopewell, A. D. Morris, and A. Dixon-Brown, "The influence of field size on the late tolerance of the rat spinal cord to single doses of x rays," *The British Journal of Radiology*, vol. 60, no. 719, p. 1099–1108, 1987.

[14] B. Emami, J. Lyman, A. Brown, L. Cola, M. Goitein, J. Munzenrider, B. Shank, L. Solin, and M. Wesson, "Tolerance of normal tissue to therapeutic irradiation," *International Journal of Radiation Oncology, Biology, Physics*, vol. 21, no. 1, p. 109–122, 1991.

[15] J. A. Laissue, H. Blattmann, and D. N. Slatkin, "Alban köhler (1874-1947): Erfinder der gittertherapie," *Zeitschrift für Medizinische Physik*, vol. 22, no. 2, p. 90–99, 2012.

[16] W. Zeman, H. J. Curtis, and C. P. Baker, "Histopathologic effect of high-energy-particle microbeams on the visual cortex of the mouse brain," *Radiation Research*, vol. 15, no. 4, p. 496, 1961.

[17] J. A. Laissue, H. Blattmann, M. Di Michiel, D. N. Slatkin, N. Lyubimova, R. Guzman, W. Zimmermann, S. Birrer, T. Bley, P. Kircher, and et al., "Weanling piglet cerebellum: a surrogate for tolerance to mrt (microbeam radiation therapy) in pediatric neurooncology," *SPIE Proceedings*, 2001.

[18] H. Blattmann, J.-O. Gebbers, E. Bräuer-Krisch, A. Bravin, G. Le Duc, W. Burkard, M. Di Michiel, V. Djonov, D. Slatkin, J. Stepanek, and et al., "Applications of synchrotron x-rays to radiotherapy," *Nuclear Instruments and Methods in Physics Research Section A: Accelerators, Spectrometers, Detectors and Associated Equipment*, vol. 548, no. 1-2, p. 17–22, 2005.

[19] D. N. Slatkin, P. Spanne, F. A. Dilmanian, and M. Sandborg, "Microbeam radiation therapy," *Medical Physics*, vol. 19, no. 6, p. 1395–1400, 1992.

[20] F. A. Dilmanian, T. M. Button, G. Le Duc, N. Zhong, L. A. Pena, J. A. L. Smith, S. R. Martinez, T. Bacarian, T. Jennifer, R. Baorui, P. M. Farmer, K.-E. John, P. L. Micca, M. M. Nawrocky, J. A. Niederer, F. P. Recksiek, A. Fuchs, and E. M.

Rosen, "Response of rat intracranial 9l gliosarcoma to microbeam radiation therapy," *Neuro-Oncology*, vol. 4, no. 1, pp. 26–38, 2002.

[21] J. C. Crosbie, R. L. Anderson, K. Rothkamm, C. M. Restall, L. Cann, S. Ruwanpura, S. Meachem, N. Yagi, I. Svalbe, R. A. Lewis, and et al., "Tumor cell response to synchrotron microbeam radiation therapy differs markedly from cells in normal tissues," *International Journal of Radiation Oncology, Biology, Physics*, vol. 77, no. 3, p. 886–894, 2010.

[22] A. Bouchet, N. Sakakini, M. El Atifi, C. Le Clec'h, E. Brauer, A. Moisan, P. Deman, P. Rihet, G. Le Duc, L. Pelletier, and et al., "Early gene expression analysis in 9l orthotopic tumor-bearing rats identifies immune modulation in molecular response to synchrotron microbeam radiation therapy," *PLoS ONE*, vol. 8, no. 12, 2013.

[23] A. Bouchet, N. Sakakini, M. E. Atifi, C. Le Clec'h, E. Bräuer-Krisch, L. Rogalev, J. A. Laissue, P. Rihet, G. Le Duc, L. Pelletier, and et al., "Identification of areg and plk1 pathway modulation as a potential key of the response of intracranial 9l tumor to microbeam radiation therapy," *International Journal of Cancer*, vol. 136, no. 11, p. 2705–2716, 2014.

[24] A. Bouchet, B. Lemasson, G. Le Duc, C. Maisin, E. Bräuer-Krisch, E. A. Siegbahn, L. Renaud, E. Khalil, C. Rémy, C. Poillot, and et al., "Preferential effect of synchrotron microbeam radiation therapy on intracerebral 9l gliosarcoma vascular networks," *International Journal of Radiation Oncology, Biology, Physics*, vol. 78, no. 5, p. 1503–1512, 2010.

[25] A. Bouchet, B. Lemasson, T. Christen, M. Potez, C. Rome, N. Coquery, C. Le Clec'h, A. Moisan, E. Bräuer-Krisch, G. Leduc, and et al., "Synchrotron microbeam radiation therapy induces hypoxia in intracerebral gliosarcoma but not in the normal brain," *Radiotherapy and Oncology*, vol. 108, no. 1, p. 143–148, 2013.

[26] A. Bouchet, D. G. Le, and L. Pelletier, *Reponse transcriptomique des tissues cerebraux sains et tumoraux a la radiotherapie par microfasceaux synchrotron*. PhD thesis.

[27] M. Durante, E. Brauer-Krisch, and M. Hill, "Faster and safer? flash ultra-high dose rate in radiotherapy," *The British Journal of Radiology*, p. 20170628, 2017.

[28] J. Bourhis, W. J. Sozzi, P. G. Jorge, O. Gaide, C. Bailat, F. Duclos, D. Patin, M. Ozsahin, F. Bochud, J.-F. Germond, and et al., "Treatment of a first patient with flash-radiotherapy," *Radiotherapy and Oncology*, vol. 139, p. 18–22, 2019.

[29] V. Favaudon, L. Caplier, V. Monceau, F. Pouzoulet, M. Sayarath, C. Fouillade,

M.-F. Poupon, I. Brito, P. Hupé, J. Bourhis, and et al., "Ultrahigh dose-rate flash irradiation increases the differential response between normal and tumor tissue in mice," *Science Translational Medicine*, vol. 6, no. 245, 2014.

[30] E. Schultke, J. Balosso, T. Breslin, G. Cavaletti, V. Djonov, F. Esteve, M. Grotzer, G. Hildebrandt, A. Valdman, J. Laissue, and et al., "Microbeam radiation therapy — grid therapy and beyond: a clinical perspective," *The British Journal of Radiology*, vol. 90, no. 1078, p. 20170073, 2017.

[31] A. Bouchet, M. Potez, N. Coquery, C. Rome, B. Lemasson, E. Bräuer-Krisch, C. Rémy, J. Laissue, E. L. Barbier, V. Djonov, and et al., "Permeability of brain tumor vessels induced by uniform or spatially microfractionated synchrotron radiation therapies," *International Journal of Radiation Oncology, Biology, Physics*, vol. 98, no. 5, p. 1174–1182, 2017.

[32] P. Régnard, E. Bräuer-Krisch, I. Troprès, J. Keyriläinen, A. Bravin, and G. Le Duc, "Enhancement of survival of 9l gliosarcoma bearing rats following intracerebral delivery of drugs in combination with microbeam radiation therapy," *European Journal of Radiology*, vol. 68, no. 3, 2008.

[33] A. Bouchet, A. Boumendjel, E. Khalil, R. Serduc, E. Bräuer, E. A. Siegbahn, J. A. Laissue, and J. Boutonnat, "Chalcone jai-51 improves efficacy of synchrotron microbeam radiation therapy of brain tumors," *Journal of Synchrotron Radiation*, vol. 19, no. 4, p. 478–482, 2012.

[34] R. Serduc, E. Bräuer-Krisch, E. A. Siegbahn, A. Bouchet, B. Pouyatos, R. Carron, N. Pannetier, L. Renaud, G. Berruyer, C. Nemoz, and et al., "High-precision radiosurgical dose delivery by interlaced microbeam arrays of high-flux low-energy synchrotron x-rays," *PLoS ONE*, vol. 5, no. 2, 2010.

[35] P. Romanelli and A. Bravin, "Synchrotron-generated microbeam radiosurgery: A novel experimental approach to modulate brain function," *Neurological Research*, vol. 33, no. 8, p. 825–831, 2011.

[36] P. Pellicioli, S. Bartzsch, M. Donzelli, M. Krisch, and E. Bräuer-Krisch, "High resolution radiochromic film dosimetry: Comparison of a microdensitometer and an optical microscope," *Physica Medica*, vol. 65, p. 106–113, 2019.

[37] M. Soellinger, A. K. Rutz, S. Kozerke, and P. Boesiger, "3d cine displacement-encoded mri of pulsatile brain motion," *Magnetic Resonance in Medicine*, vol. 61, no. 1, p. 153–162, 2008.

[38] S. Bartzsch, C. Cummings, S. Eismann, and U. Oelfke, "A preclinical microbeam facility with a conventional x-ray tube," *Medical Physics*, vol. 43, no. 12, p. 6301–6308, 2016.

[39] M. Hadsell, G. Cao, J. Zhang, L. Burk, T. Schreiber, E. Schreiber, S. Chang, J. Lu, and O. Zhou, "Pilot study for compact microbeam radiation therapy using a carbon nanotube field emission micro-ct scanner," *Medical Physics*, vol. 41, no. 6Part1, p. 061710, 2014.

[40] D. Iwanenko and I. Pomeranchuk, "On the maximal energy attainable in a betatron," *Physical Review*, vol. 65, no. 11-12, p. 343–343, 1944.

[41] F. R. Elder, A. M. Gurewitsch, R. V. Langmuir, and H. C. Pollock, "Radiation from electrons in a synchrotron," *Physical Review*, vol. 71, no. 11, p. 829–830, 1947.

[42] "How does the esrf work?," Apr 2018. https://www.esrf.fr/home/education/what-is-the-esrf/how-does-the-esrf-work.html.

[43] G. Brown, K. Halbach, J. Harris, and H. Winick, "Wiggler and undulator magnets — a review," *Nuclear Instruments and Methods in Physics Research*, vol. 208, no. 1-3, p. 65–77, 1983.

[44] K. Wille, "Introduction to insertion devices," Mar 1999. https://cds.cern.ch/record/382323.

[45] G. Geloni, V. Kocharyan, and E. Saldin, "Brightness of synchrotron radiation from wigglers," *Nuclear Instruments and Methods in Physics Research Section A: Accelerators, Spectrometers, Detectors and Associated Equipment*, vol. 807, p. 13–29, 2016.

[46] R. P. Walker, "Depth-of-field effects in wiggler radiation sources: Geometrical versus wave optics," *Physical Review Accelerators and Beams*, vol. 20, no. 2, 2017.

[47] P. Pellicioli, M. Donzelli, J. A. Davis, F. Estève, R. Hugtenburg, S. Guatelli, M. Petasecca, M. L. Lerch, E. Bräuer-Krisch, M. Krisch, and et al., "Study of the x-ray radiation interaction with a multislit collimator for the creation of microbeams in radiation therapy," *Journal of Synchrotron Radiation*, vol. 28, no. 2, p. 392–403, 2021.

[48] E. A. Siegbahn, J. Stepanek, E. Bräuer-Krisch, and A. Bravin, "Determination of dosimetrical quantities used in microbeam radiation therapy (mrt) with monte carlo simulations," *Medical Physics*, vol. 33, no. 9, p. 3248–3259, 2006.

[49] J. C. Crosbie, P. Fournier, S. Bartzsch, M. Donzelli, I. Cornelius, A. W. Stevenson,

H. Requardt, and E. Bräuer-Krisch, "Energy spectra considerations for synchrotron radiotherapy trials on the id17 bio-medical beamline at the european synchrotron radiation facility," *Journal of Synchrotron Radiation*, vol. 22, no. 4, p. 1035–1041, 2015.

[50] M. S. Rio and L. Rebuffi, "Oasys: A software for beamline simulations and synchrotron virtual experiments," *AIP Conference Proceedings*, 2019.

[51] L. Rebuffi and M. Sanchez del Rio, "Oasys (orange synchrotron suite): An open-source graphical environment for x-ray virtual experiments," *Advances in Computational Methods for X-Ray Optics IV*, 2017.

[52] L. Rebuffi and M. Sánchez del Río, "Shadowoui: A new visual environment for x-ray optics and synchrotron beamline simulations," *Journal of Synchrotron Radiation*, vol. 23, no. 6, p. 1357–1367, 2016.

[53] N. Canestrari, D. Karkoulis, and M. Sánchez del Río, "Shadow3-api: The application programming interface for the ray tracing code shadow," *SPIE Proceedings*, 2011.

[54] M. Sanchez del Rio and O. Mathon, "A simple formula to calculate the x-ray flux after a double-crystal monochromator," *SPIE Proceedings*, 2004.

[55] P. Berkvens, E. Brauer-Krisch, T. Brochard, C. Nemoz, M. Renier, P. Fournier, H. Requardt, and M. Kocsis, "Highly robust, high intensity white synchrotron beam monitor," *2013 IEEE Nuclear Science Symposium and Medical Imaging Conference (2013 NSS/MIC)*, pp. 1–3, 2013.

[56] "Ptw bragg peak ionization chamber." https://www.ptwdosimetry.com/en/products/bragg-peak-ionization-chambers/.

[57] W. Elam, B. Ravel, and J. Sieber, "A new atomic database for x-ray spectroscopic calculations," *Radiation Physics and Chemistry*, vol. 63, no. 2, p. 121–128, 2002.

[58] *Absorbed dose determination in external beam radiotherapy: An international code of practice for DSIMETRY based on standards of absorbed dose to water.* International Atomic Energy Agency, 2001.

[59] "Ptw pinpoint ion chamber 31014." https://www.ptwdosimetry.com/en/products/pinpoint-3d-ion-chamber/.

[60] P. Fournier, *Dosimetry in synchrotron microbeam radiation therapy.* PhD thesis, University of Wollongong, Australia, 2016.

[61] P. Fournier, J. C. Crosbie, I. Cornelius, P. Berkvens, M. Donzelli, A. H. Clavel, A. B.

Rosenfeld, M. Petasecca, M. L. Lerch, E. Bräuer-Krisch, and et al., "Absorbed dose-to-water protocol applied to synchrotron-generated x-rays at very high dose rates," *Physics in Medicine and Biology*, vol. 61, no. 14, 2016.

[62] Y. Prezado, I. Martínez-Rovira, S. Thengumpallil, and P. Deman, "Dosimetry protocol for the preclinical trials in white-beam minibeam radiation therapy," *Medical Physics*, vol. 38, no. 9, p. 5012–5020, 2011.

[63] "Easy cube." https://www.lap-laser.com/fr/produits/easy-cube/.

[64] M. Williams, P. Metcalfe, A. Rosenfeld, T. Kron, F. d'Errico, and M. Moscovitch, "Radiochromic film dosimetry and its applications in radiotherapy," *AIP Conference Proceedings*, 2011.

[65] A. Rink, I. A. Vitkin, and D. A. Jaffray, "Suitability of radiochromic medium for real-time optical measurements of ionizing radiation dose," *Medical Physics*, vol. 32, no. 4, p. 1140–1155, 2005.

[66] J. Tsibouklis, C. Pearson, Y.-P. Song, J. Warren, M. Petty, J. Yarwood, M. C. Petty, and W. J. Feast, "Pentacosa-10,12-diynoic acid/henicosa-2,4-diynylamine alternate-layer langmuir–blodgett films: Synthesis, polymerisation and electrical properties," *J. Mater. Chem.*, vol. 3, no. 1, p. 97–104, 1993.

[67] Y. Watanabe, G. N. Patel, and P. Patel, "Evaluation of a new self-developing instant film for imaging and dosimetry," *Radiation Protection Dosimetry*, vol. 120, no. 1-4, p. 121–124, 2006.

[68] D. Lewis, A. Micke, X. Yu, and M. F. Chan, "An efficient protocol for radiochromic film dosimetry combining calibration and measurement in a single scan," *Medical Physics*, vol. 39, no. 10, p. 6339–6350, 2012.

[69] J. Seco, *Monte Carlo techniques in radiation therapy.* CRC Press, 2016.

[70] S. Agostinelli, J. Allison, K. Amako, J. Apostolakis, H. Araujo, P. Arce, M. Asai, D. Axen, S. Banerjee, G. Barrand, and et al., "Geant4—a simulation toolkit," *Nuclear Instruments and Methods in Physics Research Section A: Accelerators, Spectrometers, Detectors and Associated Equipment*, vol. 506, no. 3, p. 250–303, 2003.

[71] G. F. Salvat, M. F. V. Jose, and J. S. Roma, *Penelope 2008: A code system for Monte Carlo simulation of electron and photon transport: Workshop proceedings, Barcelona, Spain 30 June-3 July 2008.* OECD, 2009.

[72] T. R. Mackie, J. W. Scrimger, and J. J. Battista, "A convolution method of calculating dose for 15-mv x rays," *Medical Physics*, vol. 12, no. 2, p. 188–196, 1985.

[73] J. E. O'Connor, "The variation of scattered x-rays with density in an irradiated body," *Physics in Medicine and Biology*, vol. 1, no. 4, p. 352–369, 1957.

[74] S. Bartzsch and U. Oelfke, "A new concept of pencil beam dose calculation for 40-200 kev photons using analytical dose kernels," *Medical Physics*, vol. 40, no. 11, p. 111714, 2013.

[75] M. Donzelli, E. Bräuer-Krisch, U. Oelfke, J. J. Wilkens, and S. Bartzsch, "Hybrid dose calculation: A dose calculation algorithm for microbeam radiation therapy," *Physics in Medicine & Biology*, vol. 63, no. 4, p. 045013, 2018.

[76] S. Bartzsch, *Microbeam radiation therapy: Physical and biological aspects of a new cancer therapy and development of a treatment planning system.* PhD thesis, Verlag nicht ermittelbar, 2014.

[77] L. R. Day, M. Donzelli, P. Pellicioli, L. M. Smyth, M. Barnes, S. Bartzsch, and J. C. Crosbie, "A commercial treatment planning system with a hybrid dose calculation algorithm for synchrotron radiotherapy trials," *Physics in Medicine & biology*, vol. 66, no. 5, p. 055016, 2021.

[78] C. M. Poole, L. R. Day, P. A. Rogers, and J. C. Crosbie, "Synchrotron microbeam radiotherapy in a commercially available treatment planning system," *Biomedical Physics & Engineering Express*, vol. 3, no. 2, p. 025001, 2017.

[79] "X-ray mass attenuation coefficients," Feb 2022. https://www.nist.gov/pml/x-ray-mass-attenuation-coefficients.

[80] "X-ray mass attenuation coefficients," *Journal of Synchrotron Radiation*, pp. https://www.nist.gov/pml/x–ray–mass–attenuation–coefficients.

[81] "Nist uncertainties on x-rays attenuation coefficients." https://physics.nist.gov/PhysRefData/FFast/Text2000/sec06.htmltab2.

[82] P. Pellicioli, F. Esteve, R. Hugtenburg, C. Ceberg, F. Verhaegen, M.-L. Gallin-Martel, and S. Shermer, *Development of radiochromic film dosimetry at Micrometric Scale for microbeam radiation therapy.* PhD thesis, Université Grenoble Alpes, 2019.

[83] D. J. Butler, J. E. Lye, T. E. Wright, D. Crossley, P. H. Sharpe, A. W. Stevenson, J. Livingstone, and J. C. Crosbie, "Absorbed dose determination in kilovoltage x-ray

synchrotron radiation using alanine dosimeters," *Australasian Physical & Engineering Sciences in Medicine*, vol. 39, no. 4, p. 943–950, 2016.

A | Appendix A

In this section the Python code used to obtain the final spectra at the ID17 beamline starting from the resulting raw spectrum from OASYS software is presented. In the following code all the attenuating element are inserted, to obtain the desired spectra, the unwanted components just need to be commented.

```
import math
import xraydb

#function to read from a text file data of brilliance
#and energy and turn them into lists

def read_file(file_name):
    f = open(file_name, 'r')
    elements_ = f.readlines()

    energy_ = []
    brilliance_ = []

    for i in range(len(elements_)):
        words_ = elements_[i].split()
        energy_.append(words_[0])
        brilliance_.append(words_[1])

    # data from file are automatically translated into
    # lists of strings so to perform calculations on them
    # we need to transform them into floats
    # NB: if there is a title to the column of data it must be
    # eliminated before transforming into float
```

```
    del energy_[0]
    del brilliance_[0]

    fl_energy_ = []
    fl_brilliance_ = []

    for i in range(len(energy_)):
        fl_energy_.append(float(energy_[i]))
        fl_brilliance_.append(float(brilliance_[i]))

    print('\nEnergy[eV]: ')
    print(fl_energy_)
    print('\nBrilliance[ph/s/0.1%bw]: ')
    print(fl_brilliance_)
    return fl_energy_, fl_brilliance_


# function to transform brilliance into power
def brilliance_to_power(brilliance_):
    power_ = []
    for iterator_ in brilliance_:
        power_.append(iterator_*1.6*math.pow(10,-19)*1000)

    print('\nPower[W/eV]: ')
    print(power_)
    return power_


# function to make the power sum over the whole spectrum,
# multiplied by the energy step
def power_sum(power_, step_):
    power_sum_ = 0

    for iterator_ in power_:
        power_sum_ = power_sum_ + iterator_
```

```
    return power_sum_*step_


# function to transform the brilliance into flux
def brilliance_to_flux(brilliance_, energy_):
    flux_ = []

    for i in range(len(energy)):
        brilliance_[i]*1000/energy_[i]
        flux_.append(brilliance_[i]*1000/energy_[i])

    print('\nFlux[ph/s]: ')
    print(flux_)
    return flux_


# function that, given an element, returns its attenuation
# length for all the energies involved in a vector
def coefficients(energy_, element_):
    if element_ == 'pmma':
        density_ = 1.18
        coefficient_ = xraydb.material_mu(element_, energy_,
                                          density_, 'total')
    elif element_ == 'graphite carbon':
        density_ = 2.23
        coefficient_ = xraydb.material_mu(element_, energy_,
                                          density_, 'total')
    elif element_ == 'water':
        density_ = 1.0
        coefficient_ = xraydb.material_mu(element_, energy_,
                                          density_, 'total')
    else:
        density_ = xraydb.atomic_density(element_)
        mu_ = xraydb.mu_elam(element_, energy_, 'total')
        #gives back the mu/ro
        coefficient_ = []
        for iterator_ in mu_:
```

```
            coefficient_.append(iterator_ * density_)
            # to return the attenuation length must multiply
            # by density

    print('\nAttenuation coefficient at each energy [1/cm]: ')
    print(coefficient_)
    return coefficient_

# function that return the attenuated spectrum knowing
# the attenuation coefficients, the input brilliance and the
# attenuator thickness
def attenuated_spectra(input_brilliance_, att_coefficients_,
                                                thickness_):
    output_brilliance_ = []

    for i in range(len(input_brilliance_)):
        output_brilliance_.append(input_brilliance_[i] *
                math.exp(-att_coefficients_[i] * thickness_))

    print('\nBrilliance[ph/s/0.1%bw]: ')
    print(output_brilliance_)
    return output_brilliance_


# function to save the output brilliance and corresponding
# energy in a txt file
def output_file(brilliance_, energy_, name, file, percentage):
    str_energy_ = []
    str_brilliance_ = []

    for i in range(len(brilliance_)):
        str_energy_.append(str(energy_[i]))
        str_brilliance_.append(str(brilliance_[i]))

    with open(file, 'a') as f:
        if name == 'Att':
            line = [percentage, ' attenuation \n']
```

```
        else:
            line = [name, '␣Attenuator␣\n']
        f.writelines(line)
        line = ['Photon␣Energy[eV]', '␣␣␣Flux[ph/s/0.1%bw]']
        f.writelines(line)
        for i in range(len(brilliance_)):
            line = ['\n', str_energy_[i],
                    '␣␣␣␣␣␣␣␣␣␣␣␣␣␣', str_brilliance_[i]]
            f.writelines(line)
        line = ['\n␣————␣\n']
        f.writelines(line)


# function that, given the element, the input spectrum and
# the wanted attenuation percentage returns the material
# thickness to obtain that result
# the result can be more or less precise by fixing both
# the step_ and the acceptance_ value that means
# how far we can go from the wanted attenuation,
# for example 50% att means perc_ = 2 cause p0/pf = 2 and
# by choosing acceptance_ = 0.01 we accept as good for result
# the interval [1.99, 2.01]
# NB: be careful in the choice of the two parameters
def hvl_thickness_search(min_val_, max_val_, coefficients_,
            brilliance_, initial_power_sum_, energy_step_, perc_):
    step_ = 0.001
    acceptance_ = 0.005
    i = min_val_

    while i <= max_val_:
        brill_ = attenuated_spectra(brilliance_, coefficients_, i)
        pow_ = brilliance_to_power(brill_)
        print('\np0/pF:')
        pow_sum_ = power_sum(pow_, energy_step_)
        print(initial_power_sum_/pow_sum_)
        if (perc_ - acceptance_) < initial_power_sum_/pow_sum_
                    and (perc_ + acceptance_) >
```

```
                    initial_power_sum_/pow_sum_:
                print('\nWanted thickness found!')
                return i, brill_
            i = i + step_

    print('No HVL thickness for the material
    found in the given interval.')
    return 0.0, brill_


# function that returns a txt file containing all the value
# of p0/pf for increasing thickness of a given material
def thickness_evaluation(coefficients_, brilliance_, p0, energy_step_):
    step_ = 0.001
    min_value = 0.0

    pf = p0
    print(pf)
    power_ratio_ = []
    thickness_ = []

    power_ratio_.append(str(p0/pf))
    thickness_.append(str(min_value))

    while pf/p0 >= 0.05:
        min_value = min_value + step_
        print(min_value)
        brill_ = attenuated_spectra(brilliance_, coefficients_,
                min_value)
        pow_ = brilliance_to_power(brill_)
        pf = power_sum(pow_, energy_step_)
        print(pf)
        print(pf/p0)
        power_ratio_.append(str(pf/p0))
        thickness_.append(str(min_value))

    with open('Spectrum1_Al_IR.txt', 'a') as f:
```

```
        line = ['p0/pf', '   Thickness [cm]']
        f.writelines(line)
        for i in range(len(power_ratio_)):
            line = ['\n', power_ratio_[i], '    ', thickness_[i]]
            f.writelines(line)
        line = ['\n ------- \n']
        f.writelines(line)


if __name__ == '__main__':
    #Menu
    print('Menu: ')
    print('Attenuator 1: Be')
    x = input('Insert thickness [cm]: ')
    att1_thickness = float(x)

    print('\nAttenuator 2: C')
    x = input('Insert thickness [cm]: ')
    att2_thickness = float(x)

    print('\nAttenuator 3: Al')
    x = input('Insert thickness [cm]: ')
    att3_thickness = float(x)

    print('\nAttenuator 4: Cu')
    x = input('Insert thickness [cm]: ')
    att4_thickness = float(x)

    print('\nMaterial to calculate HVL')
    material = input('Insert the chemical name of the element: ')

    #Input Spectrum
    print('\n\nInput spectrum:')
    energy, initial_brilliance = read_file('Shadow_Spectrum.txt')
    step = energy[1] - energy[0]
    initial_power = brilliance_to_power(initial_brilliance)
```

```
#Attenuator 1
print('\n\nAttenuator 1')
att1_coeff = coefficients(energy, 'Be')
att1_brilliance = attenuated_spectra(initial_brilliance,
                                     att1_coeff, att1_thickness)
output_file(att1_brilliance, energy, 'Be', 'Be_att.txt', 0)

#Attenuator 2
print('\n\nAttenuator 2')
att2_coeff = coefficients(energy, 'C')
att2_brilliance = attenuated_spectra(att1_brilliance,
                                     att2_coeff, att2_thickness)
output_file(att2_brilliance, energy, 'C', 'C_att.txt', 0)

#Attenuator 3
print('\n\nAttenuator 3')
att3_coeff = coefficients(energy, 'Al')
att3_brilliance = attenuated_spectra(att2_brilliance,
                                     att3_coeff, att3_thickness)
output_file(att3_brilliance, energy, 'Al', 'Al_att.txt', 0)

#Attenuator 4
print('\n\nAttenuator 4')
att4_coeff = coefficients(energy, 'Cu')
att4_brilliance = attenuated_spectra(att3_brilliance,
                                     att4_coeff, att4_thickness)
output_file(att4_brilliance, energy, 'Cu', 'Cu_att.txt', 0)

#ICO
print('\n\nIC0')
IC0_Au_coeff = coefficients(energy, 'Au')
IC0_brilliance_1 = attenuated_spectra(att4_brilliance,
                                     att3_coeff, 0.2)
IC0_brilliance_2 = attenuated_spectra(IC0_brilliance_1,
                                     IC0_Au_coeff, 0.000028)
output_file(IC0_brilliance_2, energy, 'IC0 attenuator',
                                     'IC0.txt', 0)
```

```
#IC0bis
print('\n\nIC0bis')
IC0bis_coeff_1 = coefficients(energy, 'pmma')
IC0bis_coeff_2 = coefficients(energy, 'graphite carbon')
print(IC0bis_coeff_1)
print(IC0bis_coeff_2)
IC0bis_brilliance_1 = attenuated_spectra(IC0_brilliance_2,
                                         IC0bis_coeff_1, 2.146)
IC0bis_brilliance_2 = attenuated_spectra(IC0bis_brilliance_1,
                                         IC0bis_coeff_2, 0.004)
output_file(IC0bis_brilliance_2, energy, 'ICObis attenuator',
                                         'ICObis_real.txt', 0)

#Phantom
print('\n\nphantom')
phantom_coeff = coefficients(energy, 'water')
phantom_brilliance = attenuated_spectra(IC0_brilliance_2,
                                         phantom_coeff, 17)
output_file(phantom_brilliance, energy, 'phantom',
                                         'phantom.txt', 0)

p0 = brilliance_to_power(IC0bis_brilliance_2)
p0_sum = power_sum(p0, step)
print('\nInitial power sum [W/eV]: ')
print(p0_sum)

print('\n\nHVL calculation:')
mat_HVL_coeff = coefficients(energy, material)
x = input('\nType: 1 for 50% attenuation, 2 for 75% attenuation,'
          '3 for 87.5% attenuation, 4 to get them all, '
          '5 to get all values of thickness 0 to exit:  ')
flag = float(x)

while flag != 0:
    if flag == 1:
        HVL50_thickness, final_brilliance =
```

```
                hvl_thickness_search(0.0, 20, mat_HVL_coeff,
                att4_brilliance, p0_sum, step, 2)
        print('50% attenuation with: ')
        print(HVL50_thickness, 'cm')
        output_file(final_brilliance, energy, 'Att',
                'material.txt', '50%')
        flag = 0

    elif flag == 2:
        HVL75_thickness, final_brilliance =
                hvl_thickness_search(0.0, 20, mat_HVL_coeff,
                att4_brilliance, p0_sum, step, 4)
        print('75% attenuation with: ')
        print(HVL75_thickness, 'cm')
        output_file(final_brilliance, energy, 'Att',
                'material.txt', '75%')
        flag = 0

    elif flag == 3:
        HVL875_thickness, final_brilliance =
                hvl_thickness_search(0.0, 20, mat_HVL_coeff,
                att4_brilliance, p0_sum, step, 8)
        print('87.5% attenuation with: ')
        print(HVL875_thickness, 'cm')
        output_file(final_brilliance, energy, 'Att',
                'material.txt','87.5%')
        flag = 0

    elif flag == 4:
        HVL50_thickness, final_brilliance50 =
                hvl_thickness_search(0.0, 20, mat_HVL_coeff,
                att4_brilliance, p0_sum, step, 2)
        HVL75_thickness, final_brilliance75 =
                hvl_thickness_search(0.0, 20, mat_HVL_coeff,
                att4_brilliance, p0_sum, step, 4)
        HVL875_thickness, final_brilliance875 =
                hvl_thickness_search(0.0, 20, mat_HVL_coeff,
```

```
            att4_brilliance, p0_sum, step, 8)
        print('50% attenuation with: ')
        print(HVL50_thickness, 'cm')
        output_file(final_brilliance50, energy, 'Att',
            'material.txt', '50%')
        print('75% attenuation with: ')
        print(HVL75_thickness, 'cm')
        output_file(final_brilliance75, energy, 'Att',
            'material.txt', '75%')
        print('87.5% attenuation with: ')
        print(HVL875_thickness, 'cm')
        output_file(final_brilliance875, energy, 'Att',
            'material.txt', '87.5%')
        flag = 0

    elif flag == 5:
        thickness_evaluation(mat_HVL_coeff, att4_brilliance,
            p0_sum, step)
        flag = 0

    else:
        print('Wrong insertion, try again.')
        flag = input('Type 1 for HVL calculation,'
            '2 for 75% attenuation, 3 for 87.5% attenuation'
            ', 4 to get them all, 0 to exit:')
```

B | Appendix B

In this section at first the remaining spectra obtained from Python code are presented in Figure B.1. Following the HVL measurement result compared to the calculated value are shown for five remaining spectra in Figures B.2, B.3, B.4, B.5 and B.6 along with the exact HVLs calculated and measured in Tables B.1, B.2, B.3, B.2 and B.5.

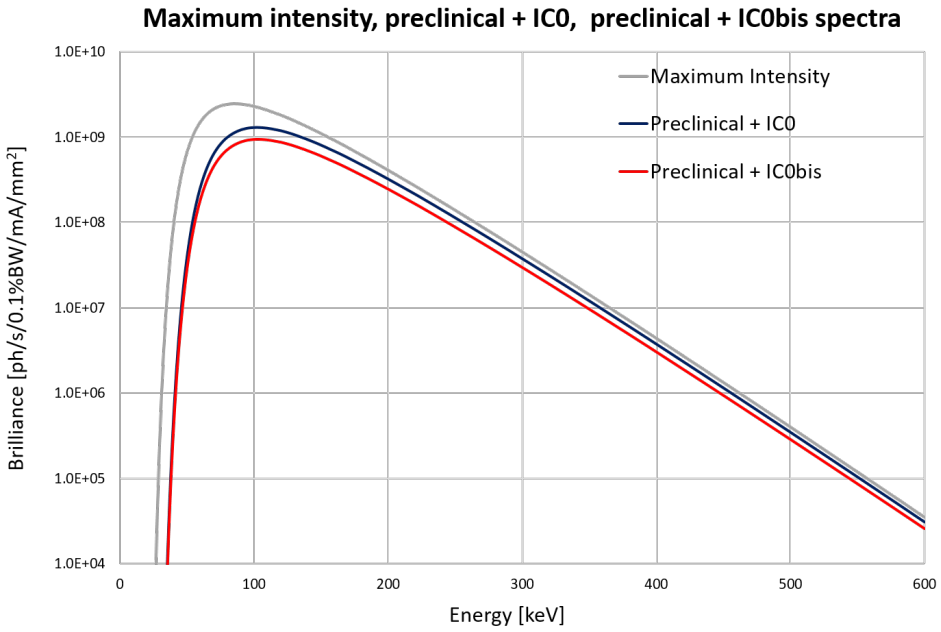

Figure B.1: In grey the maximum intensity spectrum is shown, along with the preclinical spectrum with IC0 in blue and the preclinical spectrum with IC0bis in red.

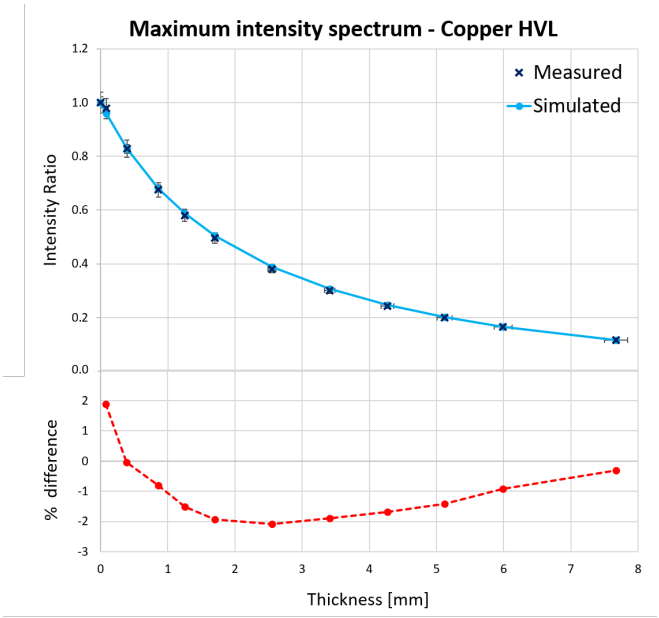

(a)

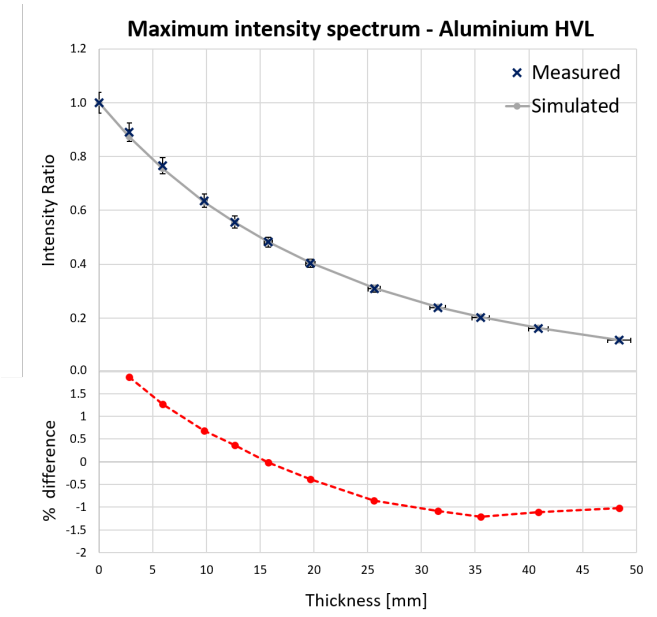

(b)

Figure B.2: (a). Plot of measured data(blue) against the simulated data(light blue) for HVL, using extra Cu sheets, maximum intensity spectrum. (b). Plot of measured data(blue) against the simulated data(grey) for HVL, using extra Al sheets, maximum intensity spectrum.

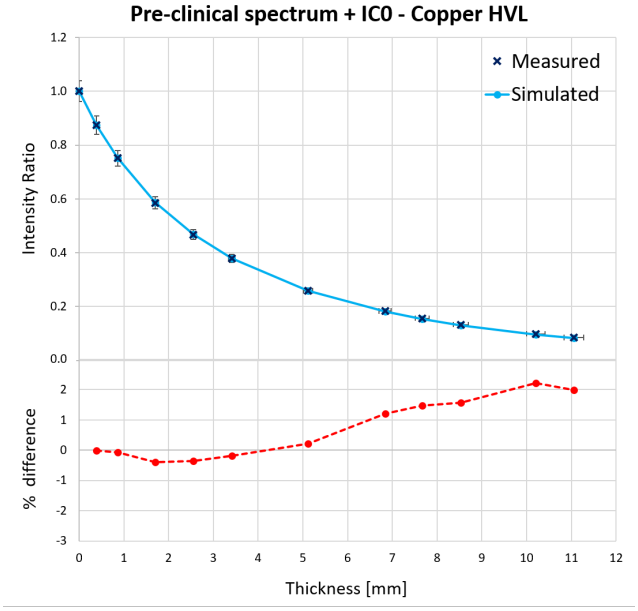

(a)

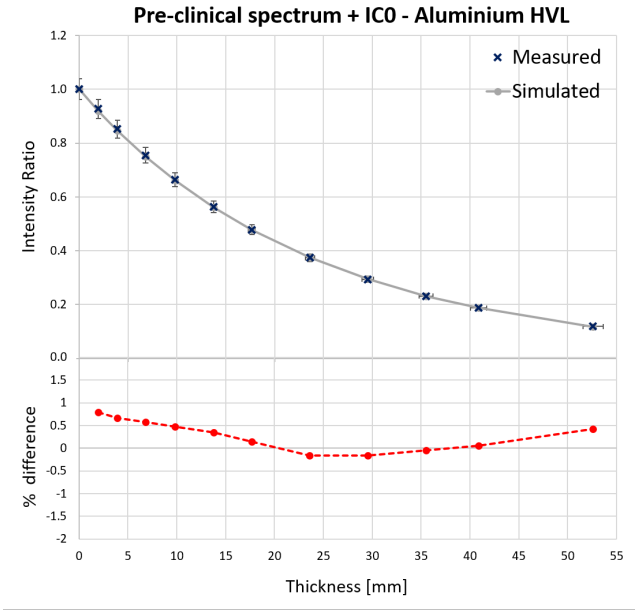

(b)

Figure B.3: (a). Plot of measured data(blue) against the simulated data(light blue) for HVL, using extra Cu sheets, preclinical spectrum plus IC0. (b). Plot of measured data(blue) against the simulated data(grey) for HVL, using extra Al sheets, preclinical spectrum plus IC0.

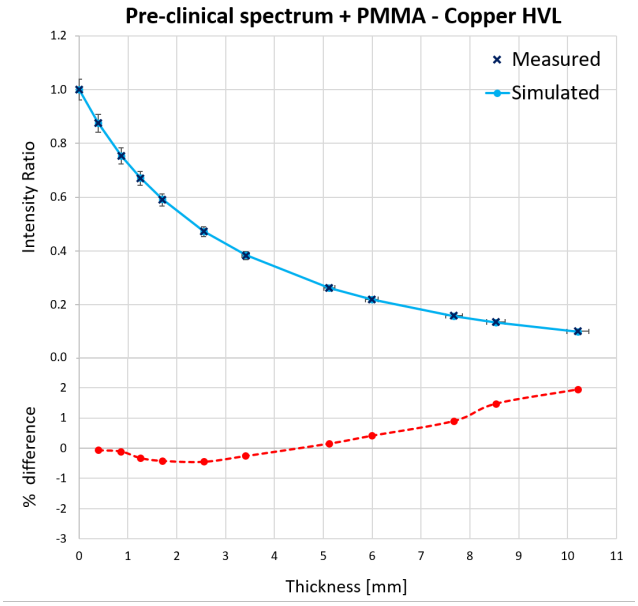

(a)

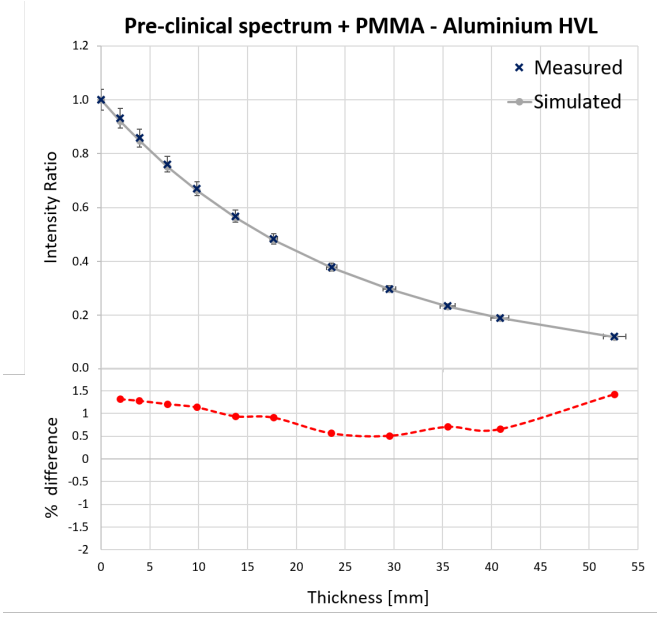

(b)

Figure B.4: (a). Plot of measured data(blue) against the simulated data(light blue) for HVL, using extra Cu sheets, preclinical spectrum plus PMMA. (b). Plot of measured data(blue) against the simulated data(grey) for HVL, using extra Al sheets, preclinical spectrum plus PMMA.

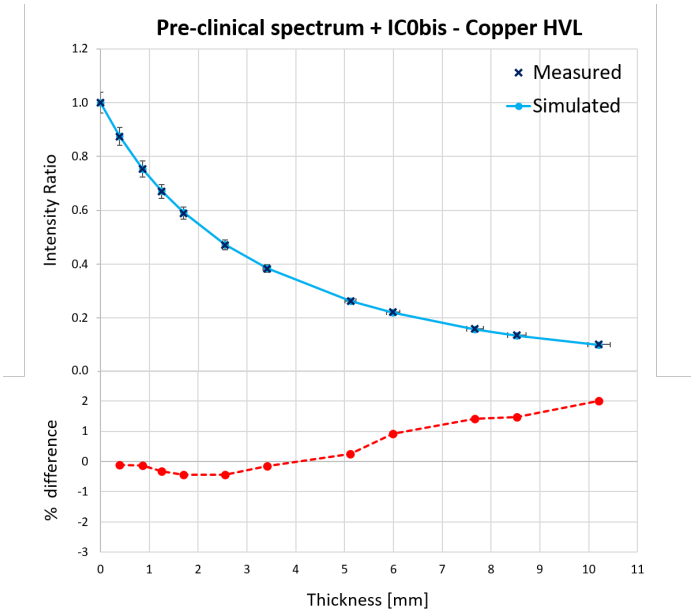

(a)

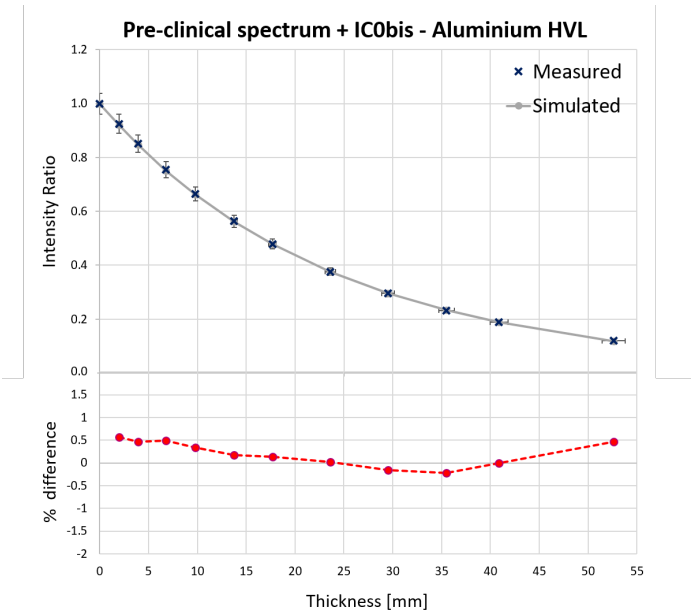

(b)

Figure B.5: (a). Plot of measured data(blue) against the simulated data(light blue) for HVL, using extra Cu sheets, preclinical spectrum plus IC0bis. (b). Plot of measured data(blue) against the simulated data(grey) for HVL, using extra Al sheets, preclinical spectrum plus IC0bis.

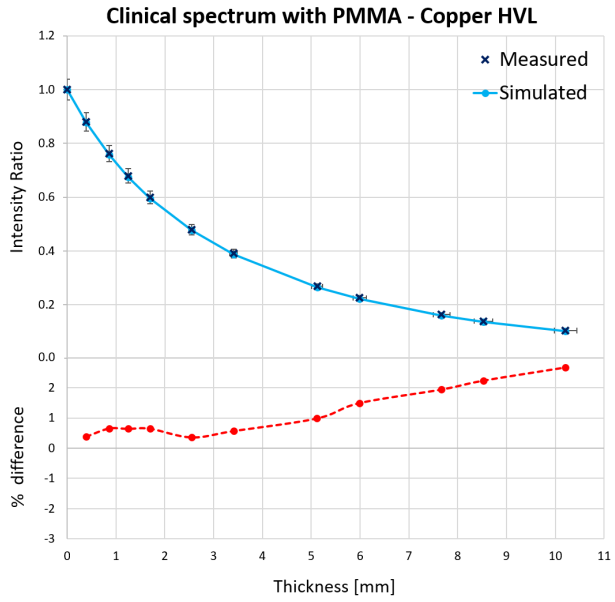

(a)

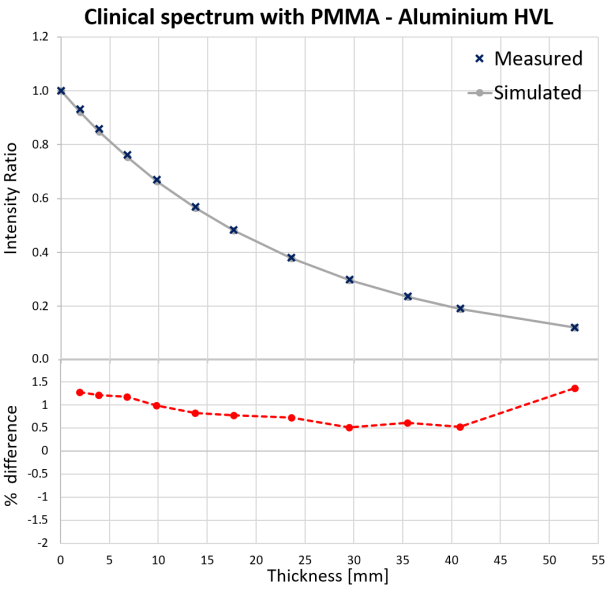

(b)

Figure B.6: (a). Plot of measured data(blue) against the simulated data(light blue) for HVL, using extra Cu sheets, clinical spectrum with PMMA. (b). Plot of measured data(blue) against the simulated data(grey) for HVL, using extra Al sheets, clinical spectrum with PMMA.

Maximum Intensity	Experimental Cu [mm]	Theoretical [mm]	% diff
HVL1	1.69 ± 0.10	1.73 ± 0.03	-2.25
HVL2	4.13 ± 0.25	4.21 ± 0.08	-1.86
HVL3	7.32 ± 0.45	7.33 ± 0.15	-0.10

(a)

Maximum Intensity	Experimental Al [mm]	Theoretical [mm]	% diff
HVL1	14.94 ± 0.92	14.93 ± 0.30	0.01
HVL2	30.55 ± 1.88	30.70 ± 0.61	-0.50
HVL3	46.81 ± 2.88	47.15 ± 0.94	-0.72

(b)

Table B.1: (a). Experimental measured HVLs of Cu compared to theoretical predictions for maximum intensity spectrum. (b). Experimental measured HVLs of Au compared to theoretical predictions for maximum intensity spectrum.

Maximum Intensity	Experimental Cu [mm]	Theoretical [mm]	% diff
HVL1	2.23 ± 0.14	2.30 ± 0.05	1.02
HVL2	5.27 ± 0.32	5.27 ± 0.11	0.05
HVL3	8.85 ± 0.55	8.78 ± 0.18	0.76

(a)

Maximum Intensity	Experimental Al [mm]	Theoretical [mm]	% diff
HVL1	16.57 ± 1.02	16.54 ± 0.33	0.19
HVL2	33.62 ± 2.07	33.58 ± 0.67	0.11
HVL3	51.14 ± 3.15	51.09 ± 1.02	0.09

(b)

Table B.2: (a). Experimental measured HVLs of Cu compared to theoretical predictions for preclinical spectrum plus IC0. (b). Experimental measured HVLs of Au compared to theoretical predictions for preclinical spectrum plus IC0.

Maximum Intensity	Experimental Cu [mm]	Theoretical [mm]	% diff
HVL1	2.34 ± 0.14	2.34 ± 0.05	0.01
HVL2	5.34 ± 0.33	5.35 ± 0.11	-0.24
HVL3	8.99 ± 0.55	8.91 ± 0.18	0.91

(a)

Maximum Intensity	Experimental Al [mm]	Theoretical [mm]	% diff
HVL1	16.81 ± 1.04	16.62 ± 0.33	1.16
HVL2	34.01 ± 2.09	33.75 ± 0.67	0.76
HVL3	51.59 ± 3.18	51.35 ± 1.03	0.46

(b)

Table B.3: (a). Experimental measured HVLs of Cu compared to theoretical predictions for preclinical spectrum plus PMMA. (b). Experimental measured HVLs of Au compared to theoretical predictions for preclinical spectrum plus PMMA.

Maximum Intensity	Experimental Cu [mm]	Theoretical [mm]	% diff
HVL1	2.34 ± 0.14	2.33 ± 0.05	0.62
HVL2	5.34 ± 0.33	5.35 ± 0.11	-0.13
HVL3	9.00 ± 0.55	8.91 ± 0.18	0.97

(a)

Maximum Intensity	Experimental Al [mm]	Theoretical [mm]	% diff
HVL1	16.64 ± 0.92	16.61 ± 0.33	0.16
HVL2	33.77 ± 1.88	33.75 ± 0.67	0.05
HVL3	51.39 ± 2.88	51.34 ± 1.03	0.10

(b)

Table B.4: (a). Experimental measured HVLs of Cu compared to theoretical predictions for preclinical spectrum plus IC0bis. (b). Experimental measured HVLs of Au compared to theoretical predictions for preclinical spectrum plus IC0bis.

Maximum Intensity	Experimental Cu [mm]	Theoretical [mm]	% diff
HVL1	2.40 ± 0.15	2.36 ± 0.05	1.90
HVL2	5.45 ± 0.34	5.40 ± 0.11	0.86
HVL3	9.12 ± 0.56	8.99 ± 0.18	1.49

(a)

Maximum Intensity	Experimental Al [mm]	Theoretical [mm]	% diff
HVL1	16.87 ± 1.04	16.68 ± 0.33	1.13
HVL2	34.12 ± 2.10	33.88 ± 0.68	0.71
HVL3	51.76 ± 3.19	51.53 ± 1.03	0.44

(b)

Table B.5: (a). Experimental measured HVLs of Cu compared to theoretical predictions for clinical spectrum with PMMA. (b). Experimental measured HVLs of Au compared to theoretical predictions for clinical spectrum with PMMA.

List of Figures

List of Tables

List of Symbols

Acronym	Complete Name
RT	Radiation Therapy
MRT	Microbeam Radiation Therapy
TCP	Probability of Tumor Control
NTCP	Probability of Complications on Normal Tissue
PVDR	Peak to Valley Dose Ratio
BM	Bending Magnet
ID	Insertion Device
SR	Synchrotron Radiation
OH1	First Optical Hutch
EH1	First Experimental Hutch
HVL	Half Value Layer
IR	Intensity Ratio
IC	Ionization Chamber
MC	Monte Carlo
RCF	Radiochromic Films
TPS	Treatment Planning System

Acknowledgements

I would like to express my gratitude to my supervisor Dr. Paolo Pellicioli for his endless help and support during the project and the beamtimes, for sharing with me his knowledge and passion about the research and for always making me feel appreciated for my work.
I would like to thank all the team at the ID17 beamline for making me feel warmly welcomed since the first day. In particular thanks to Dr. Michael Krisch for his support during my project, to Dr. Liam Day for helping me with the Monte Carlo simulations and to Dr. Luca Fardin.
My gratitude goes also to Dr. Juan Reyes Herrera for his help on the OASYS software.
I would like to thank as well the Politecnico di Milano and the ESRF for giving me such an amazing opportunity, in particular Prof. Marco Moretti for its availability and support during the development of the project.
My deepest gratitude goes to my family, my mom, my dad and my brother for always encouraging me during these university years.
I want to express my gratitude to all the friends that I met at university. I feel the luckiest person in the world to have encountered such extraordinary people. In particular thanks to Riccardo, Lucia, Paolo, Giorgio, Chiara and Francesca for every moments shared together, for always encouraging me to do my best and for always being there.
A special thanks goes to Stefano for being there both in good and bad days, for sharing the Erasmus experience and for being the incredible person he is.
A very heartfelt thanks goes to Nicolò for being my biggest support and for always believing in me, even when I doubted myself.
Another special thanks goes to the friends who shared the months in Grenoble with me, Camilla, Federico, Federico and Matteo. Without you nothing would have been the same, thanks for making the experience one of the best of my life.
I cannot forget to thank Anna, the best flatmate I could have ever asked for. Thank you for the daily sharing of joy and sadness, for being an amazing friend and an inspiration everyday.
Last but not least, I would like to thank those friends that have been at my side for years

now, with whom I grew up with, Chiara, Andrea and all the others, thanks for always supporting me all along the way.